Distribution Agreement

In presenting this thesis or dissertation as a partial fulfillment of the requirements for an advanced degree from Emory University, I hereby grant to Emory University and its agents the non-exclusive license to archive, make accessible, and display my thesis or dissertation in whole or in part in all forms of media, now or hereafter known, including display on the world wide web. I understand that I may select some access restrictions as part of the online submission of this thesis or dissertation. I retain all ownership rights to the copyright of the thesis or dissertation. I also retain the right to use in future works (such as articles or books) all or part of this thesis or dissertation.

Signature:

Alina Ionescu Date

Protein and Solvent Dynamical Contributions to Reactions of the 2-Aminopropanol Substrate Radical in Ethanolamine Ammonia-Lyase

By

Alina Ionescu

Doctor of Philosophy

Physics

____

Kurt Warncke, Ph.D.
Advisor

____

Laura Finzi, Ph.D.
Committee Member

____

David Lynn, Ph.D.
Committee Member

____

Connie Roth, Ph.D.
Committee Member

____

Daniel Weissman, Ph.D.
Committee Member

Accepted:

____

Lisa A. Tedesco, Ph.D.
Dean of the James T. Laney School of Graduate Studies

____

Date

Protein and Solvent Dynamical Contributions to Reactions of the 2-Aminopropanol Substrate Radical in Ethanolamine Ammonia-Lyase

By

Alina Ionescu
M.S., University of Bucharest, 2012
B.S., University of Bucharest, 2010

Advisor: Kurt Warncke, Ph.D.

An abstract of
A dissertation submitted to the Faculty of the
James T. Laney School of Graduate Studies of Emory University
in partial fulfillment of the requirements for the degree of
Doctor of Philosophy
in Physics
2020

Abstract

Protein and Solvent Dynamical Contributions to Reactions of the 2-Aminopropanol Substrate Radical in Ethanolamine Ammonia-Lyase

By Alina Ionescu

The B_{12}-dependent ethanolamine ammonia lyase (EAL) is the signature enzyme of the ethanolamine utilization (Eut) pathway in pathogenic strains of *Salmonella* and *Escherichia coli* associated with microbiome disease conditions in the human gut. The enzyme catalyzes the deamination of ethanolamine or the unnatural substrate, 2-aminopropanol, for production of nutrients for the bacterial cell. Under pathogenic conditions the enzyme is thought to function in the sub-cellular organelle Eut bacterial microcompartment together with the other enzymes of the Eut pathway. EAL isolated from *S. typhimurium* has been studied by electron paramagnetic resonance (EPR) spectroscopy to gain insights into the fundamental aspects of its molecular mechanism and modulation by the surrounding environment. The EPR spin probe, TEMPOL, identifies concentric phases around EAL: a protein associated domain (PAD, hydration layer) and an aqueous 2-aminopropanol mesodomain. The PAD undergoes the established disorder-to-order transition (ODT) with decreasing *T* over 230-235 K, and this transition can be tuned (*T* decreased) by adding (2.0% v/v) dimethylsulfoxide (DMSO) to 210-215 K. The *T*-dependence of the EPR amplitudes of EAL-bound paramagnets [cob(II)alamin and substrate radical] show a kink at the *T* values that correlates to the *T* of the TEMPOL-detected ODT. The kink is proposed to originate from a change in sample dielectric properties at the ODT. The kinetics of the cryotrapped cob(II)alamin-2-aminopropanol substrate radical pair decay upon temperature (*T*) -step initiation in the range of 210 – 240 K is measured by time-resolved, full-spectrum EPR and show parallel native and non-native (destructive) radical rearrangement pathways. The steric effect of the 2-methyl group on the substrate contributes to an increase in the barrier for the protein configurational interconversion between substrate radical states, $\mathbf{S_1^\bullet}$ and $\mathbf{S_2^\bullet}$, that adds to the native protein configurational barrier. Simulation of the interconversion and reaction microscopic rate constants reveals that the barrier to protein configurational interconversion is raised at the *T* corresponding to the ODT. The results reveal the solvent and protein dynamical coupling that drives the critical protein configurational transition that bridges radical pair capture and rearrangement enabling phases of enzyme catalysis in EAL.

Protein and Solvent Dynamical Contributions to Reactions of the 2-Aminopropanol Substrate Radical in Ethanolamine Ammonia-Lyase

By

Alina Ionescu
M.S., University of Bucharest, 2012
B.S., University of Bucharest, 2010

Advisor: Kurt Warncke, Ph.D.

A dissertation submitted to the Faculty of the
James T. Laney School of Graduate Studies of Emory University
in partial fulfillment of the requirements for the degree of Doctor of Philosophy
in Physics
2020

Acknowledgements

I am thankful to my advisor, Dr. Kurt Warncke, for the guidance and support that he provided during my time at Emory. I am grateful to the members of my committee, Dr. Laura Finzi, Dr. David Lynn, Dr. Connie Roth and Dr. Daniel Weissman for their time and guidance throughout my dissertation research. I also owe thanks to other Warncke lab members: Dr. Umar Twahir for his time and mentoring during my first year at Emory, and to Dr. Meghan Kohne, Dr. Nforneh Benjamen and Wei Li for their valuable inputs during group meetings. I am also thankful to Dr. Raghunath Gokul for his thoughtful inputs on the molecular biology aspect of my project.

I want to thank all of the friends that my move to the US brought into my life for the time spent together. Warm thanks to Jaya, Bhavya, Miling, Ashwin, Sushmita, and the Bhakti yoga community at Georgia Tech for their remarkable friendship. I find myself lucky to have met you and be part of your lives.

I am also deeply grateful to the unconditional love and support of my parents and brother who have been there for me in my hardest times and had never stopped believing in me. I am also grateful to my boyfriend who, from the moment we met, never stopped encouraging and motivating me to reach the end of this journey. Regardless of our paths, I will always be appreciative of his contribution to my professional and personal growth. Thank you!

Table of Contents

Chapter I: Studies of EAL and Eut proteins by using EPR spectroscopy

1.1. Introduction 2

1.1.1. The coenzyme B_{12}: AdoCbl 5

1.1.2. Ethanolamine Ammonia Lyase: an AdoCbl-Dependent Enzyme 7

1.1.2.1. Structure 7

1.1.2.2. Metabolic Pathway 8

1.1.2.3. Minimal Mechanism for EAL Catalytic Cycle and the Active Site 10

1.1.2.4. Catalysis and Dynamics 12

1.1.3. Bacterial Microcompartments 14

1.1.3.1. The BMC structural protein EutS 16

1.1.3.2. The BMC structural protein EutL 17

1.2. Experimental techniques 18

1.2.1. Continuous Wave EPR spectroscopy 18

1.2.1.1. Paramagnetic molecules: TEMPOL and 4-Maleimido-TEMPO 21

1.2.1.2. Paramagnetic species in EAL, EPR spectroscopy 24

1.2.1.3. Spin-Lattice Relaxation 27

1.2.2. Site Directed Spin Labeling 27

1.3. Outline 29

Chapter II: Solvent dynamics around EAL in 10 mM 2-aminopropanol with 0 % and 2 % DMSO

2.1. Introduction 31

2.2. Materials and Methods 33

2.2.1. Protein and EPR sample preparation ... 33

2.2.2. Continuous Wave EPR spectroscopy ... 34

2.2.3. EPR Simulations ... 35

2.3. Results ... 36

2.3.1. TEMPOL EPR line shape. Temperature dependence in frozen aqueous solution with EAL and 2-aminopropanol in the presence of 0 % v/v DMSO ... 36

2.3.2. TEMPOL EPR line shape. Temperature dependence in frozen aqueous solution with EAL and 2-aminopropanol in the presence of 2 % v/v DMSO ... 36

2.3.3. TEMPOL rotational correlation times and normalized weights. Temperature dependence in frozen aqueous solution with EAL and 2-aminopropanol in the presence of 0 % v/v DMSO ... 39

2.3.4. TEMPOL rotational correlation times and normalized weights. Temperature dependence in frozen aqueous solution with EAL and 2-aminopropanol in the presence of 2 % v/v DMSO ... 41

2.4. Discussion ... 43

2.4.1. 10 mM 2-aminopropanol is creates a mesodomain around EAL at cryogenic temperatures ... 43

2.4.2. Addition of 2 % v/v DMSO to the 10 mM 2-aminopropanol increases the mesodomain volume ... 44

2.4.3. Estimations for the relative dimensions of the mesodomain ... 48

2.5. Conclusions ... 49

Chapter III: Mechanism of 2-aminopropanol substrate radical rearrangement catalysis in B_{12}-dependent EAL

3.1. Introduction ... **51**

3.2. Materials and Methods ... **53**

3.2.1. Protein and EPR sample preparation ... 53

3.2.2. Continuous Wave-EPR spectroscopy ... 54

3.2.3. Time-resolved full-spectrum EPR spectroscopy of substrate radical decay at cryogenic temperatures ... 55

3.2.4. Steady-State Kinetic Measurements ... 57

3.2.5. Transient kinetics analysis ... 58

3.2.6. Temperature dependence of observed rate constants ... 58

3.2.7. Numerical simulations and fitting of the minimum kinetic model ... 59

3.3. Results ... **60**

3.3.1. Time-resolved, full-spectrum EPR of the cryotrapped 2-aminopropanol substrate radical intermediate in EAL ... 60

3.3.2. EPR spectra of the deconvoluted Cbl(II)-radical pair species ... 63

3.3.3. Quantification of the radical species contribution to the EPR spectra. Proportions of the diamagnetic product states ... 64

3.3.4. Time-dependence of the Cbl(II)-substrate radical pair decay component ... 66

3.3.4.1. Cryotrapped 2-aminopropanol substrate radical intermediate in EAL with 0 % v/v DMSO solution, measured over 210-240 K ... 66

3.3.4.2. Cryotrapped 2-aminopropanol substrate radical intermediate in EAL with 2 and 4 % v/v DMSO solution, measured at 230 K and 240 K ... 68

3.3.5. Time-dependence of the growth of the uncoupled Cbl(II) 70

3.3.5.1. EPR measurements for EAL and 2-aminopropanol in 0 % v/v DMSO solution at *T* in the range 210-240 K 70

3.3.5.2. EPR measurements for EAL and 2-aminopropanol in 2 and 4 % v/v DMSO solution at T of 230 K and 240 K 72

3.3.6. Steady-state kinetic measurement 74

3.4. Discussion 78

3.4.1. Kinetic Model. Microscopic rate constants for protein configurational change and rearrangement reaction steps 78

3.4.2. Arrhenius behavior of the observed rate constants 81

3.4.3. Contributions of the protein-solvent dynamical coupling to protein configurational change and rearrangement reaction steps 85

3.5. Conclusions 88

Chapter IV: Temperature-Dependence of the EPR Amplitude of Uncoupled Cbl(II) and Substrate Radical in EAL Provides a Direct Probe of Solvent Dynamics

4.1. Introduction 91

4.2. Materials and methods 92

4.2.1. Sample preparation 92

4.2.2. Continuous wave-EPR Spectroscopy 93

4.2.3. Progressive power saturation analysis 94

4.3. Results and Discussion 95

4.3.1. Paramagnetic species in EAL after reaction with 2-aminopropanol 95

    4.3.2. Cbl(II)-substrate radical pair EPR line shape. Temperature dependence in frozen aqueous solution after EAL reaction with 2-aminopropanol in the presence of DMSO: 0, 2 and 4 % v/v 98
    4.3.3. Temperature dependence of the EPR amplitudes of residual and terminal species in EAL after reaction with 2-aminopropanol 99
    4.3.4. Progressive Power Saturation 102
4.4. Conclusions 104

Chapter V: Preliminary Studies Towards Structural Investigation in Bacterial Microcompartment Proteins EutL and EutS by Electron Paramagnetic Resonance Spectroscopy

5.1. Introduction 108
5.2. Materials and methods 111
    5.2.1. Protein cloning and expression 111
    5.2.2. Site directed mutagenesis 112
    5.2.3. Protein purification 113
    5.2.4. Fast protein liquid chromatography (FPLC) 114
    5.2.5. SDS and native PAGE 114
    5.2.6. SDSL 115
    5.2.7. CW-EPR spectroscopy 117
    5.2.8. CW-EPR simulations 118
5.3. Results and Discussion 118
    5.3.1. Structure and sequence analysis to identify SDSL sites 118
    5.3.2. Purified Protein oligomers 124

  5.3.3. Predicted nitroxide rotamers at Cys residues in EutL and EutS 126

  5.3.4. SDSL CW-EPR of EutS.. 130

  5.3.5. SDSL CW-EPR of EutL A73C C201S 133

5.4. Summary.. 135

Chapter VI: Final conclusions

6.1. Summary.. 138

6.2. Solvent-protein-reaction coupling in EAL... 139

BIBLIOGRAPHY 142

Appendix.. 150

List of Tables and Figures

Chapter I

Figures

Figure 1.1. The *eut* operon from *S.enterica* with the color code describing each gene function. 4

Figure 1.2. Structure of adenosylcobalamin cofactor.[44] 6

Figure 1.3. PyMOL cartoon for EAL from *E. coli* represented from the determined X-ray crystal structure (PDB: 5YSR)........ 8

Figure 1.4. The ethanolamine degradation pathway........ 9

Figure 1.5. Minimal mechanism for EAL catalytic cycle........ 11

Figure 1.6. Solvent environment around EAL......... 13

Figure 1.7. Structure of EutS BMC from *E. coli* determined by X-ray crystallography.. 16

Figure 1.8. Structure of EutL BMC from *E. coli* determined by X-ray crystallography.. 17

Figure 1.9. The energy diagram for an unpaired electron with *S=1/2* and the EPR signal recorded as the first derivative of the absorption......... 19

Figure 1.10. A. Energy level diagram for the resonance lines in a nitroxide spin label that arise from the interaction of an unpaired electron with the local nitrogen atom........ 23

Figure 1.11. Effect on EPR spectra from the motions of the spin systems........ 24

Figure 1.12. EPR spectrum of cobalamin and cryoptrapped Cbl(II)-2-aminopropanol substrate radical pair. 26

Chapter II

Tables

Table 2.1. Arrhenius parameters obtained from the *T*-dependence of the rotational correlation times for TEMPOL tumbling motion in EAL and 10 mM 2-aminopropanol system with or without DMSO 46

Figures

Figure 2.1. Temperature dependence of the TEMPOL EPR spectrum for the frozen EAL solution in the presence of 10 mM 2-aminopropanol 38

Figure 2.2. Temperature dependence of the rotational correlation time (A) and normalized mobility component weights (B) of TEMPOL in the presence of EAL and 10 mM 2-aminopropanol with 0 % v/v DMSO added... 40

Figure 2.3. Temperature dependence of the rotational correlation time (A) and normalized mobility component weights (B) of TEMPOL in the presence of EAL and 10 mM 2-aminopropanol with 2 % v/v DMSO added... 42

Figure 2.4. Arrhenius plot for rotational correlation times that characterize the TEMPOL in solution of EAL, 10 mM 2-aminopropanol and the different DMSO %................................. 47

Chapter III

Tables

Table 3.1. First-order rate constants and normalized amplitude parameters for the biexponential fitting to the decay kinetics of the Cbl(II)-substrate radical pair at indicated temperatures and added % v/v DMSO.. 70

Table 3.2. First-order rate constants and normalized amplitude parameters for the mono- and bi-exponential fitting to the growth curves of the uncoupled Cbl(II) at indicated temperatures and added % v/v DMSO. 74

Figures

Figure 3.1. EPR spectrum of the cryoptrapped Cbl(II)-2-aminopropanol substrate radical pair in EAL. 61

Figure 3.2. Time-resolved, full-spectrum EPR of the cryotrapped 2-aminopropanol substrate radical intermediate in EAL resolved by X-band EPR at 230 K. 62

Figure 3.3. Time-dependence EPR signal of the uncoupled Cbl(II) radical species 63

Figure 3.4. The absorption spectra of the EPR signal of the Cbl(II)-substrate radical pair measured at 230 K 65

Figure 3.5. The time-dependence of the EPR amplitude of the substrate radical component at the measured temperatures 67

Figure 3.6. The time-dependence of the EPR amplitude of the 2-aminopropanol substrate radical component in the presence of 2 % v/v DMSO (A&B) and 4 % v/v DMSO (C&D) 69

Figure 3.7. The time-dependence of the EPR amplitude of the uncoupled Cbl(II)- radical state component 71

Figure 3.8. Time-dependence of the EPR amplitude of the uncoupled Cbl(II) 73

Figure 3.9. Time-dependence of the Cbl(II)- 2-aminopropanol substrate radical pair state in EAL. 76

Figure 3.10. The time-dependence of the EPR amplitude of **S$^\bullet$** (red), **X$^\bullet$** (blue) and **PH** (black) from the EPR signal measured at 288 K. 77

Figure 3.11. Microscopic kinetic models tested for the mechanism of the Cbl(II)-2-aminopropanol substrate radical pair decay in EAL. 79

Figure 3.12. Time-dependence of the deconvoluted Cbl(II)-2-aminopropanol substrate radical pair decay components in EAL and % DMSO at the corresponding measured *T* values overlaid with simulated components of the kinetic model 80

Figure 3.13. Arrhenius plot of the mean first order rate constants from the mono/biexponential fittings 82

Figure 3.14. Kinetic scheme. The kinetic model for the decay of the 2-ampropanol substrate radical in EAL at 210 K and over the *T* range of 220-240 K.. 84

Figure 3.15. Arrhenius plot of the mean first order rate constants from the mono/biexponential fittings 85

Figure 3.16. Arrhenius plots for the microscopic rate constants determined from the proposed kinetic model for Cbl(II)-substrate radical decay in EAL.. 87

Chapter IV

Tables

Table 4.1. Parameters of the linear fits to the *T*-dependence amplitudes of the uncoupled Cbl(II) and substrate radical features at different % v/v DMSO 100

Table 4.2. Progressive power saturation parameter, $P_{1/2}$, determined at 200 K and 235 K for uncoupled Cbl(II) and substrate radical, $\mathbf{S}^{\bullet}$, in EAL and different % DMSO....................... 103

Figures

Figure 4.1. Representative EPR spectrum of the cryotrapped Cbl(II)-2-aminopropanol substrate radical pair and uncoupled species in EAL. 97

Figure 4.2. Temperature dependence of the Cbl(II)-substrate radical and uncoupled Cbl(II) + radical species spectra for the decayed cryotrapped Cbl(II)-2-aminopropanol substrate radical pair in EAL solution in the presence of different added % v/v DMSO 99

Figure 4.3. *T*-dependence of the amplitude of the uncoupled Cbl(II) (A) and substrate radical (B) features at constant microwave power and at different % v/v DMSO 101

Figure 4.4. Progressive power saturation for the decayed EAL-bound paramagnets [substrate radical (A) and uncoupled Cbl(II) (B)] in reaction solution with different % v/v DMSO 104

Chapter V

Tables

Table 5.1. Solvent accessible surface area of residues that reposition, revealing movement upon conformational change between open and closed states of EutL. 123

Table 5.2. Distance calculations in PyMOL between modelled MTSL nitroxide labels attached to the protein at indicated sites. 129

Figures

Figure 5.1. Sequence alignment of amino acids for EutS and EutL proteins from *E. coli* and *S. typhimurium*. 119

Figure 5.2. EutL monomers in closed (green) and open (light pink) conformations overlapped 122

Figure 5.3. Overlap of the closed (green) and open (light pink) conformations of EutL that shows the rearrangement in the loop of domain 1. 124

Figure 5.4. SDS PAGE and gel filtration on Superdex 200 of purified proteins............ 125

Figure 5.5. PyMOL cartoon representation for the shell proteins EutS and EutL with the most probable MTSL rotamers. 129

Figure 5.6. Simulated EPR signal using easyspin for the dipole-dipole interaction between the nitroxide labels predicted at the Cys106 position 131

Figure 5.7. 4MT EPR spectrum for EutS protein at room *T*.. 133

Figure 5.8. 4MT EPR spectrum for EutL A73C C201 labeled protein. 135

Chapter I

Studies of EAL and Eut proteins by using EPR spectroscopy

1.1. Introduction

Gastrointestinal (GI) and urinary tract infections that promote disease conditions have been a major cause of the successful proliferation of pathogens in challenging environments.[1, 2] The most prevalent pathogen is the prokaryotic class bacteria which possess a remarkable adaptability to various environments making them the most common single-celled organisms.[3] Bacteria serve as critical biochemical factories in earth's ecology, converting complex chemicals into simple molecules (carbohydrate digestion) or producing vitamins in diverse host systems like humans, plants and animals.[4] In human and animal hosts, bacteria colonize the intestines in high number (between 500-1000 species; make up ~10^{14} cells)[5, 6], where they facilitate proper digestion and regulate immune homeostasis.[7] However, when the peaceful collaboration between the intestinal microbiota and the intestinal cells is disturbed, the health of the host is affected. This disturbance happens when certain bacteria develop an advantage and overgrow to an extent that the immune system cells or antibiotics are unable to restore the equilibrium in the intestinal microbiota. The fitness of some bacteria to overgrow and promote infection has been associated with utilization of ethanolamine (EA) as nutrient.[8] The source of the metabolic compound EA is the lipid phosphatidylethanolamine (PE) which comprises 25 - 45 % of all phospholipids within the membrane wall of all eukaryotic and prokaryotic cells.[8-10] In mammalian and human cell membrane PE is the second most abundant lipid with the highest percentage in mitochondria lipid bilayer (70 %) and is operative in membrane structure, lipoprotein secretion, blood clotting, cytokinesis, cell signaling and membrane fusion and fission. [11, 12] In the GI tract the frequent and fast turnover of the intestinal epithelia, the high population of bacteria and the food diet provide a rich source of PE which is converted into EA and glycerol by phosphodiesterase.[3, 9, 13]

Many bacteria that reside or inhabit the gut have the ability to use EA as a sole nutrient source and they include species of *Escherichia coli*, *Salmonella enterica*, *Listeria monocytogenes*, *Clostridium perfringens* and *Enterococcus faecalis*.[14-19] Strains of these pathogens like the enterohemorrhagic and enteropathogenic *E. coli*, *S. enterica serovar typhimurium* and *Enteritidis*, *L. monocytogenes* CLIP80459 and *C. perfringens* have been associated with food poisoning, diarrhea or hemorrhagic colitis caused by disease conditions like foodborne disease.[18-23] The intestine resident uropathogenic *E. coli* (UPEC) strain have been shown to cause urinary tract infection by migrating from the gut to perineum, urethra and finally the bladder.[2, 24] Recently the cause of inflammatory bowel disease has been identified as *E. coli* infection. [1]

These diseases have been associated with ethanolamine utilization genes encoded in a *eut* operon present in over 100 bacterial genomes.[21, 25] In some cases, however the eut pathway is thought to promote innate immune response in the intestine of the host through the downstream pathway of the product acetate, which binds to G-protein-coupled receptor 43 and triggers the immunoglobulin A production further modulating the immune response and inflammation. [8, 26] This *eut* operon presents different content and organization among the different bacteria. The anaerobic species have a rather long operon compared to the aerobic bacteria whose operon is short, encoding for only a few genes. [19, 27] However, in both cases the *eut* operons encode a common pair of genes, *eutB* and *eutC*, which express the two subunits that form the signature enzyme ethanolamine ammonia lyase (EAL).[15, 28, 29] This enzyme starts the EA catabolism in the presence of its cofactor, adenosylcobalamin (AdoCbl). In addition to the two main genes *eutB* and *eutC*, the longer operons contain accessory genes that encode structural proteins that play a major role in regulation, efficiency and optimization of EA catabolism.[30-32] (Figure 1.1) Five of these proteins self-assemble to form bacterial microcompartments (BMC) [33-37] and they include EutS, EutM, EutN, EutL and EutK. Their role, function and structure are intensely studied and it has been shown that BMCs are highly expressed in strains of *C perfringens*, *S. enterica*, *E. coli* and *Klebsiella* which have a negative impact on human health as they are implicated in disease conditions ranging from food poisoning to colon cancer.[38] Moreover, it has been suggested that the BMC isolates and sequesters the toxic volatile intermediate acetaldehyde from the reaction pathway increasing its local concentration together with other intermediates, thus enhancing the efficiency of the downstream reactions.[30, 32, 39] The expression of these genes is regulated by eutR as well as by AdoCbl in the presence of eutV.[8]

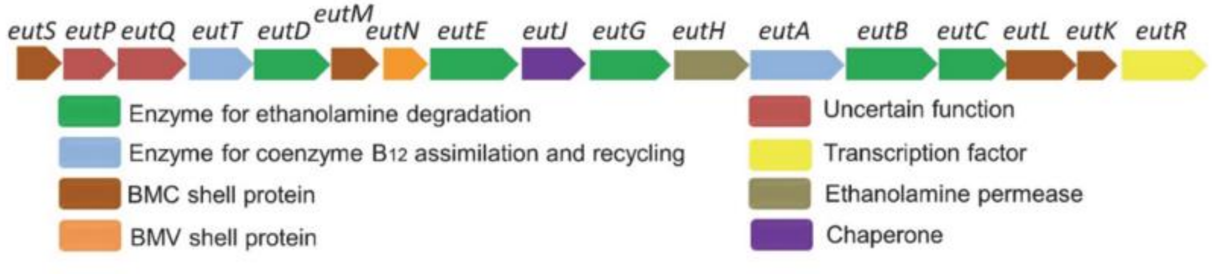

Figure 1.1. The *eut* operon from *S.enterica* with the color code describing each gene function.[37, 40]

For several years there has been a collective effort towards understanding the underlying biological processes that are operative in the ethanolamine utilization pathway. Although the function of many proteins encoded by *eut* genes have been identified, the details of their mechanisms and regulatory pathways are still not fully resolved. Moreover, insights into the molecular basis of the catalytic mechanism of the signature enzyme EAL, will bring advancement not only in enzyme engineering but also towards therapeutic developments in fighting the disease conditions associated with the *eut* pathway. In particular, the EAL catalysis is a special one because of the nature of the reactions enabled by the use of the B_{12}-coenzyme.

1.1.1. The coenzyme B_{12}: AdoCbl

The cofactor AdoCbl initiates the EAL catalytic process of breaking down EA into acetaldehyde and ammonia. AdoCbl is also a cofactor for 11 other enzymes reported so far.[41] It is formed by using the adenosine from adenosine triphosphate (ATP) and the corrinoid cobalamin adenosyltransferase encoded in the *eut* operon by *eutT*. [42] In some bacteria with long operons the cofactor is also involved in *eut* genes regulatory system by negatively influencing the EutX and EutV interaction, thus playing a dual role.[8] In addition to regulatory function, AdoCbl together with EA serve as a transcription coinducer for the *eut* operon.[42, 43]

Also known as the coenzyme B_{12}, AdoCbl represents one of the two biologically active forms of vitamin B_{12}, the other being methylcobalamin (MeCbl).[41, 44] With the most complex structure among biological cofactors, AdoCbl is produced only in prokaryotes but also used by higher eukaryotes. As is shown in Figure 1.2, AdoCbl is formed from cobalamin and 5'-deoxy-adenosine.[44] The cobalamin structure shows the cobalt (Co) ion bound by the four nitrogen atoms of a corrin ring which constitutes a macrocycle, and four propionamide side chains from which one has an attached nucleotide tail that includes a dimethylbenzimidazole (DMB) group. This group coordinates Co at the axial position below the corrin ring through a nitrogen from the imidazole ring of DMB. The axial position above the macrocycle is occupied by a covalent bond with the 5’ carbon on adenosine. This relatively weak covalent bond ($BDE \approx 30$ kcal/mol) is significant in the chemistry of biological processes as the homolysis of the bond gives a Cbl(II) and a highly reactive organic radical 5’-deoxyadenosyl radical (Ado•) which is considered to facilitate difficult and unusual catalytic reactions.

The reactions enabled by the B_{12}-coenzymes yield highly reactive organic radicals that can be exploited by their dependent enzymes to perform catalysis on un-reactive molecules. The capability to cause cobalt-carbon (Co-C) homolysis has been associated with the flexibility induced by the relatively small distortion in the corrin plane of the macrocycle, distortion caused by the electrostatic interactions with the protein or by the displacement of the DMB tail.[41] A better understanding of the generation and control of free radicals by B_{12}-dependent enzymes could advance the field of enzyme engineering towards expanding and improving the catalysis of diverse free radicals.

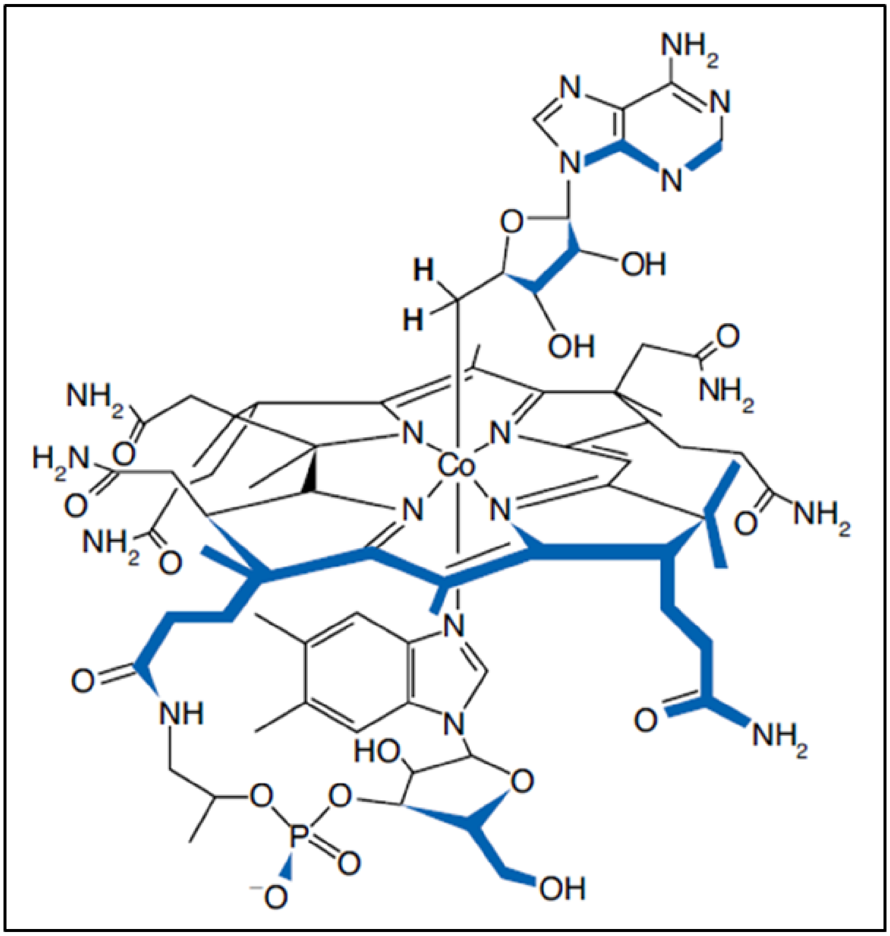

Figure 1.2. Structure of adenosylcobalamin cofactor.[44]

1.1.2. Ethanolamine Ammonia Lyase: an AdoCbl-Dependent Enzyme

Among all pathogenic species, the EA catabolism together with the AdoCbl-dependent EAL enzyme have been identified in strains of *E. coli* and *S. typhimurium* about 50 years ago.[45-47] EAL, like most B_{12}-dependent enzymes, is found only in bacteria, and the X-ray crystal structure of a truncated EAL protein with its coenzyme and substrate is available.[48] Based on the catalytic process, the AdoCbl-dependent EAL belongs to the isomerase family of the B_{12}-dependent enzyme superfamily.[44, 49] Further, based on the nature of the substrate which dictates the type of rearrangement through which the Co-C bond is cleaved, the enzyme is placed in the eliminase subgroup. One of the characteristics of this group is that AdoCbl maintains its Cbl coordination with DMB throughout the catalytic process.[41, 44, 49]

1.1.2.1. Structure

EAL encoded within the *eut* operon by the *eutB* and *eutC* genes is functional only in the presence of its cofactor AdoCbl. The two genes express the two subunits which come together to form a monomer [EutBEutC] that contains an active site. The EAL oligomer is a trimer of dimers presenting a $[[\text{EutBEutC}]_2]_3$ stoichiometry with six active sites. In Figure 1.3 the X-ray crystal structure of the EAL from K12 *E. coli* strain (Protein Data Base (PDB): 5YSR) is depicted together with its cofactor and 2-aminopropanol localized in each of the six pockets.[50] In the active site, it is the larger EutB subunit that contains the binding region for the substrate as well as the binding motif for the coenzyme-B_{12} in the C-terminal region.[51] The globular protein has a molecular mass of approximately 500 kDa with each of the subunits representing 50 kDa and 32 kDa, respectively.

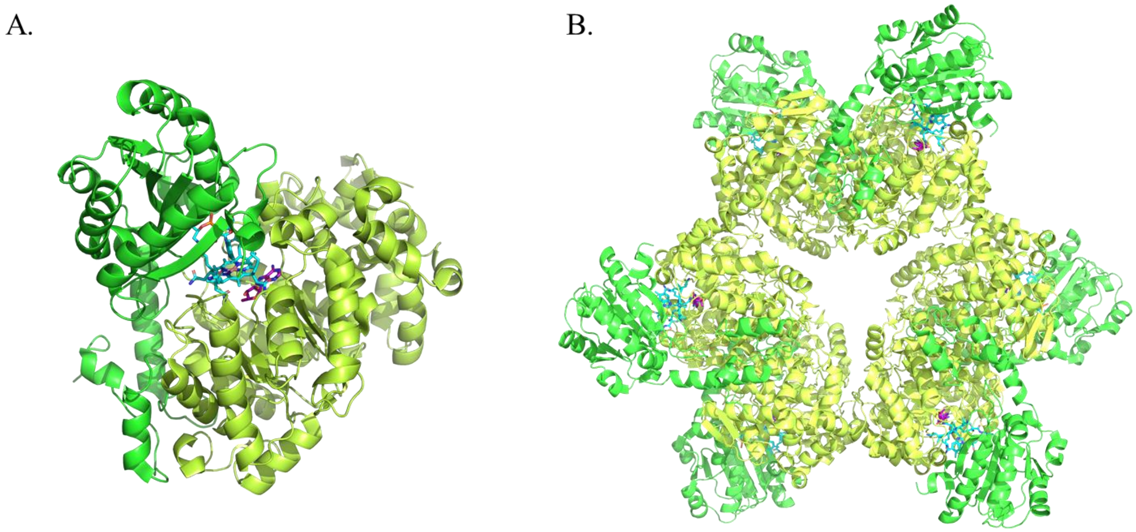

Figure 1.3. PyMOL cartoon for EAL from *E. coli* represented from the determined X-ray crystal structure (PDB: 5YSR). [50] Panel A. shows the EutBEutC monomer; and B. the hexamer (or trimer of dimers: $[(\text{EutB-EutC})_2]_3$). The subunits EutB and EutC are presented in yellow and green. Within the active sites the cofactor, AdoCbl (light blue), and the substrate, 2-amino-1-propanol (purple) are depicted.

1.1.2.2. Metabolic Pathway

In the first step of EA metabolism, after successful transport of the EA through diffusion or transporter proteins across the cytoplasmic membrane of the bacteria, the EAL in the presence of its cofactor, AdoCbl, converts EA into ammonia and acetaldehyde.[52] Further, acetaldehyde is converted by EutE into acetyl-coenzyme A (acetyl-CoA), or in a parallel reaction by EutG into alcohol through a reduction or oxidation of a nicotinamide adenine dinucleotide (NAD). The acetyl-CoA is converted by EutD into acetyl phosphate which is processed further by acetate kinase into acetate with production of ATP. [30] (Figure 1.4) Both ammonia and ethanol are used as nutrients by the cells. [15, 28]

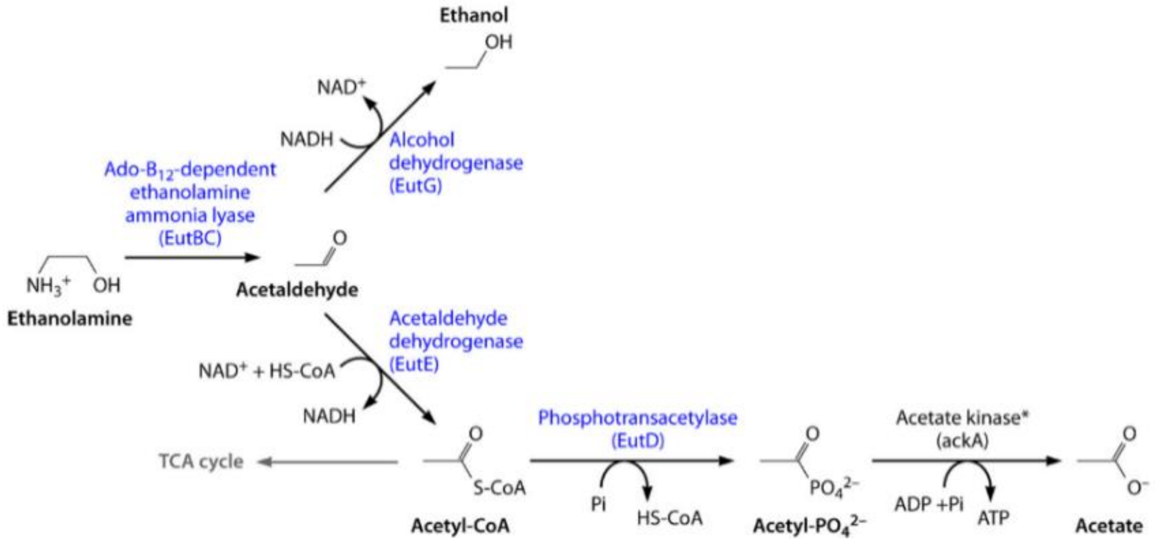

Figure 1.4. The ethanolamine degradation pathway which involves: the vitamin B_{12}-dependent enzyme EAL, the alcohol dehydrogenase, acetaldehyde dehydrogenase and phosphotransacetylase enzymes. The ethanolamine degradation serves as nitrogen and carbon source for bacteria.[37]

In addition to the abundant biological substrate EA, studies have reported that EAL also catalyzes the deamination of the unnatural substrate 2-aminopropanol into propionaldehyde and ammonia.[53] In contrast to EA, 2-aminopropanol has a methyl group substitution at the C2 carbon and presents two enantiomers (R)- and (S)-2-aminopropanol based on the chirality of the amino group. (Figure A.1 in Appendix A) Although EAL binds both enantiomers nonspecifically, the catalytic efficiency of EAL (k_{cat}/K_M) is decreased by 10 and 5-fold when using the (R)- and (S)-2-aminopropanol versus the natural EA, which is suggested to be due to the presence of the methyl group.[54-56] The binding affinity for (R)-2-aminopropanol in the EAL active site is much lower than for (S)-2-aminopropanol which has a K_m lower by an order of magnitude.[55, 57] It was suggested that the enantiomers are binding in the active site differently and are perceived as different substrates. The spatial separation between the Co(II) center and C1 atom on the substrate differs between EA (9.3 Å) and (S)-2-aminopropanol (11 Å) by 2 Å, which is suggested to be due to the steric interactions generated by the extra methyl group on 2-aminopropanol.[58-60] In the present studies (S)-2-aminopropanol is used as substrate for the B_{12}-dependent EAL.

1.1.2.3. Minimal Mechanism for EAL Catalytic Cycle and the Active Site

As mentioned earlier, the weak covalent bond between Cbl and the 5’ carbon on 5'-deoxy-adenosine in AdoCbl plays an important role in EAL catalysis. In Figure 1.5, the minimal mechanism for the EAL catalytic cycle is shown in a 6-step process that depicts the heteroatom elimination.[61] Upon AdoCbl binding in the active site of the EAL the enzyme becomes active and can now bind the substrate (1) which enables the homolysis of the weak covalent Co-C bond in the coenzyme and generation of the radical species Cbl(II) and $Ado^{\bullet}$.[48, 50] The first hydrogen transfer (HT1) in the cycle (2) is done by the highly reactive $Ado^{\bullet}$ who abstracts a H atom from the substrate C1 carbon creating the substrate radical (**S**$^{\bullet}$) and the 5'-deoxy-adenosine.[59] The radical rearrangement step occurs within **S**$^{\bullet}$ with migration of the NH_2 group from C2 to C1 simultaneously with electron spin density transfer on C2 and leading to product radical formation (3).[56, 61] In the second hydrogen transfer step (HT2) a H atom is transferred from 5'-deoxy-adenosine to the product radical to form the product species, aldehyde and ammonia (4). The cycle ends with the regeneration of the AdoCbl through reformation of the Co-C bond (5).

2-Aminopropanol arrangement in the active site allows for the same 6-step reactions to occur in the catalytic cycle. However, suicidal inactivation under this substrate was previously reported and it is suggested to be a consequence of side reactions within the active site.[50, 57] After homolysis, the ribose of the adenosyl radical ($Ado^{\bullet}$) forms H-bonding with the enzyme at Serα247 and Cbl(II) at the oxygen atom of R28 and undergoes displacement of 5-7 Å to mediate the HT1.[50, 59, 60] Moreover, the interactions within the active site during the catalysis reaction are conducted through H bonds and Van der Waals contacts between six key residues of the EutB subunit which not only represent binding sites for substrates and intermediates but also assist homolysis and stabilize the transition state.[56, 59, 62-64]

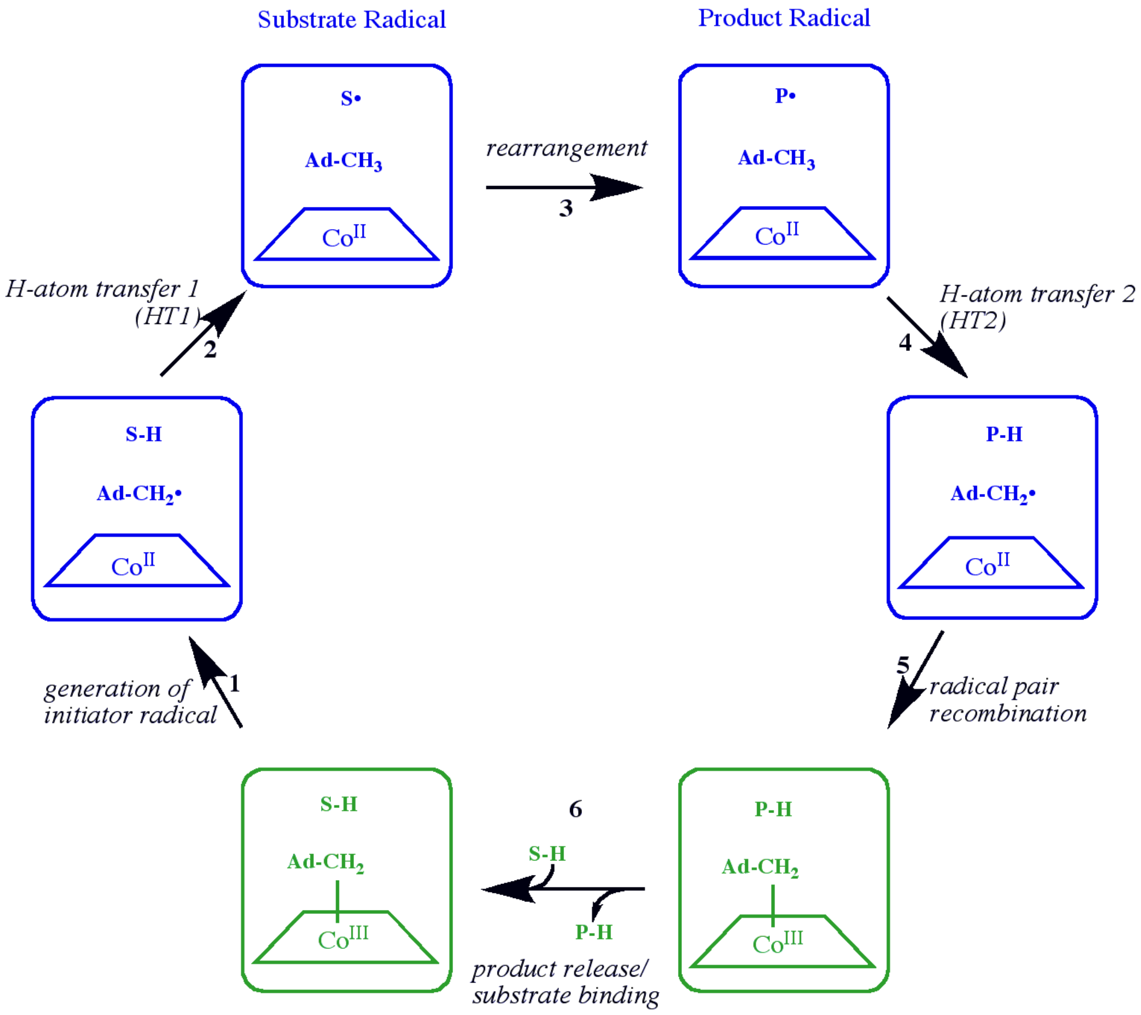

Figure 1.5. Minimal mechanism for EAL catalytic cycle.[61]The 6-step reaction cycle illustrates the Co-C bond homolysis with generation of Co(II) and an organic radical (1), the formation of the substrate radical (2) and quenching of the product radical (4) upon hydrogen transfer with the 5’-deoxy-adenosine, substrate radical rearrangement into product radical (3), and Co-C bond reformation (5) with product release and repopulation with substrate (6).

1.1.2.4. Catalysis and Dynamics

Like all catalysts, enzymes are designed to increase the reaction rate by lowering the transition state energy and thus the activation energy between reactants and products. In an exceptional way, enzymes accelerate reaction rates by 6-12 orders of magnitude relative to uncatalyzed reactions under similar conditions.[3] Remarkably, EAL has found a way to perform at the upper end of the scale. The low dissociation energy of the Co-C covalent bond in the AdoCbl facilitates the catalytic mechanism involving unusual or difficult reactions. It has been reported that the AdoCbl-dependent isomerase class accelerate the cleavage of this bond with a rate increase of 10^{12} times.[65-67]

In order to achieve lower energy barriers, it was proposed that during the reaction EAL undergoes specific configurational changes.[68] Moreover, these changes are proposed to be coupled to both the reaction and surrounding solvent. It is well established that, folded native state of the proteins is strongly controlled by both intramolecular interactions and dynamics of hydration water through a series of interactions that couple to maintain the protein structure and function integrity.[69-75] The latest studies towards understanding the molecular basis of EAL catalysis by using low-T electron paramagnetic resonance (EPR) spectroscopy include advances in characterizing the kinetics and mechanism of particular steps in the catalytic cycle with insights on the effect that the solvent and surface fluctuations have on the catalysis.[61, 76, 77] The solvent environment around EAL was characterized in the low-temperature (T) regime and two phases with tunable solvent dynamics were identified in the presence of cosolvent. (Figure 1.6) [78, 79] In the presence of a cosolvent the hydration layer or protein associated domain (PAD) is surrounded by a second phase, the mesodomain, whose volume is controlled by the concentration of cosolvent. The PAD solvent structure and dynamics are dominated by the confinement effects of the ice boundary transmitted through the mesodomain and can therefore be controlled by the mesodomain volume. The modulation of the effects is qualitatively associated with the T of the order-disorder transition (T_{ODT}) in the PAD structure.

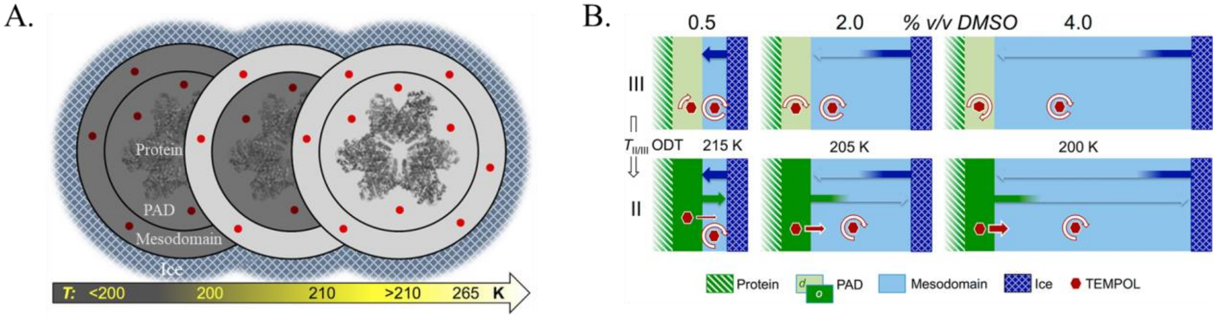

Figure 1.6. Solvent environment around EAL. A. Model for solvent phases around EAL protein; Mobility of the spin probe (red dots) is increased with increasing T (indicated by the arrow) from all solid (dark grey) to fluid (light gray).[78] B. Model for solvent dynamics and confinement effects in the protein-PAD-mesodomain-ice system.[79] The effect of the ice boundary region is lost with increase in the mesodomain volume (% v/v DMSO) and that is observed through a shift in the T_{ODT} to lower T values.

These observations have been unified with the EAL kinetics of the radical rearrangement step for ethanolamine substrate reported by Kohne et al., which have shown a piecewise-linear Arrhenius dependence from room T to 203 K, that is punctuated by a bifurcation and kinks (transition) in the narrow T-range of $220>T\geq217$ K.[68, 76] These results have identified the T_{ODT} as the region of bifurcation which is indicative of a strong contribution from protein-solvent coupling to the protein configurational dynamics that guide the reaction of breaking down aminoethanol.

1.1.3. Bacterial Microcompartments

Bacterial microcompartments (BMCs) are self-assembling protein-based organelles found in bacteria that encapsulate the set of enzymes necessary to perform a specific function. Based on the processes they carry out there are two main categories, anabolic carboxysomes and catabolic metabolosomes. The only anabolic BMC discovered so far is the carboxysome with role in CO_2 fixation.[80] The catabolic BMCs provide optimal metabolism of different organic compounds such as EA, 1,2-propandiol, choline and fucose/rhamnose through a specific pathway for aldehyde production by encapsulation of the necessary enzymes and channeling the intermediates in the catalytic cycle.[19, 34, 37, 81] The improved enzymatic reaction efficiency in the metabolic pathway is done by confining and thus concentrating the enzymes, metabolites and cofactors, enhancing the metabolism.[82] In addition, the BMC proteinaceous layer is thought to act as a barrier for metabolites, thus sequestering the toxic and volatile products, limiting detrimental processes.[37] The shell is 3 to 4 nm thick and 80 to 250 nm in diameter with a polygonal structure and consists of an assembly of 5000 to 20000 structural and encapsulated proteins. [33, 83] Although, the BMCs present high diversity through the structural and functional variety of encapsulated proteins, they display a conserved architecture. Three types of proteins have been reported to compose these organelles, BMC-H, BMC-T and BMC-P.[34] The most abundant, BMC-H, is a homohexamer that together with BMC-T, a pseudohexamer of a trimer of dimers with a central pore, forms the facets of the shell. In addition, BMC-P, a pentameric protein, closes the icosahedral shape of the BMCs by completing the vertices.

The common feature of metabolosomes is the core biochemistry of the pathway, which is defined by a signature enzyme, an aldehyde-generating catalyst. Usually expressed in the presence of the metabolic compound, BMCs enable growth in a nutrient depleted environment, affording a competitive advantage to bacterial pathogens.[37] In the EA metabolism, acetaldehyde has been reported to be a volatile and toxic intermediate for the cells. [30] However, bacteria developed the ability to grow on EA, and this was proven to be possible in the presence of BMCs.[30, 32] These are based on ethanolamine utilization pathway (Eut BMC) and encapsulate the set of enzymes for the EAL catalytic cycle, protecting the cell from the acetaldehyde intermediate. Organisms that have been shown to express these Eut BMC, such as *C. perfringens, S. enterica*, *E. coli*, *L. monocytogenes* and *Klebsiella*, have a negative impact on human health as they have been implicated in conditions ranging from food poisoning to colon cancer.[20, 38, 84]

The quaternary structure of BMC-T type proteins (EutL, EutM, PduA, PduB, PduT) has been observed by crystallographic studies to present pores that are thought to control transport through passive or dynamic gated mechanisms.[34, 85, 86] These shell proteins serve various functions within the shell as studies on a similar class of BMCs, namely the propanediol utilization (Pdu) BMC, have demonstrated a selective flux for substrate versus the toxic intermediate across the PduA protein due to the polar character of its pore. The polarity produces a low energy barrier that disfavors the passage of the toxic propionaldehyde and allows only the 1,2- propanediol transport.[87] However, it is not known how the Eut BMC mediates transport of substrate and products through its proteins, across the shell. Additionally, how certain products are sequestered inside the organelle is not well understood. These Eut BMCs are a topic of ongoing research due to their potential in therapeutics and new approaches to engineering multi-enzymatic synthesis. Moreover, the characterization of the *S. typhimurium* native Eut BMC is lacking.

The *eut* operon encodes for five proteins (EutS, EutM, EutN, EutL and EutK) that are shown to build the Eut BMC shell.[36, 40] (Figure 1.1) These proteins adopt a hexameric (EutS, EutM, EutL and EutK) or a pentameric (EutN) structure, and with the exception of EutK, they all oligomerize in solution at physiological pH.[37, 85] Additionally, it has been observed that each of the EutM, EutL and EutS BMCs crystallizes in a 2-dimensional (2D) sheet, indicating lateral interactions between identical proteins. However, a 2D structure of both EutL and EutM proteins was not successfully obtained.[37]

1.1.3.1. The BMC structural protein EutS

The EutS BMC protein consists of 111 amino acids in its monomeric form and has been observed to crystallize in a homohexameric structure. (Figure 1.7) In particular, the EutS crystal structure showed both a flat structure and a structure with an asymmetric assembly of the monomers into the homohexamer that deviates from the flat configuration by a 40° angle. This angle describes a concave bent between two sets of trimers from the hexameric appearance. The bend has been proposed to form the edges in the BMC shell structure, and it is suggested that this feature allowed to engineer BMCs in cells from EutS expression alone.[85, 88]

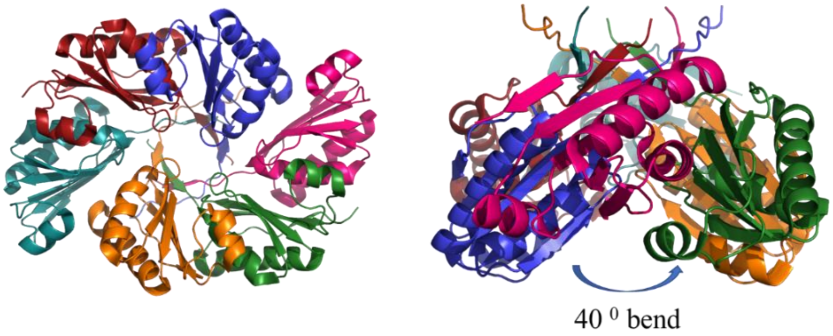

Figure 1.7. Structure of EutS BMC from *E. coli* determined by X-ray crystallography at a resolution of 1.65 Å (PDB file 3I96).[85] PyMol cartoon of the EutS homohexamer showing the subunits in different colors: top view on the left and side view showing the 40 ^{0} bend on the right.

1.1.3.2. The BMC structural protein EutL

Among the Eut BMC proteins, EutL is the largest protein with 217 amino acids in its sequence, and its monomer is formed of two similar domains. (Figure 1.8 A) The crystal structure of the *E. coli* homolog revealed a trimeric assembly into a hexagonal structure, with a central pore defined by two large flexible loops that belong to each of the two domains, where one loop is occupying the central region of the protein.[89] EutL presents two conformational states, closed and open, as indicated by distinct crystallizations of the protein and it is suggested to have implications for a selective transport function. (Figure 1.8 B and C) In the closed state, the pore has a diameter of 2.2 Å between the narrowest points while in the open state, the rearrangements in these loops create a central triangular pore of side 11 Å, and 8 Å between its narrowest points.

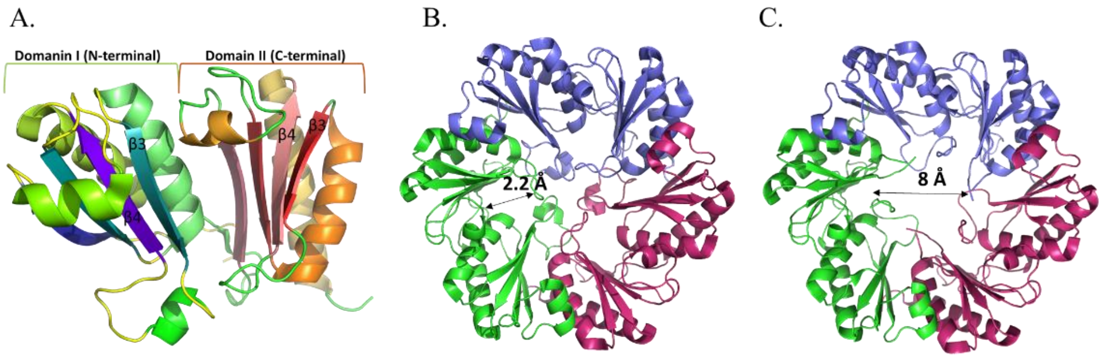

Figure 1.8. Structure of EutL BMC from *E. coli* determined by X-ray crystallography at a resolution of 2.3 Å. A. PyMol cartoon of the EutL monomer in the closed form showing the two domains and associated loops; B. The closed and C. open conformations. The trimers are highlighted using different colors. The PDB files used to build the BMC are 3I82 for closed structure and 3I87 for the open structure.[85]

It has been shown that α-helix conformation is changed in the presence of Zn.[90] In the EutL, Zn stabilizes the open conformation by binding the protein at three sites and triggering a conformational change in the central loop.[83] Studies on *C. perfringens* EutL demonstrated that in the closed conformation the central region is stabilized by the interaction of three conserved aromatic rings, each of which are Tyr residues, and by H-bonds between polar residues. [91] Two EA can bind in the small pores in the closed conformation at specific sites that are not subjected to fluctuations that would facilitate the transport of this molecule. [89, 91] It is argued that EA transport is more energetically favored by the EutM pore rather than EutL pores of the closed conformation, whose diameter is of 8.6 Å. Therefore, it was proposed that EA has a negative allosteric regulation of the central pore opening in EutL, because its binding stabilizes the closed conformation. It is suggested that the EutL pore is closed at physiological concentrations of EA. However, when EA is depleted EAL becomes inactive due to coenzyme B_{12} damage. Reactivation of the cofactor requires its transport across the shell or ATP uptake, possibly through the EutL central pore.[92] It was proposed that opening of this pore is not susceptible to aldehyde escape from the BMC because EA depletion stops the volatile and toxic compound formation, allowing only for the uptake of the necessary products. These findings however have not revealed the mechanism of opening and the transport function for the EutL BMC. How the opening conformation is triggered remains an unanswered question.

1.2. Experimental techniques

1.2.1. Continuous Wave EPR spectroscopy

CW-EPR spectroscopy is used to study chemical species with unpaired electrons such as organic or inorganic radicals and transition metal complexes to gain insights into the physical and chemical properties of the system and its surrounding environment.[61, 78, 93-99] In EPR, the interaction of electromagnetic radiation with magnetic moments of unpaired electrons in external magnetic field is observed. For a free electron in an external magnetic field (*B_0*) two non-degenerate energy states are available. Transitions between these energy states can be driven by electromagnetic radiation with frequency, ν, if the energy of that radiation matches the energy separation between the states. (Figure 1.9 A) This can be described by the resonance condition:

$$\Delta E = h\nu = g_e \beta B_0 \tag{1. 1}$$

where ΔE is the energy separation between the two states, h is the Planck's constant, g_e is the electron g-factor and β is the Bohr magneton. EPR spectra are usually generated by sweeping the B_0 field while keeping the radiation frequency constant.

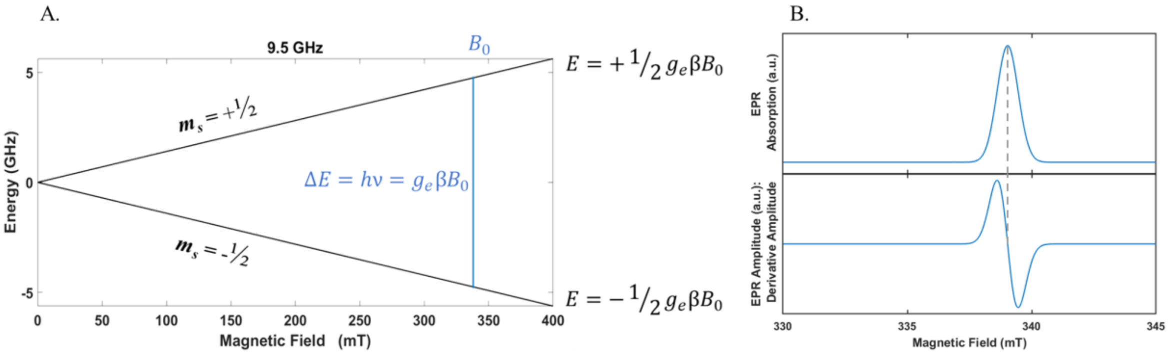

Figure 1.9. The energy diagram for an unpaired electron with *S=1/2* and the EPR signal recorded as the first derivative of the absorption. A. For X-band microwaves (9.5 GHz) and electrons with a g factor near the free electron g_e=2.0023, resonance occurs at ~340 mT. The energy diagram shows the Zeeman effect: in an external magnetic field *B_0* along z axis, the electron magnetic moment aligns parallel ($m_s = -1/2$) and antiparallel ($m_s = +1/2$) with the field giving two discreet energy states; the gap between the two states depends on the field strength. B. The EPR signal is recorded as a derivative of the absorption. This is done through phase sensitive detection of a field modulated EPR signal at 100 kHz.

The EPR signal can be represented by quantum mechanics through the Hamiltonian that describes the interactions of the unpaired electrons with their local environment. The eigenvalue of the spin operator $\boldsymbol{S}$ is the quantum number m_s that quantizes the electron spin angular momentum. The value of m_s specifies the orientation of the electron spin in an external magnetic field and identifies its specific energy state. These energy states are described by a total Hamiltonian ($\boldsymbol{H}$) that includes terms for each type of interaction the unpaired electron may experience:

$$\boldsymbol{H} = \boldsymbol{H}_{EZ} + \boldsymbol{H}_{NZ} + \boldsymbol{H}_{HFI} + \boldsymbol{H}_{DD} + \boldsymbol{H}_{exch} \tag{1. 2}$$

The first two terms refer to the electron ($\boldsymbol{H}_{EZ}$) and nuclear ($\boldsymbol{H}_{NZ}$) Zeeman interactions. The hyperfine interactions (HFI) between electrons and nuclei are described by $\boldsymbol{H}_{HFI}$. The last two terms describe the dipole-dipole ($\boldsymbol{H}_{DD}$) and isotropic exchange ($\boldsymbol{H}_{exch}$) interactions between pairs of electrons. The Zeeman terms cause non-degeneracy in the energy states according to $2S+1$ for electrons and $2I+1$ for nuclei where S and I are the total electron and nuclear spins, respectively. (Figure 1.10) The Zeeman terms $\boldsymbol{H}_{EZ}$ and $\boldsymbol{H}_{NZ}$ describe the available energy states in terms of the spin operators $\boldsymbol{S}$ and $\boldsymbol{I}$ according to:

$$\boldsymbol{H}_{EZ} + \boldsymbol{H}_{NZ} = g_e\beta_e B\boldsymbol{S} + g_n\beta_e B\boldsymbol{I} \tag{1. 3}$$

The nuclear hyperfine interaction between the electron and the nuclei is given by the $\boldsymbol{H}_{HFI}$ term:

$$\boldsymbol{H}_{HFI} = \boldsymbol{SAI} \tag{1. 4}$$

that describes the interaction through a coupling matrix (A) that consists of isotropic and anisotropic terms. The isotropic part (a_{iso}) defines the magnitude of the hyperfine interaction and describes the degree of separation between the nuclear energy states. The anisotropic part of A originates from through space dipole-dipole interactions with nuclei described by:

$$A_{dipolar} = g_e\beta_e g_n\beta_n \frac{3cos^2\theta - 1}{r^3} \tag{1. 4}$$

where θ is the angle between the inter-dipole vector and the external field B_0. Considering that the nuclear magnetic moment creates a local field at the electron, then this field can add or subtract from the external field in an orientation dependent manner.

When two unpaired electrons are in proximity, at a distance r, they interact through the same dipolar coupling mechanism, described by:

$$\boldsymbol{H}_{HFI} = \boldsymbol{S_1} D \boldsymbol{S_2} \tag{1. 5}$$

where $\boldsymbol{S_1}$ and $\boldsymbol{S_2}$ are the spin operators for the two electrons and D describes the dipole-dipole interaction. This interaction broadens the spectrum and lowers the amplitude of the absorption in a distance dependent manner ($\sim r^{-3}$). Therefore, in equation 1.5 the nuclear contribution $(g_n \beta_n)$ is replaced by another unpaired electron.

The two electrons also experience an exchange interaction, described by:

$$\boldsymbol{H}_{exch} = S_1 J S_2 \tag{1. 6}$$

where $\boldsymbol{J}$ is the coupling component described by an isotropic and anisotropic term. The isotropic part, $J_0 = 1/3 tr(\boldsymbol{J})$, characterizes a weak chemical bonding or antibonding caused by overlap of orbitals or Coulomb interactions. The anisotropic component, which is usually neglected, comes from the spin-orbit coupling.

1.2.1.1. Paramagnetic molecules: TEMPOL and 4-Maleimido-TEMPO

The nitroxide radicals used in this study, either free in solution (spin probe, TEMPOL) or attached to the protein (spin label, 4MT via site directed spin labeling) (Figure A.2 in Appendix A), add to the spin Hamiltonian the hyperfine and dipolar interaction terms described below. The spin probe TEMPOL has been previously studied by using EPR techniques to understand glass formation and phase transitions by exploiting the T-dependent of its mobility in solutions.[100-

103] The spin label nitroxide is used to understand both structure and dynamics of biomacromolecules with different degrees of complexity.[95, 104, 105]

Both molecules are stable radicals which have an unpaired electron that interacts with the nucleus of the nitrogen atom through hyperfine coupling. Because ^{14}N has nuclear spin I=1, and the number of energy states is given by 2I+1, this leads to splitting in each of the two electron spin energy states into three non-degenerate states, shown in the energy level diagram in Figure 1.10. The unpaired spin density in the ^{14}N p orbital leads to anisotropy in the coupling through the orientation dependence of the orbital with respect to the external magnetic field as expressed in Eq 1. 5. The local fields created at the electron by the different orientations of the orbital angular momentum of the equivalent nitroxides give small shifts in the resonance lines that are observed in the EPR spectrum as broadenings. (Figure 1.10) The perturbations in the Zeeman energy states given by the anisotropic hyperfine constant is presented in the energy level diagram through the thicker lines that describe angle variations from 0° to 90°. The isotropic hyperfine constant (a_{iso}) is not orientation depend and describes the degree of separation between the 3 energy states with the magnitude $a_{iso} = \frac{A_x+A_y+A_z}{3}$. Consequently, three transitions will occur according to the selection rules, $\Delta m_S=\pm 1$ and $\Delta m_I=0$, and correspond to three resonance lines (ΔE_1, ΔE_0 and ΔE_{-1}).

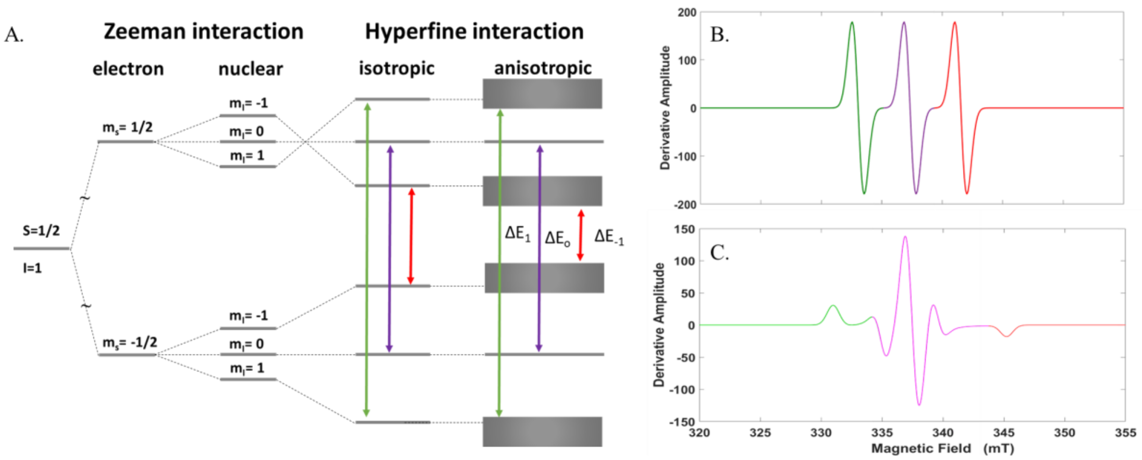

Figure 1.10. A. Energy level diagram for the resonance lines in a nitroxide spin label that arise from the interaction of an unpaired electron with the local nitrogen atom: S=½ (m_s=-½, ½); I=1 (m_I=-1, 0, 1). In panels B and C are the corresponding EPR signals where: in panel B the anisotropy is averaged by the rapid rotation of the spin probe yielding an isotropic spectrum; in panel C the orientation dependence is visible in the slow motion regime yielding a powder spectrum where the anisotropies are emphasized.

The nitroxide EPR spectra are dependent on the Zeeman and hyperfine anisotropies. In the absence of an external field the free electron that resides on a molecule has a total magnetic moment with contributions not only from its intrinsic spin angular momentum but also from the orbital angular momentum. This total magnetic moment creates a local field at the electron and the effect of this field can be described by deviations in the g values from g_e. The orientation of the molecule and thus the total magnetic moment creates anisotropy in the system. Additionally, rotational tumbling motions of the probe contributes to the broadening effects. (Figure 1.11) The tumbling motions depend on the solution viscosity which change as a function of T. The motional regimes are described through rotational correlation times that correspond to the time period over which the nitroxide radical completes a single rotation. In frozen samples, high viscosity, the slow motional regime manifests the powder pattern spectrum with full contributions from the Zeeman and hyperfine anisotropies. At high T and low viscosity, where the motions are at the same magnitude as the hyperfine interaction, the fast tumbling averages out the anisotropies of the interactions and the lineshape shows symmetry in the derivative of the absorption lines with reduced splitting. The sensitivity of the CW-EPR at X-band technique to the tumbling motion of the nitroxide molecules range from 10^{-11} to 10^{-7}.

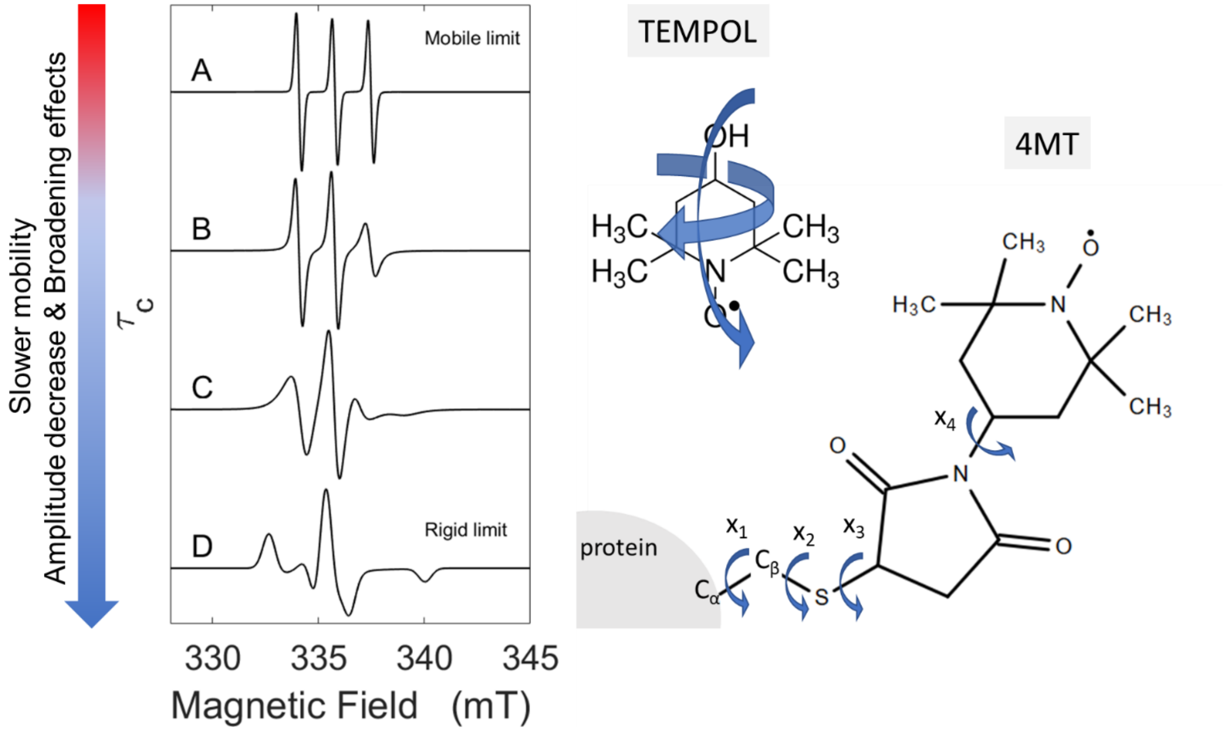

Figure 1.11. Effect on EPR spectra from the motions of the spin systems. (left) The arrow indicates decrease in motion due to *T* or to restrictions imposed by the environment. Possible scenarios: nitroxide in solution (A) or, bound to a polypeptide (B) or folded polypeptide (C) and finally nitroxide in frozen solution (D). The two nitroxides are shown with their possible rotations indicated by the arrows (right).

1.2.1.2. Paramagnetic species in EAL, EPR spectroscopy

There are four paramagnetic species that form during AdoCbl-dependent EAL catalysis under 2-aminorpopanol substrate which are illustrated in the minimal mechanism in Figure 1.5. Three states within the cycle show the free radical species and they identify within three radical pairs between the low spin Co(II) from cob(II)alamin (Cbl(II)) and three radicals Ado$^{\bullet}$, substrate radical and product radical. The Cbl(II)-substrate radical pair is the only pair in the cycle to give an EPR signal.[57, 106-108] The rate of radical pair state formation is higher than the rate of product formation.[108] Therefor, freeze quenching technique at 140 K allows for trapping the radical pair state which accumulated during steady-state turnover at room temperature when substrate is in excess.[61] This enables time dependent measurements of the forward reaction of the cryotrapped radical state initiated at low temperature by a *T*-step. At cryogenic temperatures, the fluctuations in configurational states in EAL are selectively impacted which allow individual chemical steps from the reaction cycle to be studied.

The low spin Co(II) arises from Co(III) following homolysis and it has an unpaired electron (S=1/2 and I=7/2) while the substrate radical has a free electron localized on the C1 atom (S=1/2). In uncoupled Cbl(II), the lineshape of Co(II) is well resolved showing a characteristic 8-line splitting in the EPR signal from the electron-nuclear spin hyperfine interaction. Moreover, the delocalization of the electron spin in the $d_z{}^2$ orbital gives an additional superhyperfine interaction with the nuclear spin of the neighboring nitrogen atom (I=1) from the DMB tail of cobalamin which further splits each of the 8 lines into triplets. (Figure 1.12 A) The axial symmetry of this hyperfine interaction gives a considerable anisotropic broadening in the XY plane at low field.[109] However, in the radical pair (Figure 1.12 B), the organic radical feature at g=2.015 (335 mT) and the low field Co(II) peak at g = 2.3 are split due to coupling of the d_z electron on Co(II) with the free electron of the substrate radical. In the radical pair EPR signal the low field Co(II) hyperfine splitting is unresolved while the high field can still be observed in the region where the substrate radical signal does not dominate. The splitting and broadening of the signal arise from the electron-electron dipolar interaction and isotropic exchange between the two paramagnetic species. Simulations of EPR spectra for the radical pair resolved distances between Cbl(II) and substrate radical as well as magnitudes for the isotropic exchange interaction from the dipolar interaction coupling constant, *D*. For our system, Cbl(II)- 2-aminopropanol substrate radical, the distance between Co(II) center and C1 atom on the substrate was determined to be 11 Å and the isotropic exchange interaction constant, $|J_0|$=324 MHz.

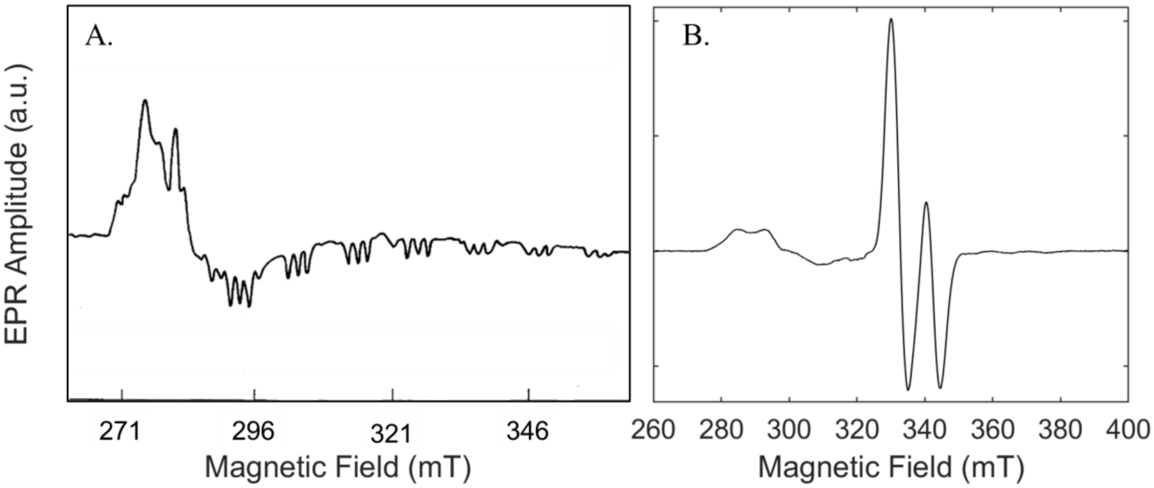

Figure 1.12. EPR spectrum of cobalamin and cryoptrapped Cbl(II)-2-aminopropanol substrate radical pair. Figure adapted from Pilbrow et al. to illustrate the hyperfine contribution in the cobalamin formed from AdoCbl within the enzyme ribonucleotide reductase. Measurement conditions:77 K; 9.015 GHz microwave frequency; 8.0 mW microwave power.[109, 110] B. The cryoptrapped Cbl(II)-2-aminopropanol substrate radical pair in EAL. Measurement conditions:120 K; 9.45 GHz microwave frequency; 2.0 mW microwave power; 10 Gauss magnetic field modulation; 100 kHz modulation frequency; 2600-4000 Gauss sweep width; 4 averaged scans.

1.2.1.3. Spin-Lattice Relaxation

At thermodynamic equilibrium the population difference between the two electron states can be described using the Maxwell-Boltzmann distribution:

$$\frac{n_u}{n_l} = e^{-\Delta E/k_B T} \qquad (1.\ 7)$$

where k_B is the Boltzmann constant and n_u and n_l are the spin populations in the upper and lower states, respectively. After resonant absorption of microwaves, the time associated with recovery of the equilibrium distribution depends on the interaction of the electron with the local environment. Spin-lattice relaxation is defined as the recovery of the equilibrium Boltzmann distribution.[97, 111] The time constant associated with this relaxation process is spin-lattice relaxation time, T_1. Depending on the nature of the local environment, excited unpaired electrons will dissipate their energy into their surroundings at a different rate which can be described in term of the recovery of the alignment of the electron spins with the external magnetic field:

$$M_z(t) = M_0(1 - e^{-t/T_1}) \qquad (1.\ 8)$$

where $M_z(t)$ is the observation of the magnetization in the direction of the external field at time t and M_0 is the equilibrium magnetization.

The T_1 relaxation is reflected in EPR spectra through changes in lineshape and intensities and these provide information about processes such as chemical reactions, intramolecular motions, electron exchange or transfer between species and local concentrations of the radical species.

1.2.2. Site Directed Spin Labeling

Site directed spin labeling (SDSL) is a technique in which a stable free radical is chemically tethered to a defined site in a biomacromolecule. The labeling is commonly through covalent bonding to the sulfhydryl group of cysteine residues. (Figure 1.11 lower right cartoon) SDSL uses small probes with minimum perturbation on the surroundings. These probes give access to site specific details of protein dynamics. Among the spin labels available for these studies the nitroxide 4MT is used. (Figure A.2 panel B in Appendix A)

EPR analysis of nitroxide 4MT can give information on the dynamics and solvent accessibility of the spin label side-chain, polarity of its environment, and intramolecular distances between at least two spin labels or between the spin label and a bound metal ion.[94, 95, 112] The mobility of the spin label is encoded in the shape of the EPR resonance lines. (Figure 1.11 left) The constraint on motion is visible through the line broadening of the spectra. In 4MT, the motion is allowed through rotations around the angles shown in Figure 1.11, lower right cartoon. If two conformations (rotameric states) of the spin label linked in the peptide are allowed, then these will appear as splitting of the lines in the spectra. From the isotropic hyperfine interaction, all lines will be equally broadened.(Figure 1.10 B) The anisotropic component will broaden the spectrum (Figure 1.10 C) depending on the nuclear and electron magnetic dipoles alignment with the field, given by the θ angle. (Equation 1.5) Distance measurements provide information on both structure and function. Pairs of spin labels that are between 8 to 80 Å apart influence each other's magnetic field through the dipolar interaction. This interaction is proportional to ${}^{1}/_{r^3}$, where r is the inter-dipole distance. (Equation 1.5) CW-EPR is sensitive to distances within the range of 8-25 Å. The distance information is depicted in the line broadening accompanied by decrease in amplitude. This distance information as well as information on motions of the spin label can be extracted from simulations and fitting of the spectra using quantum-mechanical models.

1.3. Outline

The work presented in the chapters that follows focus on understanding the mechanism of AdoCbl-dependent EAL catalysis and pathway, and the contribution of the structural BMC proteins EutS and EutL in the eut pathway, as a direction towards therapeutic development. The molecular basis of EAL catalysis is investigated by using low-*T* EPR spectroscopy and include advances in characterizing the kinetics and mechanism of particular steps in its catalytic cycle with insights on the effect that the solvent and surface fluctuations have on the catalysis. Chapter 2 demonstrates that solvent dynamics and glass transition around the enzyme are "tuned" by the presence of substrate 2-aminopropanol alone or in combination with dimethylsulfoxide (DMSO) and *T* variation. The results are further used in chapter 3 to investigate the impact that solvent-protein dynamics coupling has on the kinetics of the resolved protein configurational change and substrate radical rearrangement reaction steps. This is achieved by low-*T* kinetics experiments (210-240 K) of the cryotrapped cob(II)alamin-2-aminopropanol substrate radical pair decay with and without % v/v DMSO in the reaction solution. Observed variations in the EPR amplitudes of EAL-bound paramagnets [cob(II)alamin and substrate radical] with added % v/v DMSO enabled investigations of *T*-dependence of the spin-lattice relaxation which corelates solvent dynamics around EAL to motions in the protein interior at the active site in chapter 4. The dissertation also includes preliminary studies towards characterizing Eut shell proteins and the assembly mechanism and structure of the Eut BMC. In chapter 5 the SDSL CW-EPR technique pioneer the investigations on the shell structure and assembly mechanism of EutS BMCs, and transport properties for EutL. The studies presented herein initiate a comprehensive characterization of the solvent-protein-catalysis dynamical coupling in EAL and enable studies towards understanding the shell structure and assembly mechanism of EutS BMCs, and transport properties for EutL.

Chapter II

Solvent dynamics around EAL in 10 mM 2-aminopropanol with 0 % and 2 % DMSO

2.1. Introduction

The multitude of events that couple to maintain protein functional and structural integrity are complex and include Coulombic and hydrophobic interactions as well as formation and breaking of hydrogen bonds between water molecules and between water molecules and residues of the biomacromolecule.[69-74] The network of water immediately surrounding the protein, also termed the hydration layer that is roughly two water molecules in thickness, presents a structure which deviates from bulk water. The surface residues of the biomacromolecule induce structural heterogeneity to the water layer through electrostatic interactions and hydrogen bonding.[72] Dynamics of this hydration water were proposed to be considerably slower than the bulk water and to influence the protein conformational dynamics.[70] Additionally, the protein motion induces changes in hydration dynamics and further in the bulk water, extending up to 20 Å from the protein surface.[78, 113] A strong coupling of the dynamics in the water-protein system through cooperative interactions is achieved via the ordered hydration water which acts as a bridge between the bulk and protein surface and allows the control of protein configurational fluctuations; a necessary factor in the dynamical flexibility of the biomolecule which enables proper function.[72-75, 78, 79] Therefore, an optimal level of hydration was well established for protein to function. However, in conditions of low hydration level, enzymatic activity, although impaired, was still observed, the catalysis being activated via a hydration-mediated internal molecular motions and substrate/cofactor diffusion.[114] Interestingly normal activity is not only restored by increasing hydration but also by the presence of organic solvents [115] which act as substitutes for water and have even been shown to improve catalyzed reactions.[70, 71] Thus, not only the hydration layer, but also the presence of cosolvents and other biomolecules in the bulk water can influence protein motion. While it is clear that enzyme activity may suffer due to low hydration levels and decreased diffusion of substrates/cofactors into enzyme catalytic centers, it is not clear how enzyme dynamics, catalytic reaction and chemical steps are driven and controlled by solvent dynamics.

The B_{12}-dependent EAL enzyme is involved in microbial aminoethanol metabolism and has been associated with microbiome disease conditions in the human gut.[23, 116, 117] Studies towards understanding the molecular basis of catalysis for EAL from *Salmonella typhimurium* by using low temperature (T) electron paramagnetic resonance (EPR) spectroscopy include advances in characterizing the kinetics and mechanism of particular steps in the catalytic cycle with insights into the effect that the solvent dynamics has on the protein fluctuations and function.[61, 76, 77] The kinetics of the radical rearrangement step for ethanolamine substrate measured by using time-resolved, full-spectrum EPR spectroscopy, show a piecewise-linear Arrhenius dependence from room T to 203 K, that is punctuated by a bifurcation and kinks (transition) in the narrow T-range of $220>T\geq217$ K.[68, 76] Additionally, studies of solvent dynamics around EAL by using TEMPOL spin-probe EPR in frozen polycrystalline aqueous solution have shown that in the presence of cosolvent the environment affords two phases around the protein.[78] The cosolvent assets in forming a “mesodomain” surrounding the protein hydration layer or protein associated domain (PAD), a second phase whose volume is controlled by the concentration of cosolvent. The mesodomain phase is an interstitial glassy phase with high viscosity and lower melting T that is formed by solutes or cosolvents as a consequence of their exclusion from the ice crystallite regions during freezing.[78, 118-120] At freezing conditions TEMPOL is also excluded from the ice into the domains around the protein. Thus, TEMPOL maps the solvent of the phases in the vicinity of the protein outside the ice crystallite region.[78, 79, 121] The results have shown that the solvent structure and dynamics of the PAD are influenced by the confinement effects of the ice boundary transmitted through the mesodomain.[79] The extent of these effects on PAD depends on the mesodomain volume. The results show a correspondence of the *T* of the kinetic transition in aminoethanol with an order/disorder transition (ODT) in the PAD that surrounds EAL, which can be tuned (*T* decreased) by using added (0.5- 4.0% v/v) dimethylsulfoxide (DMSO). [79, 122]

Here we address the dynamics of solvent phases in the immediate environment of the B_{12}-dependent EAL enzyme in solution of 2-aminopropanol by using EPR spectroscopy of the spin probe, TEMPOL. The solvent dynamics are varied by using DMSO, and measured, in the protein-associated- and meso- domains that surround EAL in frozen aqueous solution. The spin probe results indicate transition regions for 0% (230-235 K) and 2% (210-215 K) v/v DMSO. The results provide support for the method of study and applicability using different cosolvents and enable the investigations of the solvent-enzyme-reaction coupling mechanism in EAL through the tunability of the solvent-protein dynamics.

2.2. Materials and Methods

2.2.1. Protein and EPR sample preparation

The EAL enzyme was expressed in the *Escherichia coli* overexpression system by cloning its coding sequence from *S. typhimurium* into the pBR328 plasmid. [29] The protein was isolated and purified by ammonium sulfate precipitation as described previously [29, 123] with modifications. [61] The specific enzymatic activity of purified EAL with aminoethanol as substrate assayed by the alcohol dehydrogenase/nicotinamide adenine dinucleotide-coupled spectrophotometric assay was 20-30 µmol min-1 mg-1 at 298 K and 1 atm. [124]

The samples for EPR spectroscopy were prepared in 10 mM potassium phosphate buffer (pH 7.5) and included 20 µM purified EAL (120 µM active sites), 10 mM (S)-2-aminopropanol, and 0.2 mM TEMPOL spin probe in a final volume of 300 µL. When present, DMSO was added to 2 % v/v to the sample final volume size. The samples were aerobically prepared in small vials on ice. The components were mixed, loaded into 4 mm outer diameter EPR tubes and rapidly submerged in isopentane pre-cooled to 140 K in liquid nitrogen. The freezing method has a characteristic cooling rate of 10 K/s. [61] Samples were stored in liquid nitrogen.

All chemicals and reagents used are commercially available and they did not need further purification. DMSO (purity,≥99.9 %) was purchased from EMD Chemical, the deionized water (resistivity, 18.2 MΩ·cm) was obtained from a Nanopure system from Siemens, (S)-2-aminopropanol and TEMPOL (4-hydroxy-TEMPO) are products of Sigma-Aldrich. The EPR tubes were purchased from Wilmad-LabGlass.

2.2.2. Continuous Wave EPR spectroscopy

The CW-EPR spectra were collected by using a Bruker E500 ElexSys EPR spectrometer equipped with a Bruker ER4122 SHQE X-band cavity resonator. The temperature was controlled by using a Bruker ER4131VT temperature controller and cooling system that consists of a nitrogen gas flow through a coil immersed in liquid nitrogen bath contained in a 4 L dewar. Across the EPR sample cavity the temperature stability is within 0.5 K. [61] For each experiment, the readout on the controller was calibrated by using a 19180 4-wire RTD probe (± 0.3 K accuracy) and an ITC503 unit from Oxford Instruments as previously described. [61]

The experimental protocol was described in previous work. [78, 79, 96] In brief, after calibration the T was set at the lower or higher limits of the measurement range (200-265 K) and a first EPR spectrum was collected. Then the next temperature was set and before collecting the spectrum the system was left at least 5 min to equilibrate and the cavity retuned. This was repeated for the entire range with a 5 K step in *T*. A dummy sample which was lacking TEMPOL was measured in a similar matter at each *T* value for baseline correction. Samples were measured in both direction of increasing and decreasing *T* in the same day or after additional storage to confirm the absence of hysteresis in correlation times or component amplitudes. The EPR acquisition parameters used were: 9.45 GHz microwave frequency; 0.2 mW microwave power; 0.2 mT magnetic field modulation; 100 kHz modulation frequency, and 4-8 spectra were averaged at each *T* value.

2.2.3. EPR Simulations

The EPR spectra of the TEMPOL spin probe were simulated using the Chili algorithm in the EasySpin program (http://www.easyspin.org/). [125] The parameters and steps for the simulations are detailed in previous work. [78] Briefly, after baseline sample subtraction the EPR spectra simulations require two components each described by a set of *g* tensor (g_x = 2.0120, g_y = 2.0130, g_z = 2.0073) and ^{14}N hyperfine tensor parameters (A_x = 20.9, A_y = 19.8, A_z = 103.2 MHz), with a varying set of parameters - the correlation times ($\tau_{c,s}$, $\tau_{c,f}$) , weights (W_s, W_f) and the intrinsic line widths - for the slow-motional and fast-motional components. The two component simulations were performed by varying the set of parameters for one component at a time (each three times), with a final variation of both components simultaneously. The best fit parameters are used for the next increasing/decreasing *T* step as a starting point and then the next steps repeated.

2.3. Results

2.3.1. TEMPOL EPR line shape. Temperature dependence in frozen aqueous solution with EAL and 2-aminopropanol in the presence of 0 % v/v DMSO

The temperature dependence of the TEMPOL spin probe mobility is mapped by the EPR line shape within the range of temperatures of 190 - 260 K. In Figure 2.1 A this dependence is shown for EAL in the presence of 2-aminopropanol and 0 % v/v DMSO solution, at representative T values within the measured range. The dominant spectral features of the TEMPOL spectrum arise from the electron-nuclear hyperfine interaction of the unpaired electron spin (S = 1/2) with the ^{14}N nuclear spin (I = 1) which gives 2I + 1 EPR lines associated to the electron spin transitions between m_I = 0, ±1 energy states. At low T, below 225 K, the spectra are characteristic for the rigid-limit, powder pattern line shape which transition to motional-narrowed spectra at 230 K. Qualitatively, the z-component of the anisotropic hyperfine tensor, A_{zz}, characterizes the rigid-limit line shape by a spectral width of 2A_{zz} of 7.3 mT (or 205 MHz). At T > 230 K the line shape changes exhibiting narrowing of the overall spectral width given by narrowing of the m_I lines width. The increase in T starts the rotational, tumbling motion of the spin probe TEMPOL that leads to averaging of the g-tensor and electron-nuclear dipolar anisotropy which narrows the line shape.

2.3.2. TEMPOL EPR line shape. Temperature dependence in frozen aqueous solution with EAL and 2-aminopropanol in the presence of 2 % v/v DMSO

The EPR line shape of the TEMPOL spin probe in frozen aqueous solution with EAL, 2-aminopropanol and added 2 % v/v DMSO is presented at representative T values in Figure 2.1 B. Here, the rigid to mobile transition is marked by the T value of 210 K. At this temperature the rigid limit, powder pattern line shape is still observed. However, above 210 K the TEMPOL spin probe mobility is enabled and increases with T, averaging out the anisotropic effects which narrow the overall spectral width and hyperfine feature widths. At $T > 245$ K, the narrowing of the line shape due to fast motional regime gives a well averaged anisotropic interactions that reaches a spectral width that corresponds to the isotropic hyperfine interaction with $2A_{iso}$ of 3.6 mT (or 101 MHz) where A_{iso} is the isotropic hyperfine coupling constant. Figure 2.1 shows that the rigid to mobile transition and the line shape narrowing occur at different T values for the two conditions, with the 2 % v/v DMSO lowering the transitions by ~20 K relative to the 0 % v/v DMSO.

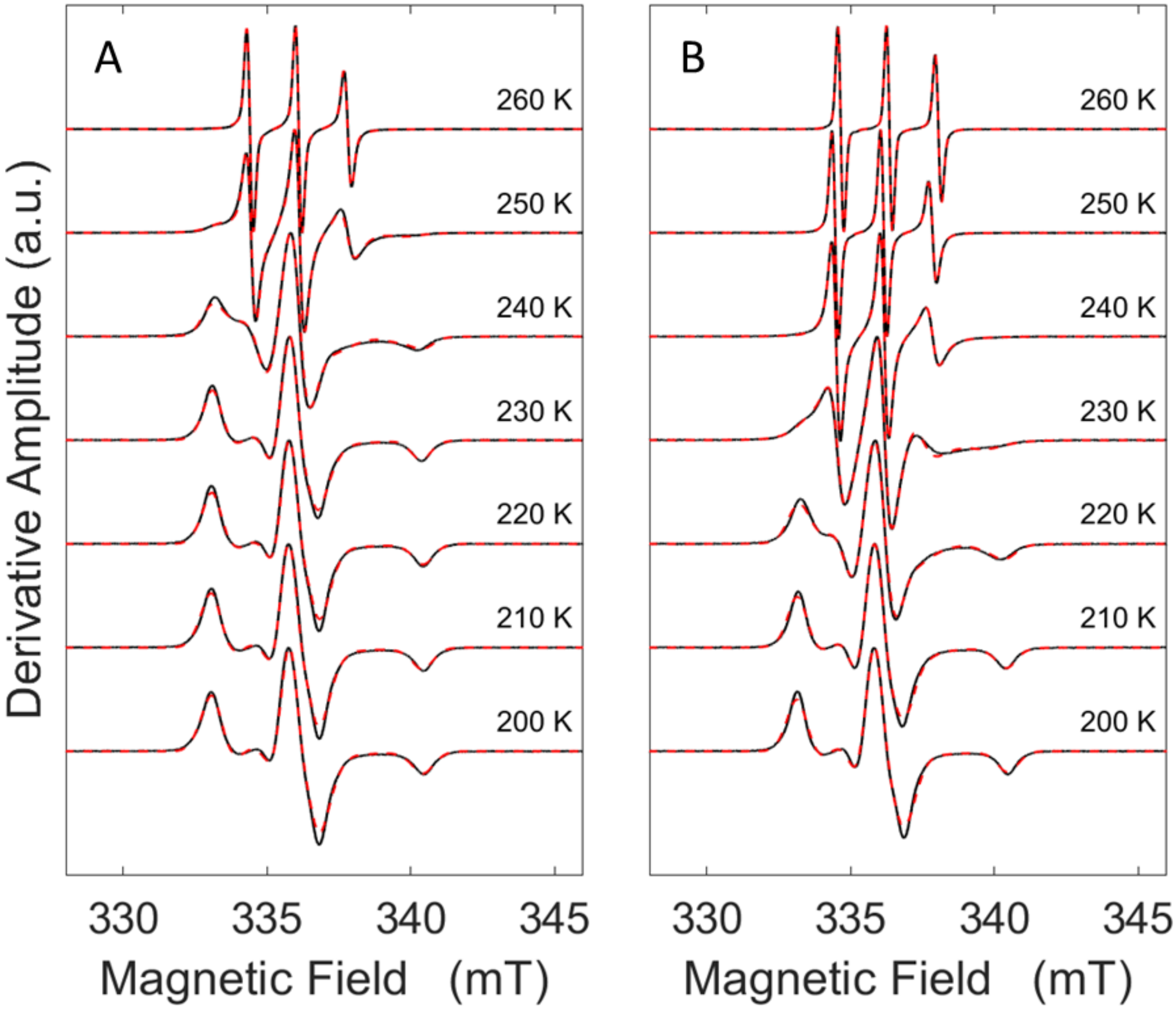

Figure 2.1. Temperature dependence of the TEMPOL EPR spectrum for the frozen EAL solution in the presence of 10 mM 2-aminopropanol at different added % v/v DMSO (black line): (A) 0 %; (B) 2%. EPR two-component simulations are overlaid (red line). Spectra are normalized to the central peak-to-trough amplitude.

2.3.3. TEMPOL rotational correlation times and normalized weights. Temperature dependence in frozen aqueous solution with EAL and 2-aminopropanol in the presence of 0 % v/v DMSO

Simulations of the TEMPOL EPR spectra gave information on the rotational correlation times (τ_c) and mobility components weights (W) of the spin probes as characteristics of the rotational mobility of the probe. A two-component behavior was indicated by the simulations characterized by $\tau_{c,s}$ with relatively large values (indicated as the "slow" component of tumbling) and $\tau_{c,f}$ with relatively small values (indicated as the "fast" component of tumbling), and associated weights, W_s and W_f. The temperature dependence of $\log\tau_c$ and W is presented in Figure 2.2 and is segmented into four regions as previously described [79]. In detail, region I ($T \leq 230$ K) includes the simulation results that give values for τ_c that are above the tumbling detection criterion which is indicated by the horizontal dashed line at $\log\tau_c = -7.0$; region II ($230 < T < 235$ K) corresponds to two populations of spins that identify with either fast-tumbling ($\tau_c \approx 10^{-11}$ s) or rigid conditions ($\tau_c \approx 10^{-7}$ s). Region III ($235 \leq T \leq 255$ K) includes tumbling populations of slow and fast motions that present decreasing τ_c values with increase in T. The boundary between regions II and III ($T =$ 235 K) marks a transition in the normalized weights of the two populations with a shift from the fast tumbling to slow tumbling. The normalized weights maintain over region III a relatively constant behavior with a mean $W_f = 0.44 \pm 0.05$ and $W_s = 0.56 \pm 0.05$. The fast and slow populations transition again at the boundary between regions III and IV ($T = 255$ K), with an abrupt increase in W_f and abrupt decrease in W_s in region IV ($T > 255$ K).

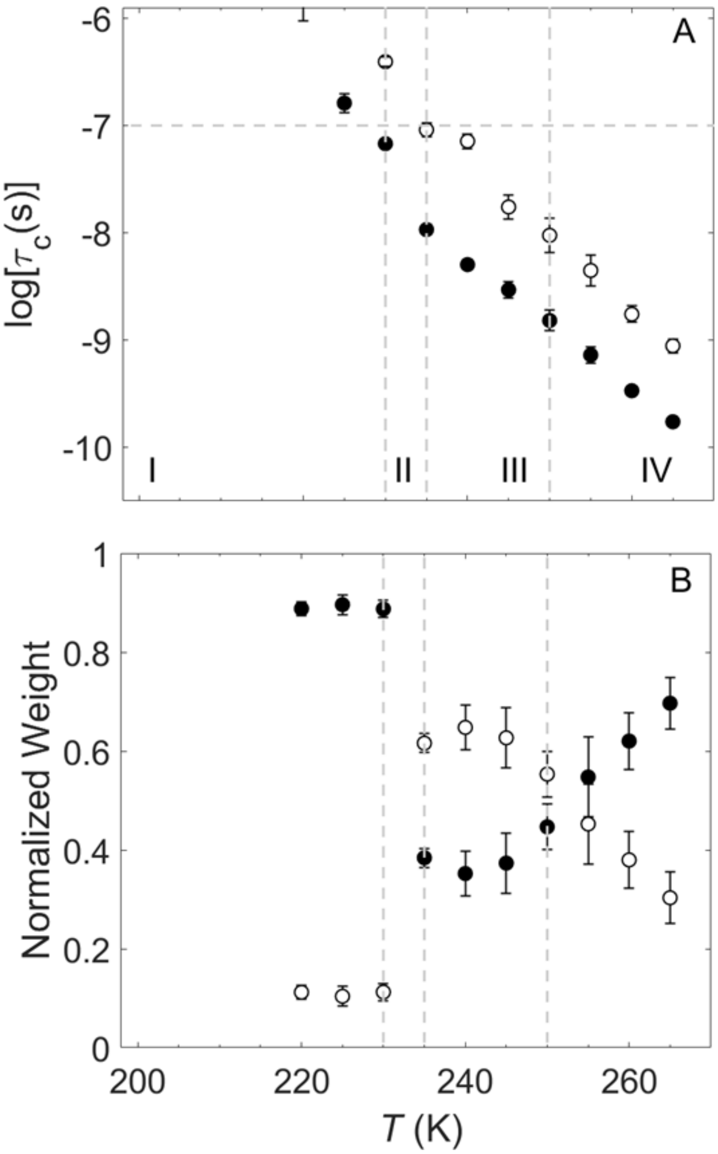

Figure 2.2. Temperature dependence of the rotational correlation time (A) and normalized mobility component weights (B) of TEMPOL in the presence of EAL and 10 mM 2-aminopropanol with 0 % v/v DMSO added. The slow and fast components are represented by open and solid circles. The error bars are the standard deviations for three separate measurements. The TEMPOL tumbling motion upper limit for detection by X-band CW-EPR is represented by the horizontal line at log τ_c = -7.0. The vertical lines represent the regions described previously. [79]

2.3.4. TEMPOL rotational correlation times and normalized weights. Temperature dependence in frozen aqueous solution with EAL and 2-aminopropanol in the presence of 2 % v/v DMSO

The TEMPOL mobility in frozen aqueous solution with EAL and 2-aminopropanol in the presence of 2 % v/v DMSO is characterized by a two-component behavior for the entire temperature region as shown in Figure 2.3. Similar to the 0 % v/v DMSO condition, the four regions of the tumbling motion are observed, with the boundary temperatures shifted to lower T values by 25 K relative to the 0 % v/v DMSO condition: region I lies below $T \leq 205$ K; region II is defined by $205 < T < 210$ K; region III is within the boundaries defined by $210 \leq T \leq 250$ K; and region IV is found above 250 K. The T-dependence of the normalized weights show a constant evolution in the slow and fast populations in region III with mean values $W_s = 0.29$ and $W_f = 0.71$ (±0.02). Region IV is characterized by a transition in the normalized weights for the slow and fast populations with a fast increase in W_f to ~ 0.8 while W_s decrease fast to ~ 0.2.

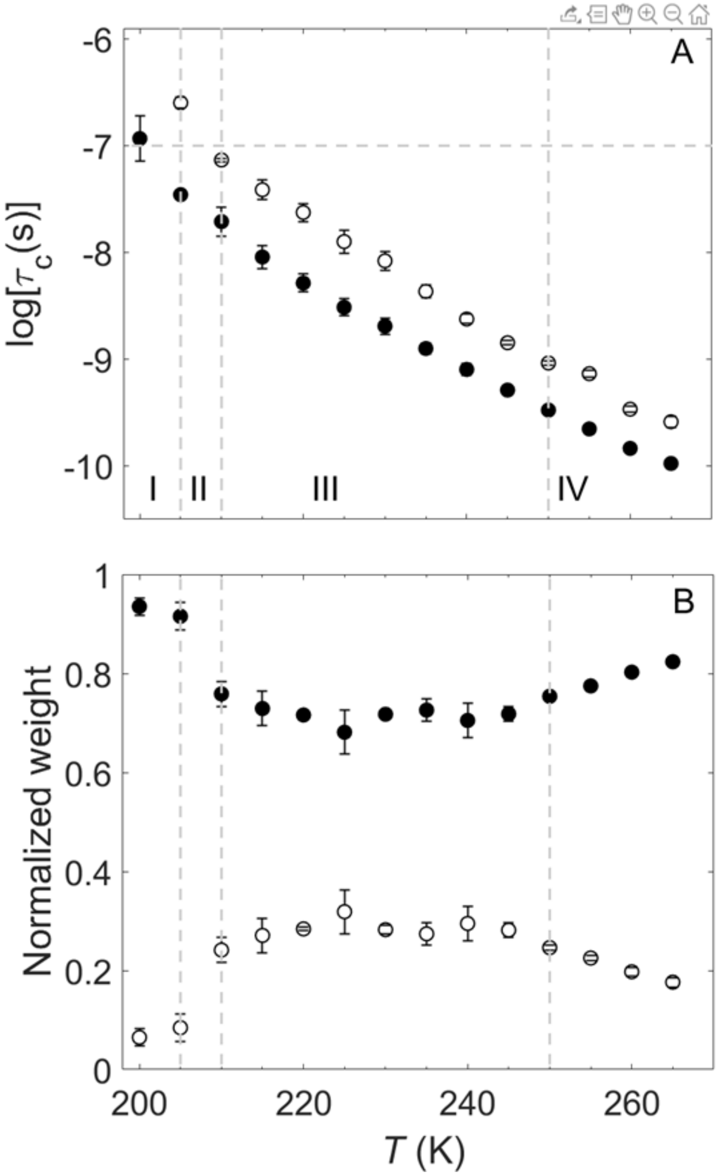

Figure 2.3. Temperature dependence of the rotational correlation time (A) and normalized mobility component weights (B) of TEMPOL in the presence of EAL and 10 mM 2-aminopropanol with 2 % v/v DMSO added. The slow and fast components are represented by open and solid circles. The error bars are the standard deviations for three separate measurements. The TEMPOL tumbling motion upper limit for X-band CW-EPR is represented by the horizontal line at log τ_c= -7.0. The vertical lines represent the regions described previously. [79]

2.4. Discussion

2.4.1. 10 mM 2-aminopropanol is creates a mesodomain around EAL at cryogenic temperatures

Similar to previous reports, the results for EAL in the presence of 10 mM 2-aminopropanol and in the absence of DMSO identify two mobility components for the spin probe.[78, 79] The EPR spectra report information about the two mobility components such as their relative proportions and associated rotational correlation times which correspond to two coexisting solvent phases: a PAD which resides at the surface of the enzyme characterized by the slow component, and a mesodomain created by the cosolvents like DMSO or the substrates aminoethanol and 2-aminopropanol characterized by the fast component.[79] In the present case for TEMPOL with EAL and 10 mM 2-aminopropanol, the T-dependence of the τ_c and W of the two components suggests that the substrate 2-aminopropanol creates a mesodomain around EAL at low T values. At T<230 K in region I, the two components describe rigid phases with correlation times that lie above the motional detection limit. The transition in region II is marked by the T value of 230 K when the local fluidization enables the detectability of the fast, dominant component which represents the population of TEMPOL that is present in the mesodomain. This component comprises ~90 % with the remaining ~10 % being trapped in the PAD. The transition to region III is concluded at 235 K where the W_s and W_f undergo a flip in dominance indicated by the relatively large drop in W_f with compensating increase in W_s. In the absence of a substrate and at different % v/v DMSO a similar type of transition was described previously[78] as the order-disorder transition (ODT) that occurs in the PAD upon T increase. Over 20 K, both components in region III are described by detectable decreases in $\tau_{c,s}$ and $\tau_{c,f}$ and, relatively constant values for W_s and W_f (W_s:W_f is ~0.6:0.4). This behavior is explained by the ODT in the PAD phase upon T increase which leads to partitioning of TEMPOL into PAD. Similar to previous results, at 250 K the ice wall starts melting and the mesodomain volume expands with increase in T, exceeding the volume of the PAD. This is suggested by the increase in TEMPOL population in the mesodomain phase with compensating decrease in the PAD while the $\tau_{c,s}$ and $\tau_{c,f}$ continue to decrease.

2.4.2. Addition of 2 % v/v DMSO to the 10 mM 2-aminopropanol increases the mesodomain volume

The presence of 2 % v/v DMSO in the sample of TEMPOL with EAL and 2-aminopropanol increases the volume of the mesodomain around EAL, shifting the ODT temperature (T_{ODT}) to lower values as demonstrated previously.[78, 79] The reported T dependence of the τ_c and W for the fast and slow components detected for TEMPOL spin probe in solution of EAL in the presence of cosolvents 10 mM 2-aminopropanol and 2 % v/v added DMSO follow the same behavior as the samples with only DMSO present as cosolvent. In the presence of substrate and DMSO, the transition from region I to region II at 205 K is shifted up by 10 K when compared to DMSO only and down by 25 K when compared to substrate only, where the mobility of the fast phase becomes detectable with a high population of TEMPOL in the mesodomain (W_s:W_f is ~0.1:0.9). The T transition from region II to III (T_{ODT}) for 2 % v/v DMSO condition has been reported at 205 K. With the addition of only 10 mM 2-aminopropanol the transition is shifted by 5 K to 210 K. Relative to the 10 mM 2-aminopropanol only the T_{ODT} value is shifted down by 25 K. This transition marks a change in the PAD fluidity where the spin probe population becomes detectable and increases with compensating decrease in the mesodomain spin probe population (a ratio W_s:W_f of 0.29:0.71). The large volume of mesodomain formed by 2 % v/v DMSO recruits a large TEMPOL population.

At the T_{ODT}, there is a decrease from about 80 % to 65 % in the TEMPOL that partitions into the mesodomain with T decrease when 2 % v/v DMSO is added, while samples with only 2 % v/v DMSO or 100 mM 2-aminoethanol substrate have a migration of spin probe of about 70 % and 58 % respectively. At T> 210 K, above the boundary of ODT in the region III, the $\tau_{c,s}$ and $\tau_{c,f}$ decrease while W_s and W_f remain constant. The T value that marks the ice wall melting and beginning of expansion in the mesodomain volume is maintained at 250 K where TEMPOL concentration in the mesodomain is increasing with compensating decrease in the PAD.

The Arrhenius dependencies of the rotational correlation times for TEMPOL in the PAD and mesodomain for EAL, 2-aminopropanol and 0 % and 2 % v/v DMSO quantify the composition and dynamical properties of the two phases. The Arrhenius equation:

$$\log(\tau_c) = \log(\tau_{c,0}) - \frac{E_a}{2.3RT} \tag{2. 1}$$

describes the properties of the system through two parameters, the activation energy barrier to rotational motions (E_a) and the correlation time at the high T limit ($\tau_{c,0}$), obtained from the slope and intercept of the linear fits.(Table 2.1.) The Arrhenius relationship observed before, where the slope for PAD is higher than for the corresponding slope for mesodomain, is maintained here. The linearity of log(τ_c) versus 1/T is consistent with the T-dependence described previously [78] which indicates constant solution properties (uniform composition) over the indicated T range in both solvent components, PAD and mesodomain. Additionally, the T-dependence for the two phases described for 10 mM 2-aminopropanol cosolvent represent new results. The high values for the E_a for 10 mM 2-aminopropanol condition are in agreement with the very small mesodomain that is inferred, suggesting strong ice-boundary confinement effects on the PAD solvent dynamics not observed previously for low % v/v DMSO. Addition of 2 % v/v DMSO to the 10 mM 2-aminopropanol considerably reduces these effects. This is indicated by the decrease in E_a and increase in log($\tau_{c,0}$) parameters with addition of 2 % v/v DMSO, in agreement with previous reports [79] that propose vanishing of the ice-boundary confinement effects on the PAD by increase in mesodomain volume. This confirms the tunability of the solvent dynamics of the PAD in the presence of 2-aminopropanol and added DMSO. Moreover, it was observed that for EAL and 10 mM 2-aminopropanol combined with 2 % v/v DMSO, the mesodomain and PAD present higher values for E_a and log($\tau_{c,0}$) parameters than for the case where EAL is in only 2 % v/v DMSO condition ($\Delta E_a \approx 2$ kcal/mole and $\Delta\log(\tau_c) = -2$ s.

Table 2.1. Arrhenius parameters obtained from the *T*-dependence of the rotational correlation times for TEMPOL tumbling motion in EAL and 10 mM 2-aminopropanol system with or without DMSO at *T* values where τ_c is detectable ($<10^{-7}$). R^2 for the linear fits are 0.9931 and 0.9944 for PAD, and 0.9985 and 0.9994 for mesodomain for 0 % DMSO and 2 % DMSO, respectively.

DMSO (% v/v)	***E*** **E_a (kcal/mol)**		**-log[$\tau_{c,0}$ (s)]**	
	PAD	mesodomain	PAD	mesodomain
0	19.71 ± 1.5	18.48 ± 0.7	25.31 ± 1.3	25.02 ± 0.6
2	11.72 ± 0.4	10.17 ± 0.1	19.28 ± 0.4	18.38 ± 0.1

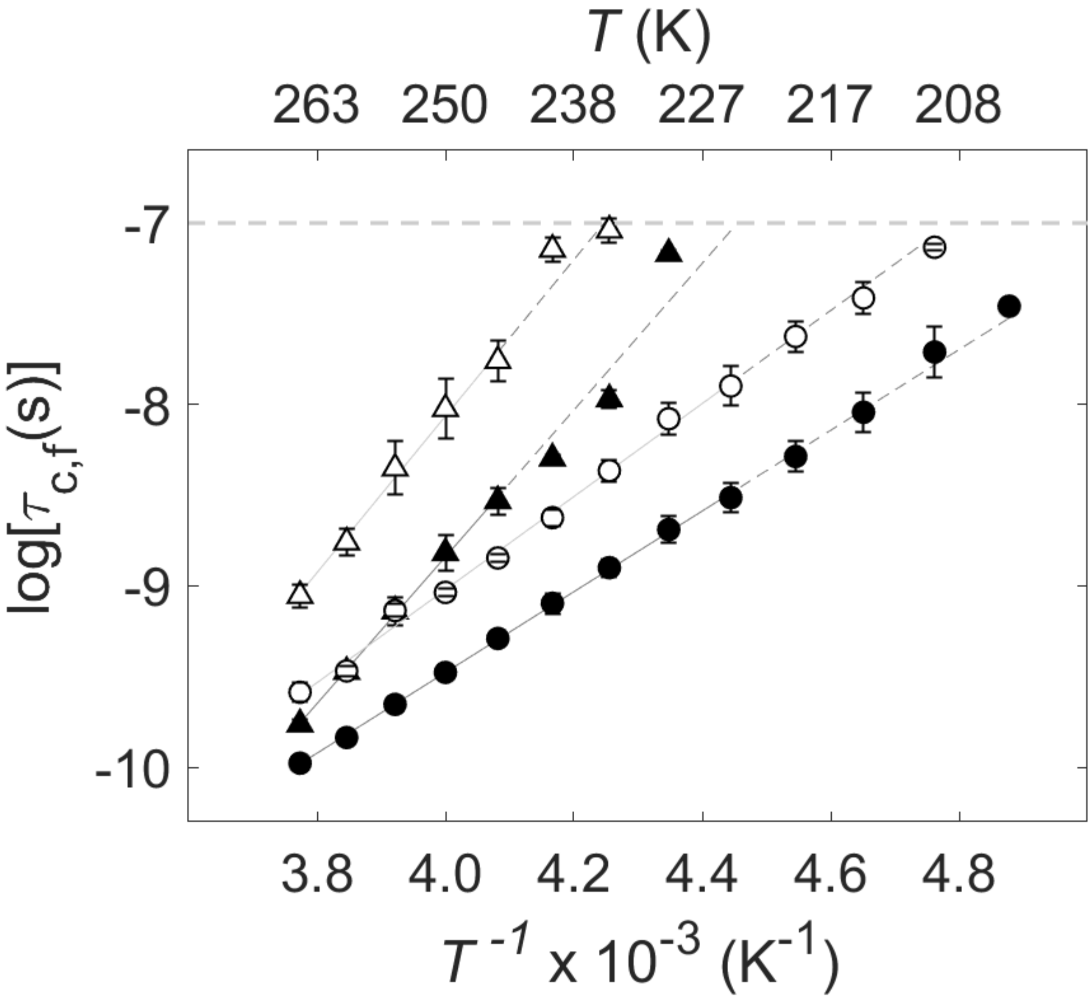

Figure 2.4. Arrhenius plot for rotational correlation times that characterize the TEMPOL in solution of EAL, 10 mM 2-aminopropanol and the different DMSO %: 0 % (triangles) and 2 % (circles) v/v added DMSO. The slow and fast tumbling components are shown in open and filled markers. Overlaid are the linear fits with extrapolation (dotted line). The error bars are the standard deviations for three separate measurements. The TEMPOL tumbling motion upper limit for X-band CW-EPR is represented by the horizontal line at log τ_c= -7.0.

2.4.3. Estimations for the relative dimensions of the mesodomain

The PAD has been characterized to be independent on the mesodomain and to have a volume that corresponds to a shell that is roughly two water molecules thick ($t_{PAD} \approx 6$ Å), $V_{\mathrm{PAD}} \approx 3$ µl.[79] These values correspond for the entire 300 µl volume of sample and a total concentration of EAL oligomer of 20 µM which translates to 4.0×10^{15} EAL molecules, each EAL oligomer being characterized by a surface area of 1.3×10^{5} Å^{2}.[62] However, for DMSO the mesodomain was proven to depend on the volume of the cosolvent and a proportionality constant, γ_{meso}, that is related to the maximum freeze concentration [126] of the cosolvent. Considering that:

$$V_{meso} = \gamma_{meso} \times V_{cosolvent} \qquad (2.\,2)$$

and that γ_{meso} was approximated to 1/0.65, the V_{meso} for 2 % v/v DMSO was calculated to be 9.2 µl with a thickness of 18 Å. The 10 mM 2-aminopropanol corresponds to 0.08 % v/v cosolvent ($V_{cosolvent}$ of 0.23 µl) which is 6.5 times lower than the lowest DMSO concentration (0.5 % v/v) studied previously.[79] Even if the lowest concentration of DMSO cosolvent that would form a mesodomain was not experimentally determined, the results indicate that 10 mM 2-aminopropanol is enough to form this interstitial phase. In order to determine the characteristic V_{meso} formed by the substrate the maximum freezing concentration of aqueous 2-aminopropanol solution is needed.

Previous work has investigated the thermal properties and glass formation of amino-alcohol compounds for developing methods for long-term organ preservation.[127, 128] For different cooling rates the solutes presented crystallization tendencies from which a volume w/w for solute to water is extracted for the crystals to be suppressed. For both aminoethanol and 2-aminopropanol, the maximum freeze concentration for glass formation is about 40 % w/w which represents 40 % v/v considering that their density is close to 1g/ml. Under these considerations the V_{meso} in the presence of 10 mM 2-aminopropanol is expected to be 0.58 µl, with a t_{meso} of 1.1 Å considering that γ_{meso} = 1/0.4 . Thus, volume and thickness of the mesodomain formed by 2-aminopropanol are five times smaller than the PAD if we consider that the volume of mesodomain covers a planar surface area equal to the solvent accessible area of 20 μM EAL. Because TEMPOL was reported to have a diameter of 7 A, at low *T*, below 230 K, the mesodomain is proposed to be not well defined in a uniform concentric disk around EAL. Small volumes of mesodomain isolate TEMPOL from the ice-crystallite region in the protein proximity such that, at increased *T*, when PAD goes through ODT, the TEMPOL from these local mesodomain formations partition into the PAD. As *T* increases the mesodomain volume expands forming the uniform concentric disk around EAL and recruiting a larger TEMPOL population.

2.5. Conclusions

The results herein indicate that 10 mM 2-aminopropanol in the presence or absence of 2 % v/v DMSO create two phases around EAL with solvent dynamics coupling, and confirm the results reported previously for EAL in solution of different % v/v DMSO and no substrate added.[78, 79] Therefore, not only DMSO but also the substrates aminoethanol and 2-aminopropanol reported for the B_{12}-dependent EAL create a mesodomain around the protein. The solvent dynamics of the mesodomain and PAD can be manipulated by changing the volume of the mesodomain by adding different % v/v cosolvent DMSO and this is quantified by the *T* region of ODT in PAD. Thus, an increased PAD solvent dynamics was detected upon addition of 2 % v/v DMSO to the 10 mM 2-aminopropanol which induces a decrease in the T_{ODT} region by 25 K. Similar to 100 mM aminoethanol which has a T_{ODT} at 225 K, the 10 mM 2-aminopropanol also presents an order-to disorder transition region which is 10 K higher than T_{ODT} for aminoethanol. These results advance the understanding of the reaction kinetics of EAL by further investigating the solvent-protein coupling effects on the chemical reaction steps induced by manipulating solvent dynamics.

Chapter III

Mechanism of 2-aminopropanol substrate radical rearrangement catalysis in B_{12}-dependent EAL

3.1. Introduction

The adenosylcobalamin (coenzyme B_{12}) –dependent ethanolamine ammonia-lyase (EAL; cobalamin (vitamin B_{12})-dependent enzyme superfamily)[129, 130] is the signature enzyme that starts the ethanolamine catabolism in the ethanolamine utilization (Eut) metabolic pathway [13] associated with microbiome homeostasis. [131] The pathway is suggested to be highly used by pathogens like enterohemorrhagic and enteropathogenic *Escherichia coli* and *Salmonella enterica* to process ethanolamine as sole nutrient source and induce disease conditions in the human gut.[23, 116, 117] Native reactions in EAL proceed over a wide low-temperature (T) range of 190 – 250 K, which allows kinetic resolution of intermediate and individual steps in the core catalytic sequence of aminoethanol [64, 68, 76, 107] and (S)-2-aminopropanol [77] conversion to the corresponding aldehyde and ammonia, by using time-resolved, full-spectrum electron paramagnetic resonance (EPR) spectroscopy.[61] EAL also represents a model enzyme for understanding fundamental physical features of the contributions of dynamics to catalysis. Recent spin probe EPR experiments under the same conditions show that the persistence of the native reaction properties deep into the cryo-regime (rate constants adhere to the same Arrhenius relation from physiological, ~295 K T values to at least 220 K) is promoted by the formation of a fluid mesodomain around EAL in the frozen aqueous solution, which maintains the protein hydration layer.[78] The cosolvent-tunable dynamics provide a powerful probe of solvent-protein dynamical coupling to the EAL reactions with single-step resolution. Here, we address the role of solvent dynamics in the native, productive substrate radical reaction and a well-defined, non-native destructive pathway of substrate radical reaction in EAL from *S. enterica serovar typhimurium.* The solvent dynamic results reported in Chapter 2 are used to reveal and characterize the solvent-protein-catalysis dynamical coupling.

The cob(II)alamin (Cbl(II))-substrate radical pair state accumulates during steady-state turnover at room *T*, and is cryotrapped as the only paramagnetic state.[61] Reactions are initiated by subsequent *T*-step up to *T* values in the wide range of 190 – 250 K. The substrate radical decay reaction at cryogenic *T* values occurs from two substrate radical microstates, denoted as $\mathbf{S_1^{\bullet}}$ and $\mathbf{S_2^{\bullet}}$, for 2-aminopropanol from 220-250 K [77] and for aminoethanol at T<220 K [76]. $\mathbf{S_1^{\bullet}}$ and $\mathbf{S_2^{\bullet}}$ are proposed to represent two protein configurational states that are sequential intermediates on the native pathway of the radical rearrangement to the product radical state ($\mathbf{P^{\bullet}}$) and subsequent hydrogen transfer-mediated formation of the diamagnetic product state (**PH**).[68] $\mathbf{S_1^{\bullet}}$ is poised to capture the nascent substrate radical formed by the initiating radical pair separation event, and $\mathbf{S_2^{\bullet}}$ is the enabling state for radical rearrangement. For aminoethanol substrate, when the configurational interconversion of $\mathbf{S_1^{\bullet}}$ and $\mathbf{S_2^{\bullet}}$ is blocked at *T*<220 K, reaction from $\mathbf{S_1^{\bullet}}$ proceeds with slower rate constants but with radical rearrangement and hydrogen transfer steps that lead to diamagnetic products. A rapid $\mathbf{S_1^{\bullet}}$ and $\mathbf{S_2^{\bullet}}$ transition holds at *T*≥220 K, and reaction occurs from a proposed macroscopic $\mathbf{S^{\bullet}}$ state with monoexponential kinetics.[76] In contrast, 2-aminopropanol displays reaction from both $\mathbf{S_1^{\bullet}}$ and $\mathbf{S_2^{\bullet}}$ at low *T* values, and reaction from $\mathbf{S_1^{\bullet}}$ leads to a non-native uncoupled Cbl(II) and free radical species.[77] This pathway shows that the enzyme misfires when the specific, reaction-guiding protein configuration (i.e., $\mathbf{S_2^{\bullet}}$) is not present. The cryo-*T* reaction of 2-aminopropanol occurs with observed rate constants that are approximately 10^2-fold slower than for aminoethanol. The lower rate may arise from imprecise positioning/steric restrictions on the rearrangement process of 2-aminopropanol, owing to the bulk of the 2-methyl moiety. The catalytic machinery of EAL is exceptionally sensitive to substrate structure – only the S-isomer of 2-amino-1-propanol, of the four 1,2-heteroatom aminopropanols was reported to undergo direct turnover. Therefore, 2-aminopropanol provides a stringent test of specificity of the protein guidance mechanism, and specifically, the role of fluctuations/dynamics. This structural effect might also lead to a desynchronization of the reaction and protein dynamics. Further, the influence of protein and coupled solvent dynamics on the native ($\mathbf{S_2^\bullet}$) and non-native ($\mathbf{S_1^\bullet}$) reaction pathways can be compared. A comparable influence would suggest that reaction dynamics are generic with respect to driving the reactions.

The fluidity of the mesodomain phase that surrounds EAL in frozen aqueous solution can be tuned by using cosolvents and temperature.[79] The substrates themselves act as cosolvents. In the aminoethanol reaction system, the bifurcation of the reaction kinetics is associated with an order-disorder transition (ODT) in the protein associated domain (PAD, also known as hydration layer) at *T*~220 K. This *T* value of the ODT is established by the aminoethanol substrate, present at 10^{-1} M prior to sample freezing. In the previous chapter it was determine the *T*-value of the PAD ODT for the 2-aminopropanol concentrations used here in kinetics measurements (10^{-2} M), and the ODT was tuned to lower *T*-values by using added dimethylsulfoxide (DMSO) cosolvent. The influence of these variations in solvent conditions on the kinetics of the resolved protein configurational change and the 2-aminopropanol substrate radical rearrangement reaction steps are used to address the coupling of solvent, protein, and reaction dynamics.

3.2. Materials and Methods

3.2.1. Protein and EPR sample preparation

The EAL enzyme expression, isolation and purification was done as described in Chapter II. The procedure for samples with cryotrapped Cbl(II)-substrate radical pair has been detailed in previous work. [61] Similarly, the samples for EPR spectroscopy were aerobically prepared in small vials, on ice, under dim red light to ensure no photochemical degradation of the coenzyme

B_{12} (adenosylcobalamin, AdoCbl) cofactor.[41, 65] All reactions were prepared in 10 mM potassium phosphate buffer (pH 7.5). When present, DMSO was added to 2 % and 4 % v/v relative to the sample final volume size of 300 µL. The purified enzyme, EAL, was added to a final concentration of 10 mg/mol (20 µM or 120 µM active sites) together with a four-fold molar excess of AdoCbl per active site. After each component addition to the buffer solution with DMSO (if present) the composition was mixed for 4 s by using a vortex mixer. The substrate (S)-2-aminopropanol was added to the reaction mixture to a final concentration of 10 mM during the final 4 s vortexing, then immediately loaded into 4 mm outer diameter EPR tubes and rapidly submerged in liquid nitrogen isopentane pre-cooled to 140 K. The time interval for the process from adding the substrate to freezing took in average about 18 s ±3s. The freezing method has a characteristic cooling rate of 10 K/s. [61] Samples were stored in liquid nitrogen until measurements.

All chemicals and reagents used are commercially available and they did not need further purification. DMSO (purity, ≥99.9 %) was purchased from EMD Chemical, the deionized water (resistivity, 18.2 MΩ·cm) was obtained from a Nanopure system from Siemens, (S)-2-aminopropanol and coenzyme B_{12} are products of Sigma-Aldrich, and the EPR tubes were purchased from Wilmad-LabGlass.

3.2.2. Continuous Wave-EPR spectroscopy

The CW-EPR spectra were collected by using a Bruker E500 ElexSys EPR spectrometer equipped with a Bruker ER4122 SHQE X-band cavity resonator. The temperature was controlled by using a Bruker ER4131VT temperature controller and cooling system that consists of a nitrogen gas flow through a coil immersed in ethanol dry ice bath at ~ 200 K, contained in a 4 L dewar. The cooling procedure maintains the desired temperature stable for longer times, requiring addition of dry ice to the bath at longer time intervals (40 min to 1 h) when compared to liquid nitrogen bath (20 min). For shorter time experiments, at 120 K the cooling system consisted of a nitrogen gas flow through a coil immersed in liquid nitrogen. Across the EPR sample cavity the temperature stability is within 0.5 K. [61] For each decay experiment, the temperature value readout on the controller was calibrated by using a 19180 4-wire RTD probe (± 0.3 K accuracy) and an ITC503 unit from Oxford Instruments as previously described. [61]

3.2.3. Time-resolved full-spectrum EPR spectroscopy of substrate radical decay at cryogenic temperatures

Measurements in the region 220-240 K. The experimental protocol for time-resolved full-spectrum EPR spectroscopy of Cbl(II) - substrate radical pair at low cryogenic temperatures was described in previous work.[61, 77, 124] For the 2-aminopropanol radical decay, the following acquisition parameters were used: 9.45 GHz microwave frequency; 2.0 mW microwave power; 10 Gauss magnetic field modulation; 100 kHz modulation frequency; 2600-4000 Gauss sweep width with central field at 3300 Gauss. A set of three different EPR samples prepared from different EAL protein purification preparations were measured at the selected temperature value within the range 220-240 K (10 K increments). After calibrating the temperature in the cavity resonator at the desired decay *T*, a dummy sample which lacks the substrate was measured (32-64 averaged spectra). For the different % v/v DMSO, either the corresponding dummy or an identical previously decayed sample were used to pre-tune the microwave bridge. This step reduced the time interval (dead time) from insertion in the cavity of the cryotrapped radical pair state sample to start of the acquisition to 1-3 minutes, by facilitating a faster tuning process. For the entire duration of the decay, which ranged between 2.5×10^4 to 9×10^4 s for the different temperatures, the EPR spectra were continuously measured with a sweep time of 41.9 s and a time constant of 10.2 ms (conversion time, 81.9 ms) for 512 points/scan and a delay time between scans of 10-100 ms.

Measurements at 210 K. Measurements for the decay of Cbl(II)-2-aminopropanol substrate radical pair at the temperature of 210 K were performed over a time length of ~80 × 10^4 s which is equivalent to ~ 9 days. Similar EPR parameter to the T region 220-240 K were used. The decay procedure included a temperature controller -100^o C ISIS Dry Block Calibrator (Isotech, model 525) with sample insert type B. The controller is designed to maintain a constant temperature in the range -100 to 40 ^{o}C with high stability within 0.04 ^{o}C. The instrument was previously calibrated using a thermocouple thermometer and type K thermocouple probe. For accurate calibration and to mimic the temperature at the probe, an assemble containing the probe placed in a 4 mm diameter EPR tube filled with 300 µl deionized water was frozen in isopentane cooled by liquid nitrogen at 140 K. The calibration step included testing the accuracy of the probe in water at room temperature, ice and liquid nitrogen, and calibrating the temperature at the sample holder inserts of the controller. The temperature controller was set at the corresponding 210 K (or -63.15 ^{o}C) calibrated T of 61.9 ^{o}C. For a week the controller was keeping the temperature set constant with no variations recorded (T stability determined was within 0.3 ^{o}C). Similarly, three samples were measured at this T. First, they were each measured continuously for ~18 h using the same parameters and procedures as for the other T, then stored in liquid nitrogen. In addition, for the 210 K experiments the time span from when the experiment was stopped until the sample was placed in liquid nitrogen was recorded and added to the decay time scale. After this decay step, all samples were taken out of the liquid nitrogen and incubated in the temperature controller (T_{set} = -61.9 ^{o}C) in the large 13 mm diameter insert where they continued to decay for the rest of 8.5 days. After each 3-6 h the samples were measured in the Bruker E500 ElexSys EPR spectrometer at *T* of 120 K with an average of 4-8 scans. At 120 K, the decay of the cryotrapped radical pair is negligible when compared to the time scale of the experiments. Samples were kept in liquid nitrogen when they were out from the temperature controller and EPR cavity. The time of decay was stopped every time the samples were out for EPR measurement and started each time the samples were placed back into the temperature controller for incubation. A dummy sample which was lacking the substrate was measured each time with the samples (average of 4-8 scans), being taken through the same steps, for background signal correction. In addition, a control sample and a dummy sample identical with the experimental ones were kept in liquid nitrogen for the entire experiment and measured each time at 120 K for signal calibration. At all times during the experiment the position of all samples was maintained the same by using the label on the EPR tube as a reference point.

3.2.4. Steady-State Kinetic Measurements

Room temperature (RT) kinetic measurements were performed for samples containing 20 µM purified EAL (120 µM active sites), 480 µM AdoCbl and 10 mM (S)-2-aminopropanol in 10 mM potassium phosphate buffer (pH 7.5). Five samples were prepared as specified above. After reaction mixture the samples were loaded into the 4 mm diameter EPR tubes. Each of the samples were incubated for a set time interval in isopentane at RT (~ 288 K) to react, then quickly emerged in liquid nitrogen isopentane pre-cooled to 140 K, for freezing and substrate radical trapping. The five samples corresponded to five time intervals of decay: 1, 5, 10, 20 or 30 min. A time ‘0 s’ sample was prepared by rapidly freezing after loading into the EPR tube. All samples were measured at 120 K with a 4-8 averaged spectra. The EPR measurement conditions and parameters were the same as for low temperatures decay experiments.

3.2.5. Transient kinetics analysis

The continuous EPR spectra collection exhibit over time a decay of the Cbl(II)-substrate radical pair feature at high field around $g \approx 2.0$. The time-dependence of the amplitude of this feature relative to the baseline from the EPR spectrum with background subtracted was fitted to a biexponential function (n = 2) that has the expression:

$$\frac{A(t)}{A(0)} = \sum_{i=1}^{n} A_i e^{-k_i t} \tag{3. 1}$$

where $\frac{A(t)}{A(0)}$ is the normalized observed EPR amplitude, A_i is the normalized component amplitude associated to the first order rate constant k_i. The data processing and fitting were developed in Matlab.

3.2.6. Temperature dependence of observed rate constants

The first-order rate constants obtained from fitting the normalized observed amplitudes have a temperature dependence which can be described by the Arrhenius (Equation 3.2) or Eyring (Equation 3.3) expression of the reaction-rate theory:

$$k(T) = Ae^{-\frac{E_a}{RT}} \tag{3. 2}$$

$$k(T) = \frac{k_B T}{h} e^{-\frac{\Delta H^{\ddagger}}{RT}} e^{\frac{\Delta S^{\ddagger}}{R}} \tag{3. 3}$$

where A is the Arrhenius prefactor with units of s^{-1}, E_a is the activation energy, R is the universal gas constant, k_B and h are the Boltzmann and Plank constants, and $\Delta H^{\ddagger}$ and $\Delta S^{\ddagger}$ are the activation enthalpy and entropy which give a free energy of $\Delta G^{\ddagger} = \Delta H^{\ddagger} - T\Delta S^{\ddagger}$. The linear dependence of the logarithmic plots of the rate constants as a function of 1/*T* gives information on the activation energy, enthalpy, entropy and free energy of activation.

3.2.7. Numerical simulations and fitting of the minimum kinetic model

The experimental results were simulated and fitted to a four-state ($\mathbf{S_1^\bullet}$, $\mathbf{S_2^\bullet}$, $\mathbf{X^\bullet}$ and **P**), three-step (k_1, k_2, k_3, k_4) microscopic kinetic model. The set of differential equations that describe the model was solved explicitly in Matlab using *dsolve* function under the initial conditions, $[\mathbf{S_1^\bullet}]_0=a_1$, $[\mathbf{S_2^\bullet}]_0=a_2=1-a_1$, $[\mathbf{X^\bullet}]_0=0$ and $[\mathbf{P}]_0=0$, where $[]_0$ represent the concentration of the species in the respective state at time 0. The set of ordinary differential equations that describe the time dependence of the states is:

$$\frac{dS_1}{dt} = -k_1S_1 - k_3S_1 + k_4S_2 \tag{3. 4}$$

$$\frac{dS_2}{dt} = -k_2S_2 - k_4S_2 + k_3S_1 \tag{3. 5}$$

$$\frac{dX}{dt} = k_1S_1 \tag{3. 6}$$

$$\frac{dP}{dt} = k_2S_2 \tag{3. 7}$$

The set of solutions that describe the time evolution of each $\mathbf{S_1^\bullet}+\mathbf{S_2^\bullet}= \mathbf{S^\bullet}$ decay and growth of $\mathbf{X^\bullet}$ and **P** were separately fit to the corresponding experimental data by using the *lsqcurvefit* function. The fitting function uses the least squares regression analysis equation

$$\underset{x}{min} \|F(x, xdata) - ydata\|_2^2 = \sum_i (F(x, xdata_i) - ydata_i)^2 \tag{3. 8}$$

Where the *xdata* and *ydata* are the time and experimental amplitude matrices of the corresponding species ($\mathbf{S^\bullet}$, $\mathbf{X^\bullet}$ and **P**), and *x* are the parameters that describe the model, the microscopic rate constants (k_1, k_2, k_3, k_4) and [$\mathbf{S_1}^{\bullet}$]$_0$. A global search of the unique set of parameters that simultaneously fit all three solutions to their respective data set was performed using the optimization algorithm known as *patternsearch*. *Paternsearch* is a global optimization routine that searches for the minimum of the objective function based on an adaptive mesh. Thus, seeding the starting points in the optimization procedure with the parameter sets obtained from the individual fits, increased the likelihood that a starting parameter set occur near a global minimum.

3.3. Results

3.3.1. Time-resolved, full-spectrum EPR of the cryotrapped 2-aminopropanol substrate radical intermediate in EAL

The EPR spectrum at 120 K for the Cbl(II) – substrate radical pair generated in EAL following cryotrapping step during turnover on 2-aminopropanol is shown in Figure 3.1. The characteristic features discussed in Chapter 1 for Cbl(II)-2-aminopropanol substrate radical pair at X-band CW-EPR extends over the range of 140 mT. The line shape reveals the broadened Cbl(II) features from the dipolar interaction with the substrate radical as well as splits in the prominent peaks of the Cbl(II) at $g_{\perp}$ = 2.32 (or 290 mT) and substrate radical at $g_{\parallel}$ = 2.0 (or 335 mT). As mentioned earlier in Chapter 1 quantifications of the magnetic dipolar interaction resolved the electron-electron distance of the radical pair which was approximated to 11 Å. [58, 59] The line shape and signal amplitude at 120 K are consistent throughout all samples with and without DMSO.

In Figure 3.2 the time-dependence of the EPR signal of the Cbl(II)-substrate radical pair formed on 2-aminopropanol substrate in EAL is shown for the temperature step at 230 K. The zero-time line shape is identical to the 120 K measurement with identical features (Figure 3.2 A).

As the decay of the radical pair progresses the EPR line shape is changing exposing new features which are mentioned in previous work.[77] In brief, the Cbl(II)-substrate radical pair (Figure 3.2 B) with features described by the 120 K data has a decrease in the amplitudes of both Cbl(II) and substrate radical species while an isolated Cbl(II) feature (Figure 3.2 C) is arising in the overall signal reported by a single narrow peak at $g_{\perp}$ = 2.32 (or 290 mT) and this is accompanied by an additional narrow radical feature at $g \approx 2.0$. Both of these new growing features were resolved through spectral deconvolution methods as described further.

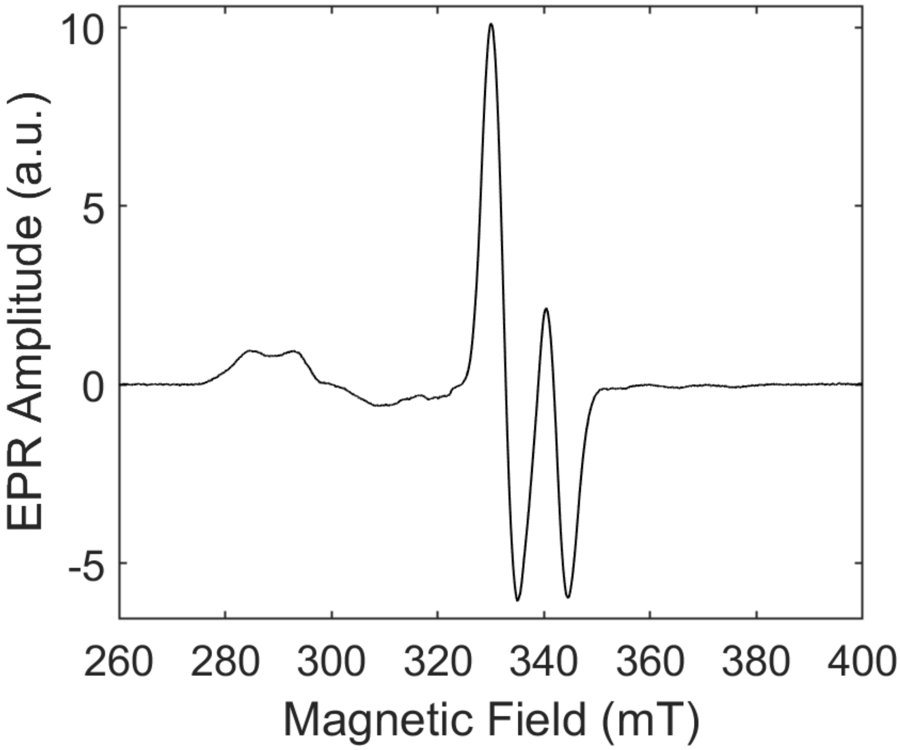

Figure 3.1. EPR spectrum of the cryoptrapped Cbl(II)-2-aminopropanol substrate radical pair in EAL. Measurement conditions:120 K; 9.45 GHz microwave frequency; 2.0 mW microwave power; 10 Gauss magnetic field modulation; 100 kHz modulation frequency; 2600-4000 Gauss sweep width; 4 averaged scans.

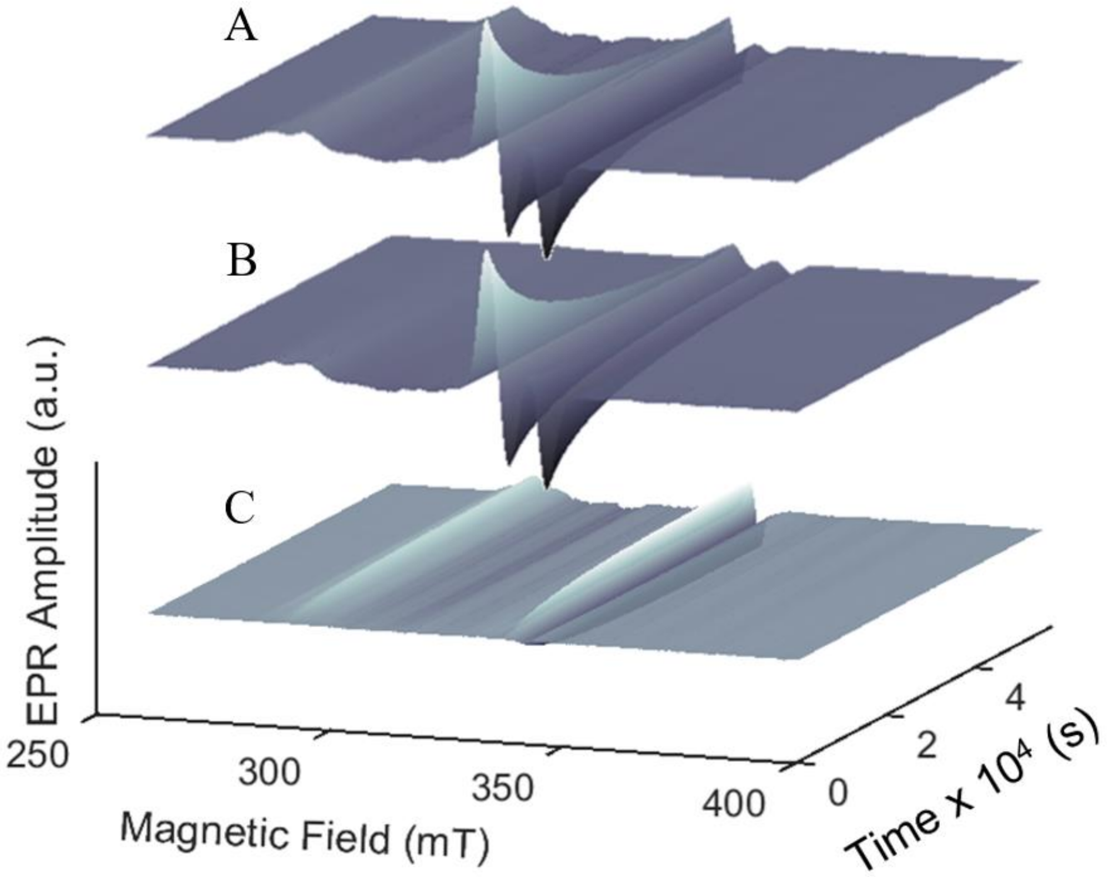

Figure 3.2. Time-resolved, full-spectrum EPR of the cryotrapped 2-aminopropanol substrate radical intermediate in EAL resolved by X-band EPR at 230 K. A. The observed time-dependence EPR signal of the radical pair. B. The deconvoluted time-dependence decay signal of the Cbl(II)-substrate radical pair. C. The deconvoluted time-dependence rise signal of the Cbl(II) radical species. Measurement conditions: 9.45 GHz microwave frequency; 2.0 mW microwave power; 10 Gauss magnetic field modulation; 100 kHz modulation frequency; 2600-4000 Gauss sweep width; 41.9 s sweep time; 10.2 ms time constant (conversion time, 81.9 ms); and 512 points/scan with a delay time between scans of 100 ms.

3.3.2. EPR spectra of the deconvoluted Cbl(II)-radical pair species

The magnetically isolated Cbl(II) feature was resolved by spectral deconvolution. The method was developed in Matlab and implemented for each time-dependence measurement over the *T* range of 210-240 K. As mentioned earlier the zero-time EPR spectrum is the characteristic signal of the Cbl(II)-substrate radical pair. Therefore, the zero-time EPR spectrum from the set of EPR spectra continuously collected during the decay was isolated and scaled to each of the remaining spectra with respect to the second trough amplitude. Further the corresponding scaled spectrum was subtracted from the subsequent spectra from the measured data set. The result of the subtraction is a time-dependence of the uncoupled Cbl(II) and radical species (Figure 3.2 C and Figure 3.3). The deconvolution reveals the temporal growing of the uncoupled Cbl(II) as the radical pair decays. In Figure 3.2 the amplitude of the uncoupled species is reported with respect to the initial total amplitude of the EPR signal as recorded and it shows an overall small magnitude. However, taken separately the growth is significant and gives important information about the system as discussed further.

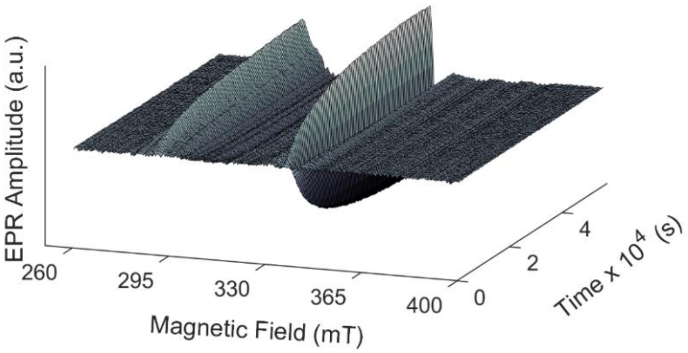

Figure 3.3. Time-dependence EPR signal of the uncoupled Cbl(II) radical species component of the Cbl(II)-substrate radical pair state in EAL when using 2-aminopropanol substrate. The signal is deconvoluted from the time series measurements at 230 K and is the same signal shown in Figure 3.2.III.

3.3.3. Quantification of the radical species contribution to the EPR spectra. Proportions of the diamagnetic product states

The zero and final time EPR spectra from the time-dependence measurement at the selected *T* value are used to determine the relative proportions of the components of the radical species that contribute to the EPR derivative signal throughout the decay. The double integration of the selected spectra was applied to obtain the area under the corresponding absorption spectra (first integration of the signal) which is known to be proportional to the amount of spins of the respective components. Because the relative proportion are of interest for this study, the exact concentrations of the spins are not necessary. The double integration was performed by using Matlab. As shown previously the broad peak at low field in the absorption line is given by the Cbl(II) while the peak at high field is from the substrate radical, with 1:1 ratio for the Cbl(II)-substrate radical pair signal at zero-time spectrum.[77] Because the coupled and uncoupled species will reside under the same absorption line (at t>0) the deconvoluted spectra are used in quantifying the uncoupled radical species existent at the final of each measurement. In Figure 3.4 it is shown the selected area under the curve (AUC) for each component of the EPR signal, Cbl(II) and substrate radical: at zero-time (A) the spectrum is given by the radical pair; and in the final scan (B) the signal convolutes the radical pair (D) with uncoupled species (C). The relative proportions of the components for each data set are obtained relative to zero-time spectrum. The values are included in Appendix C, Table C.1 as mean values from the three measurements at each *T*-step.

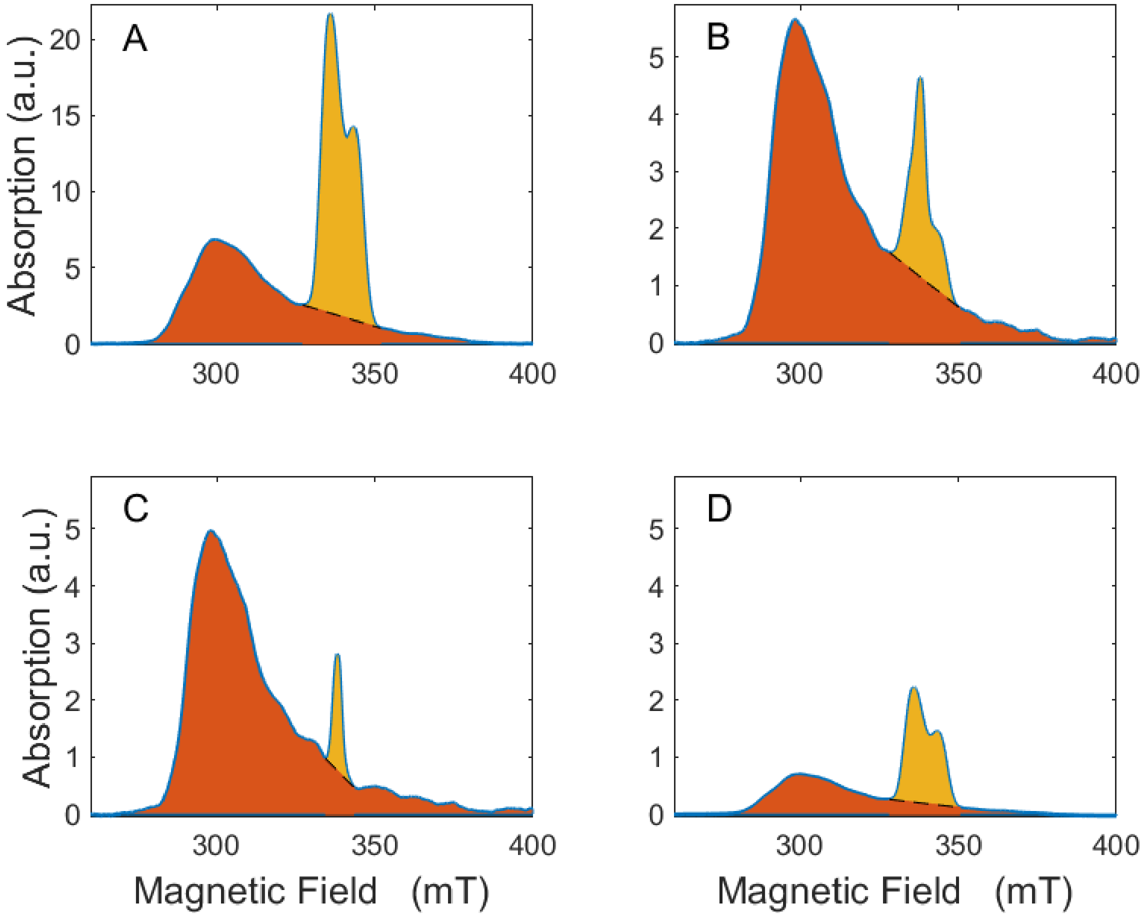

Figure 3.4. The absorption spectra of the EPR signal of the Cbl(II)-substrate radical pair measured at 230 K (blue line contours the entire absorbtion): A. The absorption of the zero-time EPR spectrum from the series of time scans, with 1:1 for Cbl(II): substrate radical from the radical pair; B. The absorption of the final EPR spectrum from the series of time scans which include coupled and uncoupled Cbl(II), substrate radical and radical species. C. The absorption of the deconvoluted Cbl(II) and radical species components from the final EPR spectrum from the series of time scans; D. The absorption of the deconvoluted Cbl(II)-substrate radical pair component from the final EPR spectrum from the series of time scans. Depicted by each area are the Cbl(II) species (orange) and the substrate radical species (yellow). The dashed black line indicates the level for the area calculation of the substrate radical species.

3.3.4. Time-dependence of the Cbl(II)-substrate radical pair decay component

3.3.4.1. Cryotrapped 2-aminopropanol substrate radical intermediate in EAL with 0 % v/v DMSO solution, measured over 210-240 K

The decay of the Cbl(II)- substrate radical pair is studied through monitoring in time the amplitude of the second trough, which is the substrate radical feature in the *g*=2 region, relative to the baseline at high field. The method for analysis was developed in Matlab and it uses the analysis approach reported in previous work.[68, 77] As observed in Figure 3.2 this feature is absent in the time-dependence uncoupled signal and, thus is associate with the radical pair and more specifically with the substrate radical. The measurements are performed to a decay level of ~ 8 % from the initial amplitude for the substrate radical of each sample in order to resolve for all components that are involved in the kinetics. Therefore, the time scales of the decays vary from ~ 2.5×10^4 s for 240 K to ~ 80×10^4 s for 210 K as it can be seen in Figure 3.6 which shows the decay of the amplitude of the radical pair for T values over the range 210-240 K. The overlaid fits presented in the figure represent the best fits of the biexponential function which gives information on the kinetics of the components that describe the process. The values of the first-order rate constants and normalized amplitudes for the two components (slow- and fast-phase observed rate constants $k_{obs,s}$ and $k_{obs,f}$, and corresponding normalized amplitudes $A_{n,s}$ and $A_{n,f}$) are reported as mean values from three measurements at each T-step, together with the statistical measure of the fitting given by the mean of the Pearson's correlation coefficient R^2 over the three measurements (Table 3.1.).

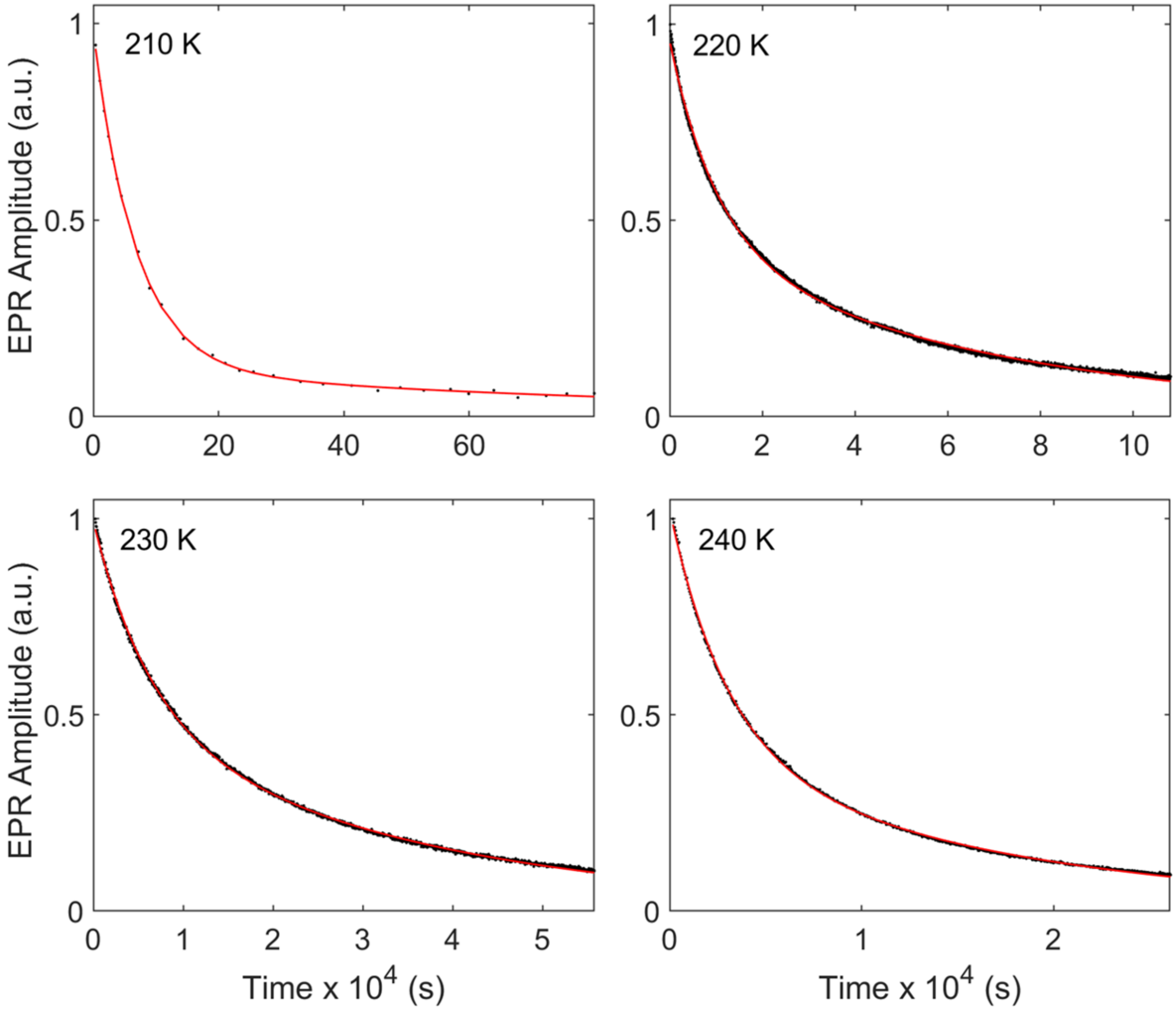

Figure 3.5. The time-dependence of the EPR amplitude of the substrate radical component at the measured temperatures (black dots) overlaid with the best-fit biexponential functions (red line). The EPR amplitude is normalized to the zero-time value.

3.3.4.2. Cryotrapped 2-aminopropanol substrate radical intermediate in EAL with 2 and 4 % v/v DMSO solution, measured at 230 K and 240 K

The amplitude of the decay of the cryotrapped 2-aminopropanol substrate radical species is measured at T of 230 K and 240 K in solution of EAL with 2 or 4 % v/v DMSO. The time-dependence of the radical pair amplitude decay is shown in Figure 3.7 (A and B for 2 % v/v DMSO and C and D for 4 % v/v DMSO). The high field trough is monitored to a decay level of ~ 9 % from the initial amplitude for the substrate radical to identify all components that are involved in the kinetics of the system. The best fits to theoretical decay functions are overlaid (red line) with the experimental data (black dots). The time-dependence amplitude curves are well fitted by a biexponential function at the measured T values, 230 K and 240 K. The information from the fits describe the kinetic process through the first-order rate constants and normalized amplitudes for the two components (slow- and fast-phase observed rate constants $k_{obs,s}$ and $k_{obs,f}$, and corresponding normalized amplitudes $A_{n,s}$ and $A_{n,f}$). In Table 3.1. the mean values from three measurements at each T-step are reported together with the statistical measure of the fitting given by the mean of the Pearson's correlation coefficient R^2 over the three measurements.

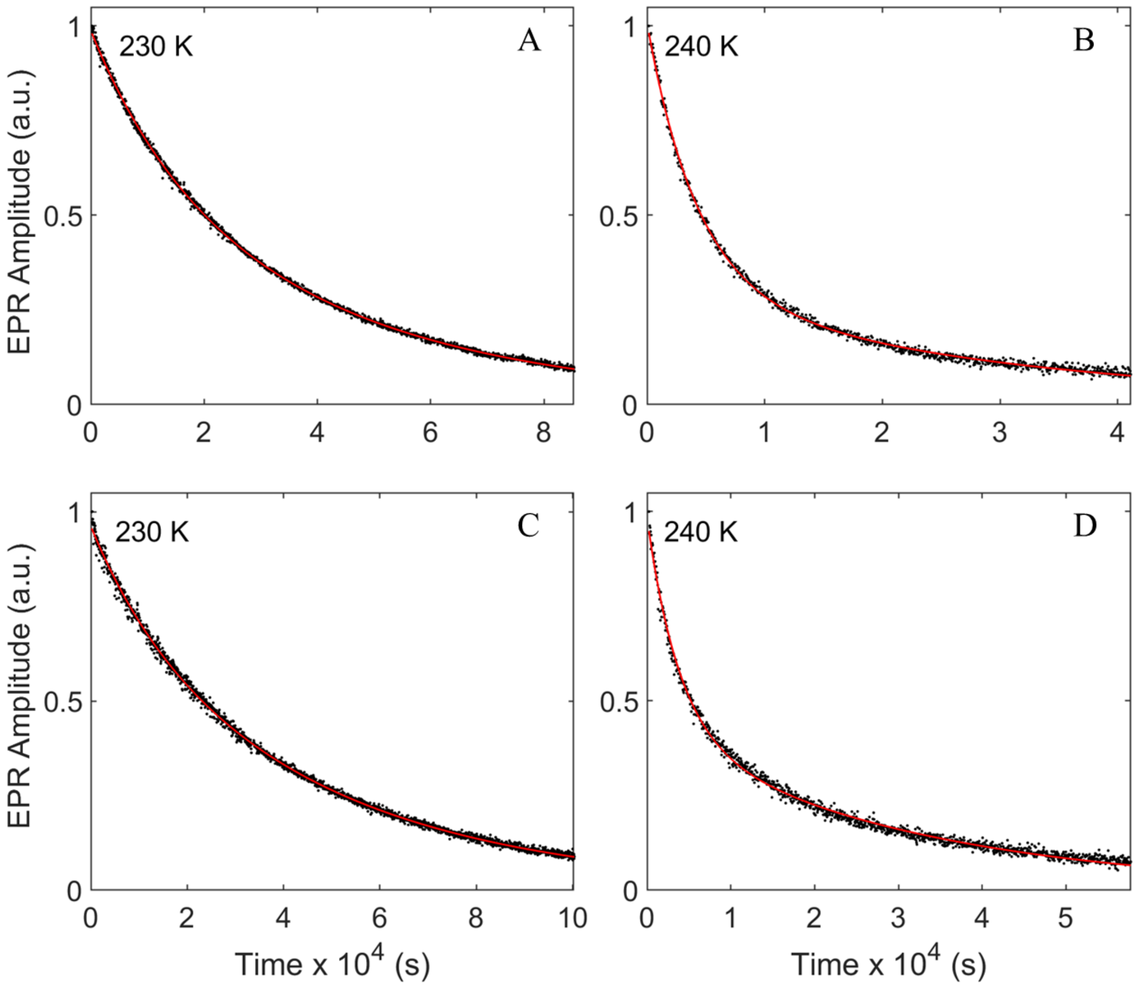

Figure 3.6. The time-dependence of the EPR amplitude of the 2-aminopropanol substrate radical component in the presence of 2 % v/v DMSO (A&B) and 4 % v/v DMSO (C&D) at selected temperatures (black dots) with overlaid best-fit biexponential functions (red line). The EPR amplitude is normalized to the zero-time value.

Table 3.1. First-order rate constants and normalized amplitude parameters for the biexponential fitting to the decay kinetics of the Cbl(II)-substrate radical pair at indicated temperatures and added % v/v DMSO. Parameters represent the mean values, ± standard deviation, for three separate decay measurements.

% v/v DMSO	*T(K)*	$k_{obs,s} \times 10^{-4}$ (s^{-1})	$k_{obs,f} \times 10^{-4}$ (s^{-1})	$A_{s,n}$	$A_{f,n}$	R^2
0	210	0.027 ± 0.005	0.19 ± 0.04	0.16 ± 0.05	0.84 ± 0.05	0.9992 ± 0.0004
	220	0.15 ± 0.01	1.06 ± 0.07	0.45 ± 0.01	0.55 ± 0.01	0.9992 ± 0.0003
	230	0.36 ± 0.06	2.1 ± 0.44	0.55 ± 0.06	0.45 ± 0.06	0.9990 ± 0.0005
	240	0.69 ± 0.09	3.57 ± 0.32	0.42 ± 0.04	0.58 ± 0.04	0.9994 ± 0.0002
2	230	0.22 ± 0.02	0.77 ± 0.27	0.63 ± 0.10	0.37 ± 0.10	0.9993 ± 0.0001
	240	0.34 ± 0.04	2.54 ± 0.31	0.34 ± 0.04	0.66 ± 0.04	0.9976 ± 0.0003
4	230	0.19 ± 0.05	0.71 ± 0.26	0.65 ± 0.24	0.35 ± 0.24	0.9985 ± 0.0001
	240	0.28 ± 0.10	2.54 ± 0.35	0.43 ± 0.03	0.57 ± 0.03	0.9927 ± 0.0034

3.3.5. Time-dependence of the growth of the uncoupled Cbl(II)

3.3.5.1. EPR measurements for EAL and 2-aminopropanol in 0 % v/v DMSO solution at *T* in the range 210-240 K

The formation of the uncoupled Cbl(II) and radical species is studied through monitoring in time the growth of the Cbl(II) feature at $g_{\perp} = 2.32$ from the deconvoluted EPR spectra. The time-dependence of the amplitude of the uncoupled Cbl(II) peak relative to the baseline at low field for *T* values over the range 210-240 K is shown in Figure 3.8. The exponential growth curves are well fitted by a monoexponential function for the measurements at 210 K and biexponential function for the experiments over the range 220-240 K. The best fits are overlaid with the experimental data. The values of the first-order rate constants and normalized amplitudes for the two components (slow- and fast-phase observed rate constants $k_{obs,s}$ and $k_{obs,f}$, and corresponding normalized amplitudes $A_{n,s}$ and $A_{n,f}$) are reported as mean values from three measurements at each T-step, together with the statistical measure of the fitting given by the mean of the Pearson's correlation coefficient R^2 over the three measurements (Table 3.2.).

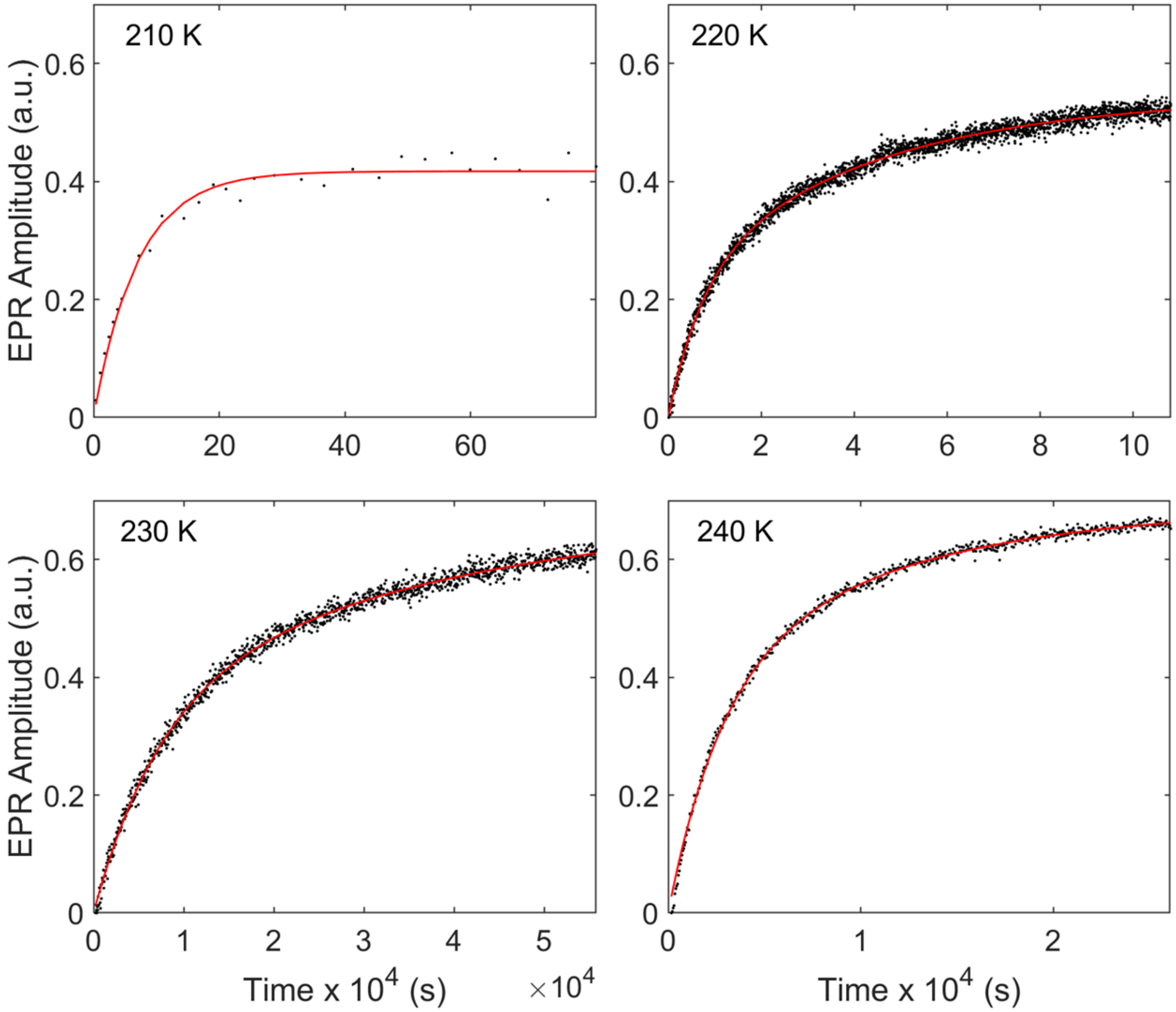

Figure 3.7. The time-dependence of the EPR amplitude of the uncoupled Cbl(II)- radical state component at the measured temperatures (black dots) overlaid with the best-fit mono or biexponential functions (red line). The EPR amplitude is scaled to the AUC for the uncoupled Cbl (II) radical species.

3.3.5.2. EPR measurements for EAL and 2-aminopropanol in 2 and 4 % v/v DMSO solution at T of 230 K and 240 K

The growth of the Cbl(II) feature at $g_{\perp}$ from the deconvoluted EPR spectra of the uncoupled Cbl(II) and radical species is measured at *T* of 230 K and 240 K in solution of EAL with 2 or 4 % v/v DMSO. The time-dependence of the uncoupled Cbl(II) formation is shown in Figure 3.9 (panel A 2 % v/v DMSO and panel B 4 % v/v DMSO). The growth curves are well fitted by a monoexponential function at the measured *T* values, 230 K and 240 K, with the best fits overlaid with the experimental data. (red lines in Figure 3.9) The kinetic process is described by the observed first-order rate constant ($k_{obs,s}$) and normalized amplitude ($A_{n,s}$) reported in Table 3.2 as the mean value of three measurements at each *T*-step. The statistical measure of the fitting at each *T* is given by the mean of the Pearson's correlation coefficient R^2 over the three measurements.

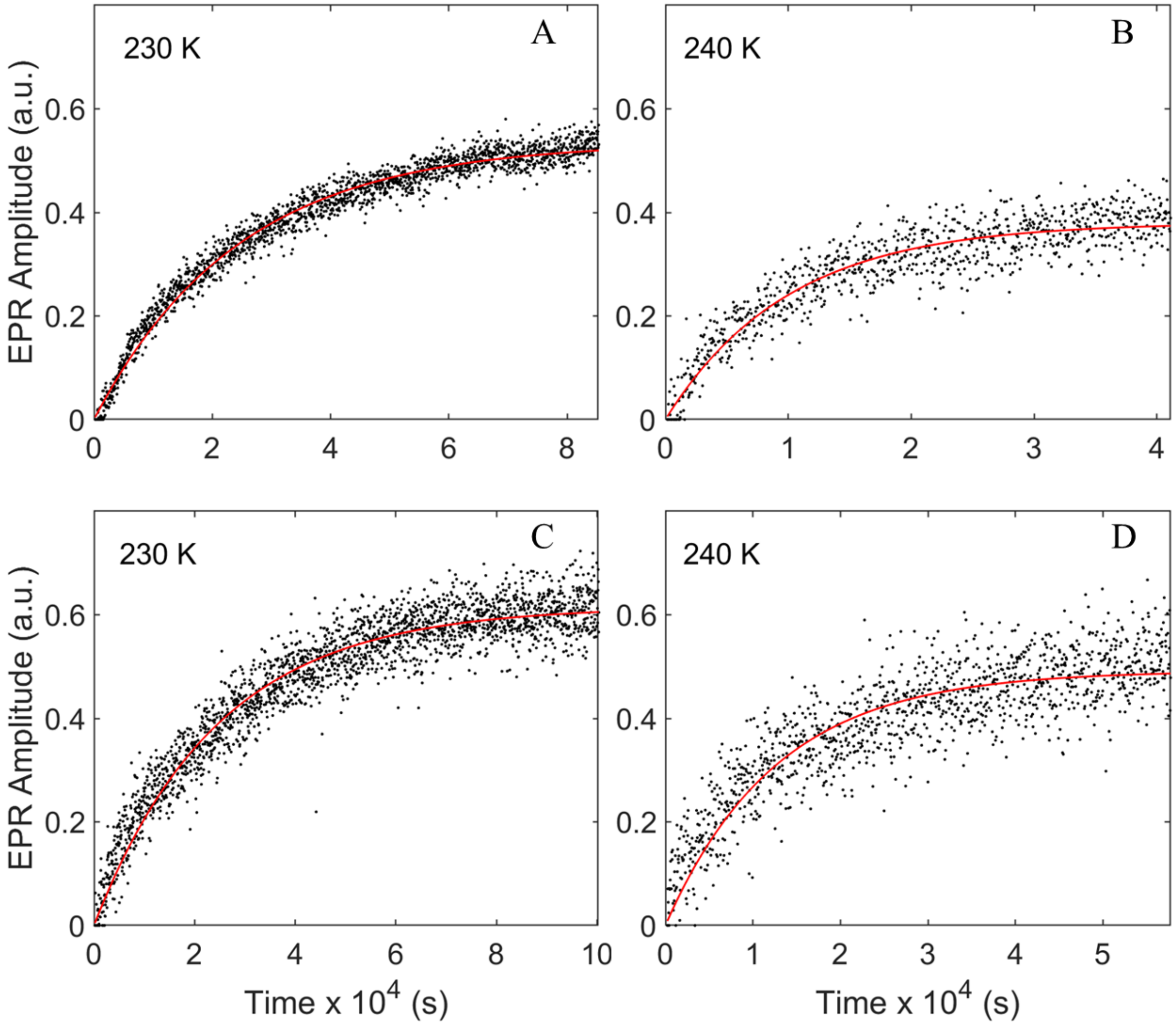

Figure 3.8. Time-dependence of the EPR amplitude of the uncoupled Cbl(II) (black dots) deconvoluted from the total EPR signal recorded during decay of the cryotrapped 2-aminopropanol substrate radical intermediate in EAL in the presence of 2 % v/v DMSO (A) and 4 % v/v DMSO (B) at selected temperature. Overlaid are the best-fit monoexponential functions (red line). The EPR amplitude is scaled to the AUC for the uncoupled Cbl (II) radical species.

Table 3.2. First-order rate constants and normalized amplitude parameters for the mono- and bi-exponential fitting to the growth curves of the uncoupled Cbl(II) at indicated temperatures and added % v/v DMSO. Parameters represent the mean values, ± standard deviation, for three separate measurements.

% v/v DMSO	*T (K)*	$k_{obs,s} \times 10^{-4}$ (s^{-1})	$k_{obs,f} \times 10^{-4}$ (s^{-1})	$A_{s,n}$	$A_{f,n}$	R^2
0	210	-	0.21 ± 0.07	-	1 ± 0.00	0.9613 ± 0.020
	220	0.30 ± 0.13	1.84 ± 0.89	0.59 ± 0.08	0.41 ± 0.08	0.9888 ± 0.007
	230	0.40 ± 0.22	3.00 ± 1.66	0.60 ± 0.13	0.40 ± 0.13	0.9912 ± 0.007
	240	0.96 ± 0.16	4.34 ± 1.34	0.48 ± 0.03	0.52 ± 0.03	0.9933 ± 0.004
2	230	0.51 ± 0.12	-	1 ± 0.00	-	0.9436 ± 0.028
	240	1.12 ± 0.23	-	1 ± 0.00	-	0.8281 ± 0.041
4	230	0.36 ± 0.05	-	1 ± 0.00	-	0.9333 ± 0.009
	240	0.65 ± 0.30	-	1 ± 0.00	-	0.7645 ± 0.072

3.3.6. Steady-state kinetic measurement

Figure 3.9 shows the EPR signal of the Cbl(II)-substrate radical pair measured at 120 K from samples incubated at 288 K for different time intervals. The stack plot shows from the top to bottom the normalized signal recorded from each sample with the corresponding incubation time (0, 1, 5, 10, 20, 30 min). The time evolution of the signal amplitude (better depicted in Appendix C, Figure C.1) and line shape shows both an abrupt decrease in the signal amplitude of the substrate radical (second trough of the lineshape) and change in lineshape of the first two peaks from 10 min incubation time to 20 min and 30 min respectively. The line shape change in both, the low field peak of Cbl(II) from a broadened split feature to a single peak, and the substrate radical peak feature that loses amplitude and splits, are indicative of the formation of uncoupled Cbl(II) and radical species as described earlier. The lineshape of the Cbl(II) low field peak feature has a visible change from the first minute and a half of incubation. It is interesting to observe that the high *T* reveals the presence of the uncoupled Cbl(II) and radical species identified at low *T* which has not been reported previously. The uncoupled Cbl(II) was deconvoluted as described earlier and the proportion of the species was determined from AUC values at each decay time measured. The time evolution of the uncoupled species was plotted with the ERP amplitudes scaled to the AUC value determined for the final decay time measured considering that time zero has 100 % radical pair.

The time-dependence of the amplitudes of the substrate radical and uncoupled Cbl(II) features indicates that the 10 mM concentration of substrate in the sample is consumed over 20 min. (Figure 3.10) At 288 K the substrate radical shows a linear decrease in amplitude over time, while the rise of uncoupled Cbl(II) follows a monoexponential growth with the best fit indicated in figure 3.10. The product formation which is the remaining of the % normalized amplitude is also represented in the time-dependence plot. The linear behavior of the substrate radical signal over time in the steady-state experiment at 288 K suggests the presence of underlying processes that drive the substrate consumption and enzyme function in the high physiological *T* region. As the substrate is being consumed diamagnetic product and Cbl(II) and radical species are formed, with the latter acting as a suicide pathway for the sites that produce it which become inactive. However, formation of diamagnetic product leads to available active sites upon its release, and they can be replenished by the available substrate. The process of product release and replenishment of the active site is continuous at 288 K and in the 10 min the active sites are populated in high percentage, but with every substrate turnover less substrate and less active sites being available. The overall dependence shows that over time as the substrate is consumed less sites are being replenished. The linear time-dependence of the substrate radical signal is also associated with the presence of a backpressure created by accumulation of product in the sample solution which acts as an inhibitor suppressing the replenishment of the active sites.

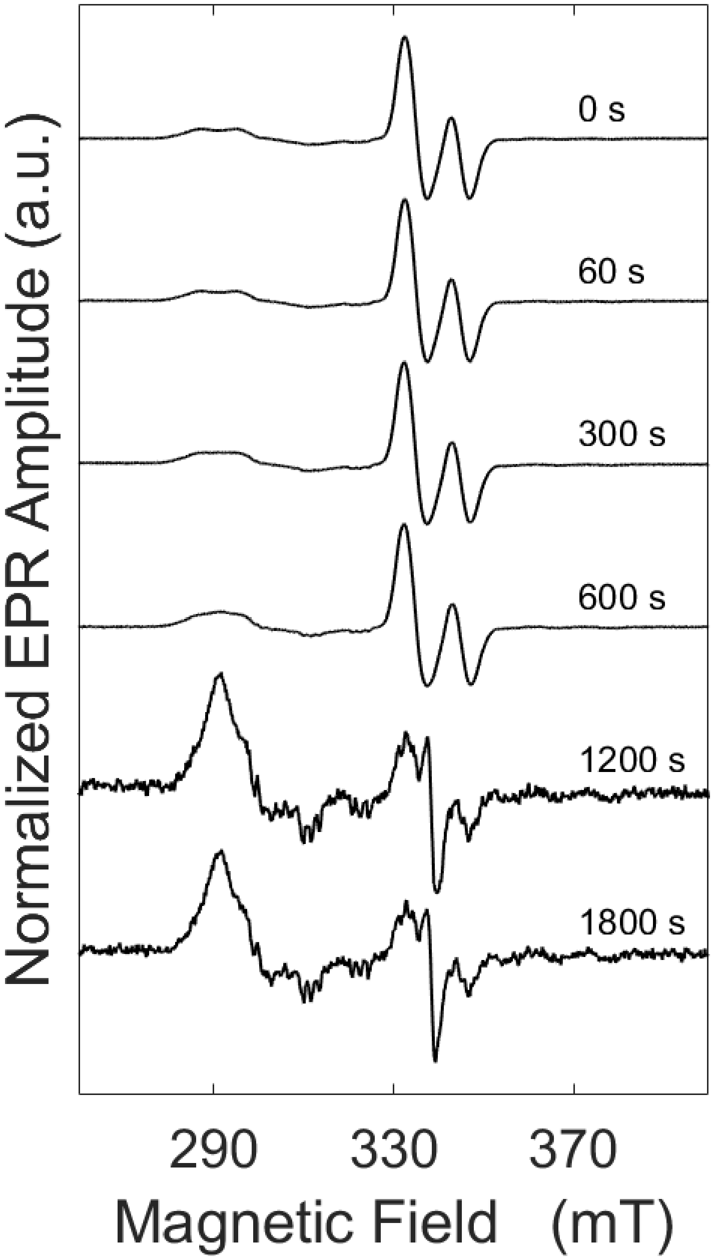

Figure 3.9. Time-dependence of the Cbl(II)- 2-aminopropanol substrate radical pair state in EAL. The signal was measured at 120 K and each scan corresponds to a sample incubated at 288 K for the time interval indicated. The EPR amplitude is normalized to the peak-to-trough amplitude of the radical signal in each scan.

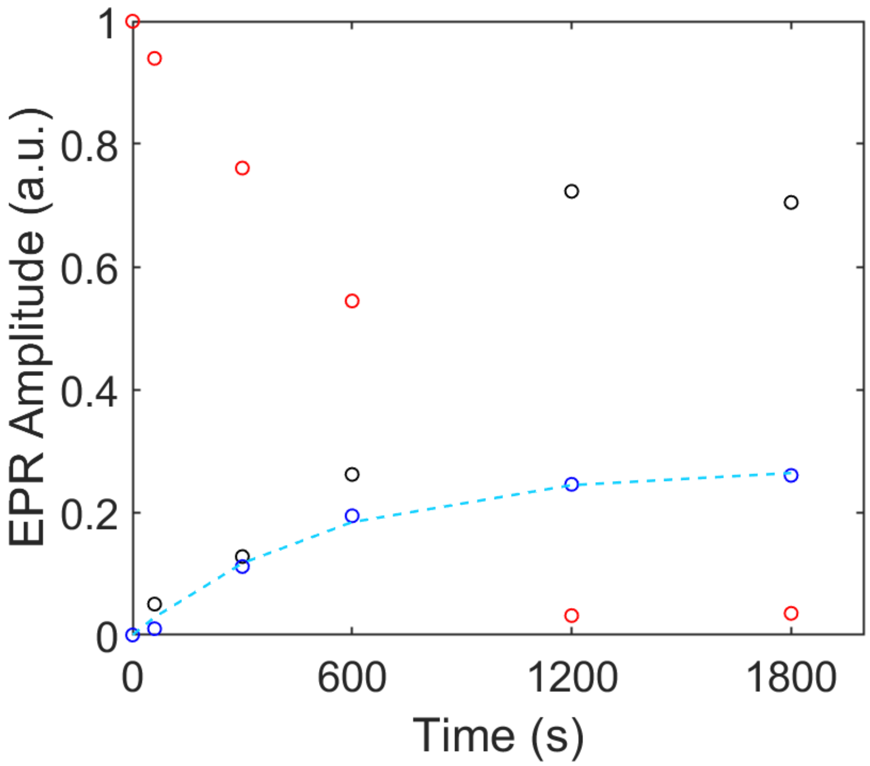

Figure 3.10. The time-dependence of the EPR amplitude of **S$^\bullet$** (red), **X$^\bullet$** (blue) and **PH** (black) from the EPR signal measured at 288 K. The EPR amplitude of the substrate radical feature is normalized with respect to the zero-time value and the amplitude of the uncoupled Cbl(II)- radical state feature is scaled to the AUC determined for the uncoupled Cbl (II) radical species as indicated above. The best-fit monoexponential function to the growth of **X$^\bullet$** is shown in dash light blue line.

3.4. Discussion

3.4.1. Kinetic Model. Microscopic rate constants for protein configurational change and rearrangement reaction steps

The time-dependence of the Cbl(II)-substrate radical pair decay and of the growth of the uncoupled Cbl(II) components were modeled using a minimal three-step/ four-state kinetic mechanism previous applied to the EAL kinetics when using aminoethanol and 2-aminopropanol as substrates(Figure 3.11).[76, 77] The Cbl(II)-2-aminopropanol substrate radical pair decay occurs from two sequential protein configurational states, $\mathbf{S_1^\bullet}$ and $\mathbf{S_2^\bullet}$, which interchange at the rates of k_3 and k_4. The protein misfires and forms uncoupled Cbl(II) and radical species from the decay of the nascent substrate radical state, $\mathbf{S_1^\bullet}$ with the first-order rate constant k_1, while the diamagnetic product formation was enabled by the radical rearrangement state, $\mathbf{S_2^\bullet}$ with the rate constant k_2. The evolution of states is conserved in time (equation 3.9), as at any t>0 the sum of the concentration of the species equals the initial concentration of the radical pair as determined by the AUC values for each sample.

$$[\boldsymbol{S^\bullet}_{\boldsymbol{tot}}]_0 = [\boldsymbol{S^\bullet}_{\mathbf{1}} + \boldsymbol{S^\bullet}_{\mathbf{2}}]_t + [\boldsymbol{X^\bullet}]_t + [\boldsymbol{P}]_t \tag{3. 9}$$

The substrate radical decay is measured as the disappearance of the combined EPR signal of the indistinguishable $\mathbf{S_1^\bullet}$ and $\mathbf{S_2^\bullet}$ states. Thus, the numerical simulations of the time dependent amplitudes of the decay are done considering the form of a total $\mathbf{S^\bullet}$ state, $\mathbf{S_1^\bullet}$+ $\mathbf{S_2^\bullet}$. The diamagnetic product is obtained from subtracting the uncoupled Cbl(II) amplitude from the inverse of substrate radical decay amplitude, as indicated by the conservation relation, equation 3.9. The set of solutions of the differential equations that describe the model defined by $\mathbf{S^\bullet}$(t), **P**(t) and $\mathbf{X^\bullet}$(t) (equations C1-C3 in Appendix C) are simulated, presenting a good fit to the experimental data.(Figure 3.12) A slightly modified kinetic model was also considered and the results are reported in the Appendix C. This model maintains the same number of states and steps, but the diamagnetic product and uncoupled species pathways both occur from the radical rearrangement state, $\mathbf{S_2^{\bullet}}$ (Figure C.2 in Appendix C). Although the alternative model captures the experimentally observed growth of the fast component of the uncoupled Cbl(II) or product, it considers two hybrid conformations of the substrate radical in the radical rearrangement state $\mathbf{S_2^{\bullet}}$ ($\mathbf{S_2^{\bullet}}$’ and $\mathbf{S_2^{\bullet}}$”) that determine the fate of the pathway. In order for this model to be valid a method for distinguishing between the two $\mathbf{S_2^{\bullet}}$ conformations of the substrate radical would be required.

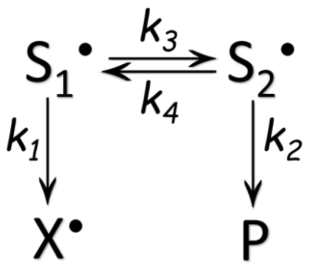

Figure 3.11. Microscopic kinetic models tested for the mechanism of the Cbl(II)-2-aminopropanol substrate radical pair decay in EAL.

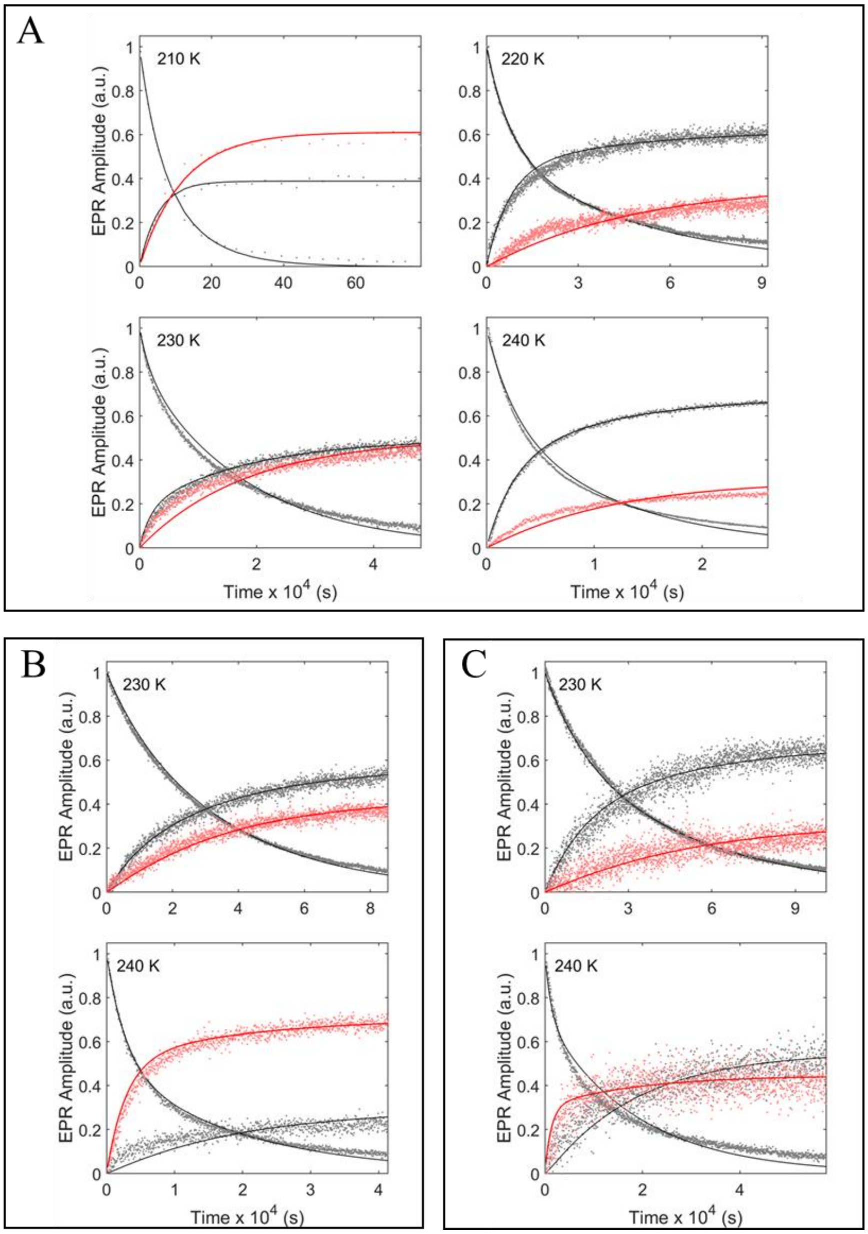

Figure 3.12. Time-dependence of the deconvoluted Cbl(II)-2-aminopropanol substrate radical pair decay components in EAL and % DMSO at the corresponding measured *T* values overlaid with simulated components of the kinetic model: A. 0 % v/v DMSO, B. 2 % v/v DMSO and C. 4 % v/v DMSO. Representative single data set for each *T* is shown. The components obtained from measurement (decay of substrate radical and growth of uncoupled Cbl(II)) are indicated in grey dots with the corresponding overlapped black lines for $\mathbf{S}^{\bullet}$(t) and $\mathbf{X}^{\bullet}$(t) simulations. The diamagnetic product is shown in light red dots with the simulated **P**(t) in red line.

3.4.2. Arrhenius behavior of the observed rate constants

Figure 3.13 shows the Arrhenius plot of the observed rate constants determined from the exponential fits to the decay of the Cbl(II)-2-aminopropanol substrate radical pair state and to the growth of the uncoupled Cbl(II) and radical species in EAL in the absence of the cosolvent DMSO from 210 to 288 K. Over 220-240 K, the kinetics of both the radical pair decay and the uncoupled species rise display biexponential evolution, with the observed rate constants, $k_{obs,s}$ and $k_{obs,f}$, for both species overlapping within approximately one standard deviation. This congruence indicates that the two microstates, $\mathbf{S_1^\bullet}$ and $\mathbf{S_2^\bullet}$, interconvert rapidly on the time scale of the reactions from $\mathbf{S_1^\bullet}$ and $\mathbf{S_2^\bullet}$. For 220- 240 K, the substrate radical decay is measured as the disappearance of the combined EPR signal of the indistinguishable $\mathbf{S_1^\bullet}$ and $\mathbf{S_2^\bullet}$ signals, which gives a two-component decay. The growth of the uncoupled species is measured as the increase in the single branch species, $\mathbf{X^\bullet}$, which also displays the biphasic kinetics, owing to the $\mathbf{S_1^\bullet}$ and $\mathbf{S_2^\bullet}$ exchange. Thus, measurements of both $\mathbf{S^\bullet\,(S_1^\bullet + S_2^\bullet)}$ and $\mathbf{X^\bullet}$ provide the same slow and fast observed rate constants. The rate constants determined from empirical fittings are not the microscopic rate constants, but composites of the first-order rates (k_1,k_2, k_3, k_4) that describe the kinetic model, denoted as κ_+ (for $k_{obs,f}$) and κ_- (for $k_{obs,s}$). Thus, the T-dependence of κ_+ and κ_- over 220-240 K in Figure 3.13 does not correspond to an Arrhenius relation for a single step, first-order rate process.

At 210 K, the radical pair decay has a biexponential kinetics, while the uncoupled species grow monoexponentially with the observe rate constant identical to the fast component of the radical pair decay. This result suggests that each of the two microstates is responsible of only one of the two outcomes of the reaction: forming the diamagnetic product state, **P**, or forming the uncoupled species, $\mathbf{X^\bullet}$. This indicates that the exchange between the microstates $\mathbf{S_1^\bullet}$ and $\mathbf{S_2^\bullet}$ is quenched on the time scale of the $\mathbf{S_1^\bullet \rightarrow X^\bullet}$ and $\mathbf{S_2^\bullet \rightarrow P}$ reactions. The biexponential kinetics in the decay process indicates the observation of the loss of the (**S$_1$$^\bullet$** + **S$_2$$^\bullet$**) EPR signal which give the components for the reaction from each microstate. The monoexponential kinetics is characterizing only one pathway, namely the formation of **X$^\bullet$** from **S$_1$$^\bullet$**. This suggest that the fast component of the (**S$_1$$^\bullet$** + **S$_2$$^\bullet$**) decay represents the **S$_1$$^\bullet$→X$^\bullet$** reaction, k_1, while the slow component identifies with the **S$_2$$^\bullet$→P** reaction, k_2. Under this considerations, and following the kinetic model results we identified that transition **S$_2$$^\bullet$** to **S$_1$$^\bullet$** was considerably slowed down at 210 K, by approximately 10-fold, essentially quenched on the time scale of the reaction. The apparent deviation of the 210 K data from a linear extrapolation of the 220 – 240 K data in Figure 3.13 is caused by the different exchange regimes.

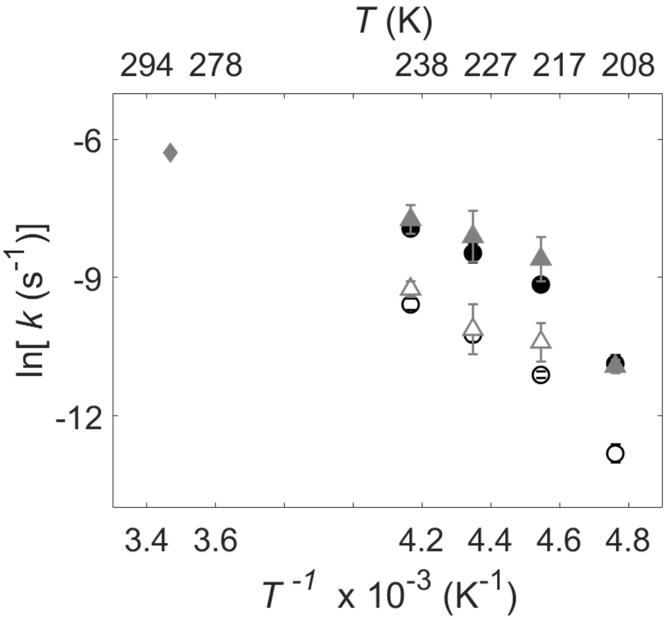

Figure 3.13. Arrhenius plot of the mean first order rate constants from the mono/biexponential fittings of the substrate radical decay (circles) and deconvoluted uncoupled Cbl(II) radical species (triangles). The 288 K rate constant for the uncoupled Cbl(II) is indicated in diamond. The fast (solid) and slow (open) rate constants correspond to the reaction kinetics measured in the T range 210-240 K in the absence of DMSO. The error bars represent the relative standard deviation for three separate decay measurements.

At 288 K only the growth of the uncoupled radical species is resolved, and it has a monoexponential kinetics with the rate constant of 4 times magnitude higher than the low *T* fast component. The determined rate constant at (1.8×10^{-3} s^{-1}) at 288 K is ~30-fold less than the first-order decay of the Cbl(II)-substrate radical pair to the adenosylcob(III)alamin resting state in solution at 278 K (5.6×10^{-2} s^{-1}). The significant difference between these values is consistent with a rapid exchange condition, k_4, $k_3 >> k_1$, k_2. Thus, at room *T* the exchange rates between the microstates $\mathbf{S_1^\bullet}$ and $\mathbf{S_2^\bullet}$ are fast relative to the **P** and $\mathbf{X^\bullet}$ formation. The linear time-dependence of the substrate radical pair signal is given by the exponential reduction in available active sites due to formation of the uncoupled radicals and to the product inhibition. The high *T* reveals the presence of the uncoupled Cbl(II) and radical species identified at low *T*, but in lower proportions (about 50 % less $\mathbf{X^\bullet}$ produced, ~ 25 %), the formation of diamagnetic **P** being the dominant pathway of the reaction. In this case, the observed rate constants represent κ_- and κ_+ in the high-*T* limit. The relatively slow growth time scale of the uncoupled species is dominated by the κ_- component, but the κ_+ component is not resolved. The decay of the Cbl(II)-substrate radical pair is driven chiefly by the rapid depletion of substrate through the more rapid product formation reaction, which is dominated by κ_+.

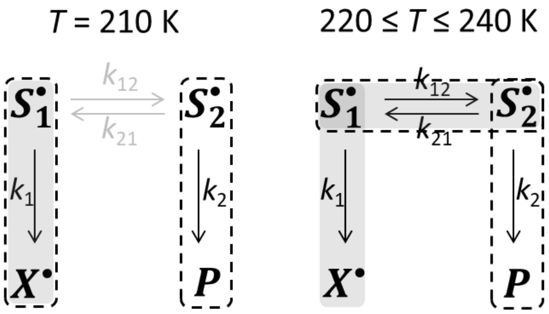

Figure 3.14. Kinetic scheme. The kinetic model for the decay of the 2-ampropanol substrate radical in EAL at 210 K and over the *T* range of 220-240 K. Black arrows correspond to reactions that contribute to the kinetics measured by the decay of $\mathbf{S_1^\bullet}$ + $\mathbf{S_2^\bullet}$. Grey pathway corresponds to states that contribute to kinetics measured by the rise of $\mathbf{X^\bullet}$. The grey arrow indicates slow/quenched reaction.

In the presence of cryosolvent, the decay of the 2-aminopropanol generated substrate radical pair follows a biexponential while the growth of the uncoupled Cbl(II) has a monoexponential behavior. This was observed for EAL in the presence of 2 % and 4 % v/v DMSO at measured *T* values of 230 K and 240 K. Under these conditions, the Arrhenius type plot of the observed rate constants (Figure 3.15) indicates that the rate of growth of the uncoupled species do not overlap with neither of the rate constants of the substrate radical decay and falls in between the two components of $\mathbf{S^\bullet}$. However, the 2 % v/v DMSO results for the $\mathbf{S^\bullet}$ decay and $\mathbf{X^\bullet}$ growth overlap with the respective rates for $\mathbf{S^\bullet}$ and $\mathbf{X^\bullet}$ determined for 4 % v/v DMSO within one standard deviation. Overall, the % v/v DMSO lowers the rate constants for $\mathbf{S^\bullet}$ decay but maintains the rates for $\mathbf{X^\bullet}$ rise at the values of the slow rates determined for samples in the absence of DMSO at the corresponding *T* values. The presence of DMSO increases the fluid dynamics in the PAD and favors a rapid exchange condition, comparable to the direct reactions from $\mathbf{S_1^\bullet}$ and $\mathbf{S_2^\bullet}$ states to **P** or $\mathbf{X^\bullet}$, $k_3,k_4 \approx k_1,k_2$.

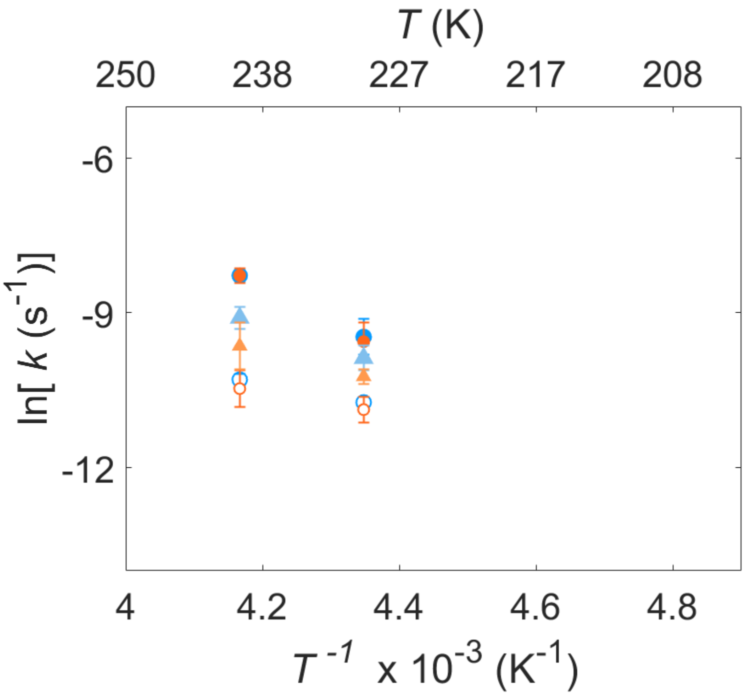

Figure 3.15. Arrhenius plot of the mean first order rate constants from the mono/biexponential fittings of the substrate radical decay (circles) and deconvoluted uncoupled Cbl(II) radical species (triangles). The fast (solid) and slow (open) rate constants from the reaction kinetics measured at *T* values of 230 K and 240 K in the 2 % and 4 % v/v DMSO system are shown in blue and orange. The error bars represent the relative standard deviation for three separate decay measurements.

3.4.3. Contributions of the protein-solvent dynamical coupling to protein configurational change and rearrangement reaction steps

The TEMPOL spin probe detects the ODT in the PAD solvent dynamics in the *T* interval, 230-235 K for EAL with 10 mM 2-aminopropanol, and 205-210 K for EAL with 10 mM 2-aminopropanol and 2 % v/v DMSO. The Arrhenius plot of the first-order rate constants, or microscopic rate constants, determined from numerical simulations is presented in Figure 3.16 for reaction kinetics in the absence (0 %, panel A) or presence (2,4 % v/v, panels B and C) of DMSO. For 0 % v/v DMSO condition, the microscopic rate constants differ by less than 100-fold at 220, 230 and 240 K, showing that the system is in the exchange regime, where $k_1 > k_3$, $k_2 = k_4$. In the 210-240 K region k_3 and k_4 display non-linear, non-Arrhenius behavior. The values are constant over 230-240 K, and then begin to decrease at 220 K. In order to accommodate the isolated decays from $\mathbf{S_1}^{\bullet}$ and $\mathbf{S_2}^{\bullet}$ at 210 K, and therefore the condition k_3, $k_4 << k_1$, k_2, the k_3, k_4 relation extrapolates to below the measured data points at 210 K as shown in Figure 3.16 panel A. The T-dependence of k_3, k_4 indicates the emergence of a free energy barrier to $\mathbf{S_2}^{\bullet}$, $\mathbf{S_1}^{\bullet}$ interconversion, with decreasing T, at the T value of the ODT. Therefore, fluctuations in the PAD solvent are coupled to the protein configurations and fluctuations that conduct and define the $\mathbf{S_1}^{\bullet}\leftrightarrow\mathbf{S_2}^{\bullet}$ interconversion. Over the T range of the ODT from 230 – 240 K, the plateau in k_3, k_4 T-dependence indicates an approximately constant activation free energy ($\Delta G^{\ddagger}$), that arises from a compensation of activation enthalpy ($\Delta H^{\ddagger}$) and entropy ($T\Delta S^{\ddagger}$) terms. Specifically, both $\Delta H^{\ddagger}$ and $\Delta S^{\ddagger}$ increase with decreasing T. This suggests that the plateau in the ln$k$ versus 1/T dependence resolves the formation region of the free energy barrier to $\mathbf{S_1}^{\bullet}\leftrightarrow\mathbf{S_2}^{\bullet}$ interconversion. The transition in PAD solvent dynamics also raises the free energy barriers to chemical reaction, $\mathbf{S_1}^{\bullet}\rightarrow\mathbf{X}^{\bullet}$. This is shown by the increasing negative slope of the k_1 relation with decreasing T. The less dramatic increase in free energy barrier to the reactions, relative to the barrier for the $\mathbf{S_1}^{\bullet}\leftrightarrow\mathbf{S_2}^{\bullet}$ configurational interconversion, may arise from a dominant energetic contribution of the intrinsic bond-breaking and re-making events.

The T values at which the kinetics in % DMSO solution is measured is well above the ODT temperature determined in the PAD for EAL with 10 mM 2-aminopropanol and 2 % v/v DMSO. The decreased ODT T region to 205-210 K by the addition of 2 % v/v DMSO, was proposed to drive the reaction to all monoexponential decay into only productive pathway with no site inactivation which would have been observed at higher T in the 0 % DMSO, above the measured T values. However, the only reaction that becomes monoexponential is the destructive pathway, the decay maintaining its biphasic characteristics. Above the ODT, the system is in the exchange regime with the rates between the two microscopic states $\mathbf{S_1}^{\bullet}$ and $\mathbf{S_2}^{\bullet}$ being comparable to the reaction rates of **P** and $\mathbf{X}^{\bullet}$ formation. For reaction solution with 2 and 4 % v/v DMSO the first-order rate constant that characterize the $\mathbf{S_1}^{\bullet} \rightarrow \mathbf{X}^{\bullet}$ reaction, k_1, remains constant with increase in T, the plateau suggesting a constant activation free energy. In contrast, k_2 increases by 10-fold with increase in T, indicating a rise in the free energy barrier to product formation. In addition, in 2 % DMSO solution the T increase does not affect the reverse reaction of the exchange step, k_4, but causes a decrease in the forward reaction, k_3. In 4 % DMSO solution the $\mathbf{S_1}^{\bullet} \leftrightarrow \mathbf{S_2}^{\bullet}$ interconversion step keeps k_3 constant at increase T while increasing k_4.

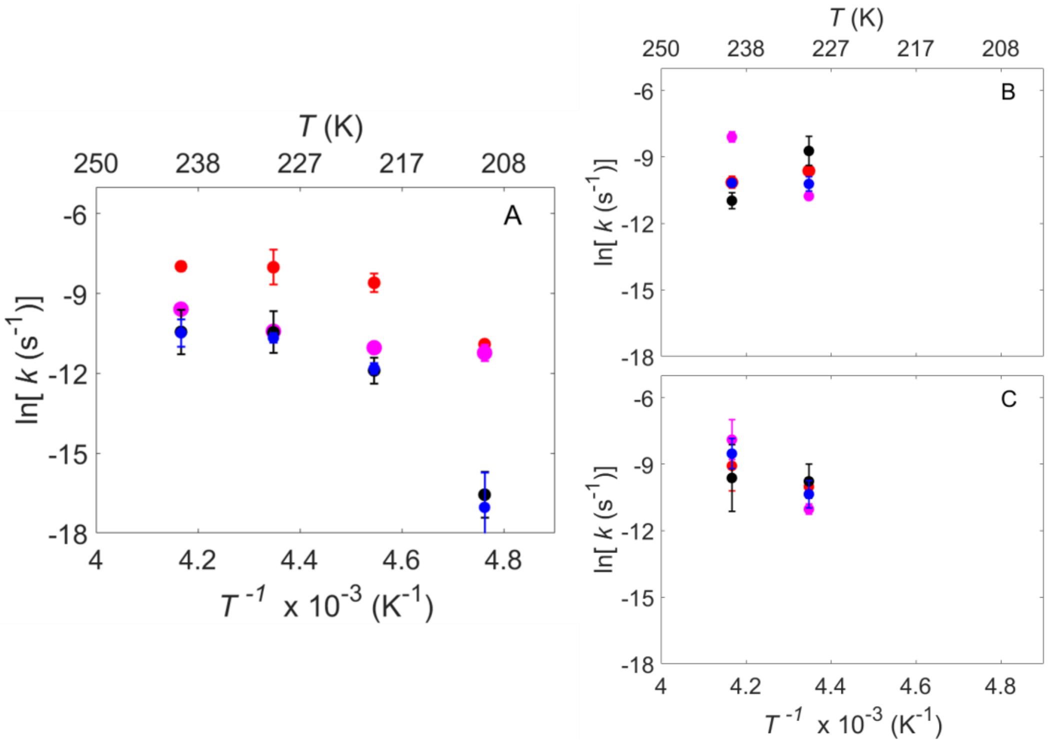

Figure 3.16. Arrhenius plots for the microscopic rate constants determined from the proposed kinetic model for Cbl(II)-substrate radical decay in EAL. The parameters (k_1 (red), k_2 (purple), k_3 (black) and k_4 (blue)) are determined for three data sets at each T value and are plotted for the different % v/v DMSO condition: 0 % (A), 2 % (B) and 4 % (C).

3.5. Conclusions

The pathway to non-productive (destructive), turnover-ending uncoupled Cbl(II) and radical species is consistent with the >100-fold lower reported k_{cat} for 2-aminopropanol versus aminoethanol, and the high substrate specificity of EAL and other Class II, eliminase B_{12}-dependent enzymes. In particular, of the two aminopropanol isomers (e.g., 2-amino-propan-1-ol and 1-amino-propan-2-ol) and their enantiomers, only [S]-2-amino-propan-1-ol has been reported to be converted directly to products by EAL. Therefore, the steric requirements for rearrangement catalysis are stringent. We propose that the steric effect of the 2-methyl group contributes to an increase to the barrier for $\mathbf{S_1^\bullet \leftrightarrow S_2^\bullet}$ interconversion that adds to the native protein configurational barrier (which is manifested as the sole barrier for aminoethanol substrate). This leads to the persistence of the biexponential decay at T values above the ODT, for 2-aminopropanol, but not for aminoethanol. As the T decreases through ODT, the protein configurational contribution to the barrier begins to dominate, and below the ODT, the protein configurational contribution effectively quenches the $\mathbf{S_2^\bullet \leftrightarrow S_1^\bullet}$ interconversion on the timescale of the decay reactions.

The contribution of the methyl-group steric impediment to the barrier to $\mathbf{S_1^\bullet \leftrightarrow S_2^\bullet}$ interconversion also accounts for the difference in the manifestation of k_3, k_4 effects for no DMSO or k_2 effects for 2 and 4 % DMSO on the T-dependent reaction rates. For aminoethanol, the barrier to $\mathbf{S_1^\bullet \leftrightarrow S_2^\bullet}$ interconversion changes from insignificant (k_3, $k_4 >> k_1$, k_2) to dominant (k_3, $k_4 << k_1$, k_2) with decreasing T over the narrow range between 220 and 214 K. This is because the barrier depends only on the solvent-coupled protein configurational barrier, and the solvent-coupling is linked to the sharp T-dependence of the effective quenching of collective, cooperative-cluster motions in the solvent. In contrast, the methyl-group steric contribution to the free energy barrier is expected to display a normal, linear Arrhenius T-dependence ($\Delta H^\ddagger$ and entropy $\Delta S^\ddagger$

contributions independent of *T*). The $\Delta G^\ddagger$ for $\mathbf{S_1}^\bullet \leftrightarrow \mathbf{S_2}^\bullet$ interconversion is comparable to the $\Delta G^\ddagger$ for the reactions of $\mathbf{S_1}^\bullet$ and $\mathbf{S_2}^\bullet$. The comparable values between the k_i may be related to similar steric penalties for configurational interconversion and reaction. The comparable values of the k_3, k_4 , k_1 and k_2 are expected to extend by 30 – 40 K into the physiological *T* range. Therefore, the results predict that the uncoupled Cbl(II) and radical species will be formed during steady-state turnover at physiological *T* values, in solution.

Chapter IV

Temperature-Dependence of the EPR Amplitude of Uncoupled Cbl(II) and Substrate Radical in EAL Provides a Direct Probe of Solvent Dynamics

4.1. Introduction

The B_{12}-dependent ethanolamine ammonia lyase (EAL) is the signature enzyme of the ethanolamine utilization (Eut) pathway [13] in pathogenic strains of *Salmonella* and *Escherichia coli* [23, 117] associated with microbiome disease conditions in the human gut, that catalyzes the conversion of substrate aminoethanol or the enantiomers, (S)- and (R)-2-aminopropanol, to acetaldehyde and ammonia,[52, 53] through a multi-step reaction cycle that uses radicals generated from the homolytic cleavage of the metal-carbon bond, Co-C, of the coenzyme-B_{12}.[48, 50, 61] In the kinetic reaction of Cbl(II)-substrate radical pair in EAL, the reaction is 100-fold slower when the substrate aminoethanol is substituted with 2-aminopropanol. With this substitution, the enzyme misfires when the native, specific protein configuration is not present, forming a non-native uncoupled Cbl(II) and free radical species. The isolated EAL strain from *Salmonella typhimurium* has been investigated by electron paramagnetic resonance (EPR) spectroscopy to gain insights into the fundamental aspects of its molecular mechanism and the modulation of its function by the surrounding environment. [61, 76, 77] The reaction kinetics were investigated over a wide low temperature (*T*) range (210-240 K) and leads to the resolution of individual steps in the core reaction-enabling and adiabatic-chemical events by using time-resolved, full-spectrum EPR spectroscopy.(Chapter 3) Spin probe EPR experiments under the same conditions showed that the persistence of the native reaction properties deep into the cryo-regime is promoted by the formation of a fluid mesodomain around EAL in the frozen aqueous solution, which maintains the protein hydration layer. The cosolvent-tunable dynamics provide a powerful probe of solvent-protein dynamical coupling to the EAL reactions. Here, we introduce the temperature dependence of the EPR amplitude as a probe of solvent dynamics, toward characterization of the solvent-protein-reaction dynamical coupling in EAL from *S. enterica serovar Typhimurium*.

The EAL protein in the frozen aqueous system is surrounded by concentric layers: a vicinal protein-associated domain (PAD, or hydration layer) and an aqueous mesodomain, whose thickness can be varied by the amount of added cosolvent.[78, 79] The substrates, which are akin to cryosolvents, are present in the mesodomain. The PAD undergoes a disordered-to-ordered transition (order-disorder transition, ODT) in the direction of decreasing temperature (T) that is detected by the EPR spin probe. In the aminoethanol reaction system, the ODT occurs over 219-220 K, and it is coupled to an energy barrier rise that leads to the kinetic bifurcation. In Chapter 2 it was shown that in the presence of 10 mM aminopropanol the ODT occurs over 230-235 K, and it is shifted by 25 K to 205-210 K by the addition of 2 % v/v dimethylsulfoxide (DMSO) cosolvent. Here, we address the influence of temperature, and the ODT in the PAD, on the EPR amplitude of the endogenous uncoupled Cbl(II) and the substrate radical in the radical pair in EAL.

4.2. Materials and methods

4.2.1. Sample preparation

The samples used for the experiments are the same samples that were measured for the kinetics reported in Chapter III and decayed to ~ 8-9 % from the initial amplitude for the substrate radical. At this low proportion of the radical pair (8-9 %) the sample is in the slow phase decay regime which allows measurements over a wide range of temperatures without losing signal due to reaction kinetics. All samples are stored in liquid nitrogen in 4 mm outer diameter EPR tubes (Wilmad-LabGlass) and contained a mixture of 20 μM purified EAL (120 μM active sites), with the initial concentrations for cofactor and substrate of 480 μM (adenosylcobalamin) and 10 mM ((S)-2-aminopropanol) in solution conditions of different percentages of DMSO (0 %, 2 % and 4% v/v) in 10 mM potassium phosphate buffer (pH 7.5).

4.2.2. Continuous wave-EPR Spectroscopy

The CW-EPR spectra were collected by using a Bruker E500 ElexSys EPR spectrometer equipped with a Bruker ER4122 SHQE X-band cavity resonator as described in section 2.1.2 of Chapter 2.

Temperature dependence. The experimental protocol is similar to the protocol for TEMPOL spin probe measurements which was described in section 2.1.2 of Chapter 2 and in previous work. [78, 79, 96] In brief, after calibration the T was set at the lower or higher limits of the measurement range (190-240 K) and a first EPR spectrum was collected. The next temperature was set and before collecting the spectrum the system was left at least 5 min to equilibrate and the cavity retuned. A dummy sample which was lacking the substrate was measured in a similar manner at each T value for baseline correction. The T was incremented in a 2 K step within a 10 K window around the T_{ODT} and a 5 K step outside this window. At the beginning and at the end of the T range a spectrum was collected at 120 K to monitor the consistency of the experiments. The EPR acquisition parameters used for these experiments were: 9.45 GHz microwave frequency; 2.0 mW microwave power; 10 Gauss magnetic field modulation; 100 kHz modulation frequency; 2600-4000 Gauss sweep width; 1024 points and 4-8 spectra were averaged at each T value. The temperature was controlled by using a Bruker ER4131VT temperature controller and cooling system that consists of a nitrogen gas flow through a coil immersed in liquid nitrogen bath contained in a 4 L dewar.

Power saturation. The experiments were done at 200 K and 235 K, over a microwave power range of 0.002-205 mW, which correspond to the attenuation settings of 50 - 0 dB of the Bruker microwave bridge (model ER 049X Super X). The parameters for the spectra acquisition were: 9.45 GHz microwave frequency,10 Gauss magnetic field modulation, 100 kHz modulation frequency, 2600-4000 Gauss sweep width; 1024 points. Each spectra consist of 4-16 averaged scans.

4.2.3. Progressive power saturation analysis

The EPR signal intensity dependence of the microwave power can be analyzed in terms of the degree of homogeneous/inhomogeneous broadening and the power for half-saturation. The empirical equation used to fit the experimental data is [132-135]:

$$I(P) = k(1 + \frac{P}{P_{1/2}})^{-b/2} \tag{4. 1.}$$

where P is the incident microwave power, $I(P)$ is the normalized EPR amplitude divided by the square root of P, $P_{1/2}$ is the power at which the EPR signal is reduced to half of the maximum achievable intensity and k is a constant. The equation allows for determining the parameters b and $P_{1/2}$. The inhomogeneity parameter, b, can take values from 1 to 3, which describes the extreme cases of purely inhomogeneous broadening (b=1) or purely homogeneous broadening (b=3). The method allows for the determination of $P_{1/2}$ values outside of the instrument power range.

Because the EPR signal of the EAL-bound paramagnets is inhomogeneously broadened, the inhomogeneity parameter b was fixed to 1 when fitting the progressive saturation curves for each of the studied species. The parameter $P_{1/2}$ was determined for all % DMSO conditions and each paramagnetic species in EAL by fitting the equation 4.1 to the corresponding experimental data by using the *lsqcurvefit* function. The fitting function uses the least squares regression analysis equation described in section 3.2.7 of Chapter 3.

4.3. Results and Discussion

4.3.1. Paramagnetic species in EAL after reaction with 2-aminopropanol

Figure 4.1 shows a representative set of spectra that indicate the origin of the signals observed in the *T*-dependence and power saturation measurements of the decayed cryotrapped Cbl(II)-2-aminopropanol substrate radical pair in EAL solution in the presence of different added % v/v DMSO. Panel A shows the zero-time and final-time spectra from a time-dependence measurement together with the deconvoluted signal from the final spectrum that grew upon decay, the uncoupled Cbl(II) and radical species. The final-time spectrum which is the decayed radical pair signal of the zero-time spectrum exposes new features as mentioned in Chapter 3. The new features can be resolved through spectral deconvolution methods described in section 3.4.2 of Chapter 3. The final-time spectrum is the type of signal that will be recorded at the different *T* and power values, and the features that will be analyzed are discussed further. The zero-time spectrum shows at low field the Cbl(II) feature of the radical pair, split by the interaction with the substrate radical. The final-time spectrum consists of a lower population of coupled Cbl(II) proportional to the population of substrate radical, and uncoupled Cbl(II) and radical species which dominate. The proportions of the coupled and uncoupled species for the samples measured are reported in Table D.1 of Appendix D. The deconvolution of the later species (black) is shown in panel B overlapped with the final-time spectrum (blue) to indicate the origin of the signals in the observed spectra. The uncoupled Cbl(II) signal has a strong low field feature in the absence of coupling with other paramagnetic species characterized by a single narrow peak that comes from the $g_{\perp}$. As it can be seen from the overlaid signal the low field (~290 mT) peak amplitude and its line shape are not changing upon deconvolution whereas the second peak (~330 mT) and second trough (~345 mT) are disappearing. Therefore, it can be argued that the features which are vanishing upon deconvolution belong to the Cbl(II)-substrate radical pair species. Although the final-time spectrum has both coupled and uncoupled Cbl(II), it can be seen here that the amplitude on the uncoupled Cbl(II) dominates. Thus, the low field peak can be associated with the uncoupled Cbl(II) signal referred further as Cbl(II). However, the central feature (~335 mT) is losing some amplitude and it is associated with the uncoupled radical species that are formed during decay. Considering these characteristics, the analysis of the *T*-dependence and power saturation of the signal is focusing on the amplitudes of the low field peak, Cbl(II), and of the high field trough, substrate radical (**S$^{\bullet}$**). In the present study this method and final-time types of spectra were measured at each *T* value, and the amplitudes are plotted in Figure 4.3.

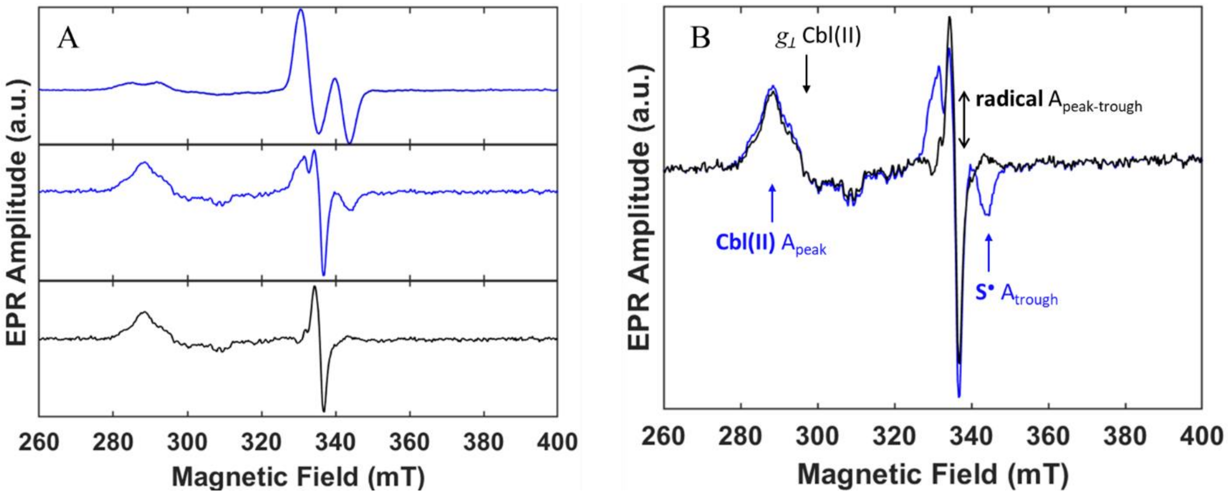

Figure 4.1. Representative EPR spectrum of the cryotrapped Cbl(II)-2-aminopropanol substrate radical pair and uncoupled species in EAL. Measurement conditions: 0% v/v DMSO; 220 K; 9.45 GHz microwave frequency; 2.0 mW microwave power; 10 Gauss magnetic field modulation; 100 kHz modulation frequency; 2600-4000 Gauss sweep width; 1 scan. In blue is the observed measured EPR signals and in black the deconvoluted EPR signal. A. The spectra from the time-dependence measurement show the observed zero-time (top) and final-time (middle) spectra, and the uncoupled signal (bottom) from the observed final time scan. The middle and bottom spectra are scaled by a factor of 3.7 for clarity. B. The final time observed (blue, middle in A) EPR spectrum overlaid to the corresponding deconvoluted spectrum of the uncoupled Cbl(II) and radical species (black, bottom in A). The radical species are indicated in black for the deconvoluted spectrum and in blue for the measured EPR signal. The Cbl(II) peak and **S**$^\bullet$ trough are the signals that will be analyzed further.

4.3.2. Cbl(II)-substrate radical pair EPR line shape. Temperature dependence in frozen aqueous solution after EAL reaction with 2-aminopropanol in the presence of DMSO: 0, 2 and 4 % v/v

As introduced in Chapter 1, the line shape of the cryotrapped cob(II)alamin (Cbl(II))-2-aminopropanol substrate radical pair in EAL presents features of the superhyperfine coupling of the Cbl(II) electron spin and ^{14}N nuclear spin from dimethylbenzimidazole (DMB) as well as the strong dipolar interaction with the substrate radical species. In the temporal decay of the Cbl(II)-substrate radical pair the substrate radical feature loses amplitude while uncoupled Cbl(II) and radical species features grow (see Chapter 3). The very low rate of decay at the end of the experiment allows to study the paramagnetic species in EAL over a wide *T* range, with negligible further decay during the EPR amplitude versus *T* and microwave power saturation measurements.

The superhyperfine coupling of Co(II) electron spin (S=1/2) with the nuclear spin of the nitrogen (I=1) on the DMB tail in the Cbl(II) is usually not manifested in the radical pair EPR spectra. However, in the decayed samples the $2I + 1$ split of the hyperfine lines of Co(II) are observed in the EPR line shape, and they became less pronounced with increase in *T* and % v/v DMSO. For example, at 310 mT the superhyperfine features are manifested in the EPR signal of the samples without DMSO at all *T* values measured (120-240 K), while in 2 and 4 % v/v DMSO the split is distinguishable up to 225 K and 220 K. At high filed, 369 mT, the 3 line split is not manifested at T>190 K in the EPR signal of samples with 2 and 4 % v/v DMSO conditions, but shows up to 200 K in the samples without DMSO. This dipolar interaction indicates a significant presence of uncoupled Cbl(II) in the samples. The vanishing superhyperfine features with increase in DMSO is a consequence of the low signal-to-noise ratio induced by a reaction-solvent coupling.

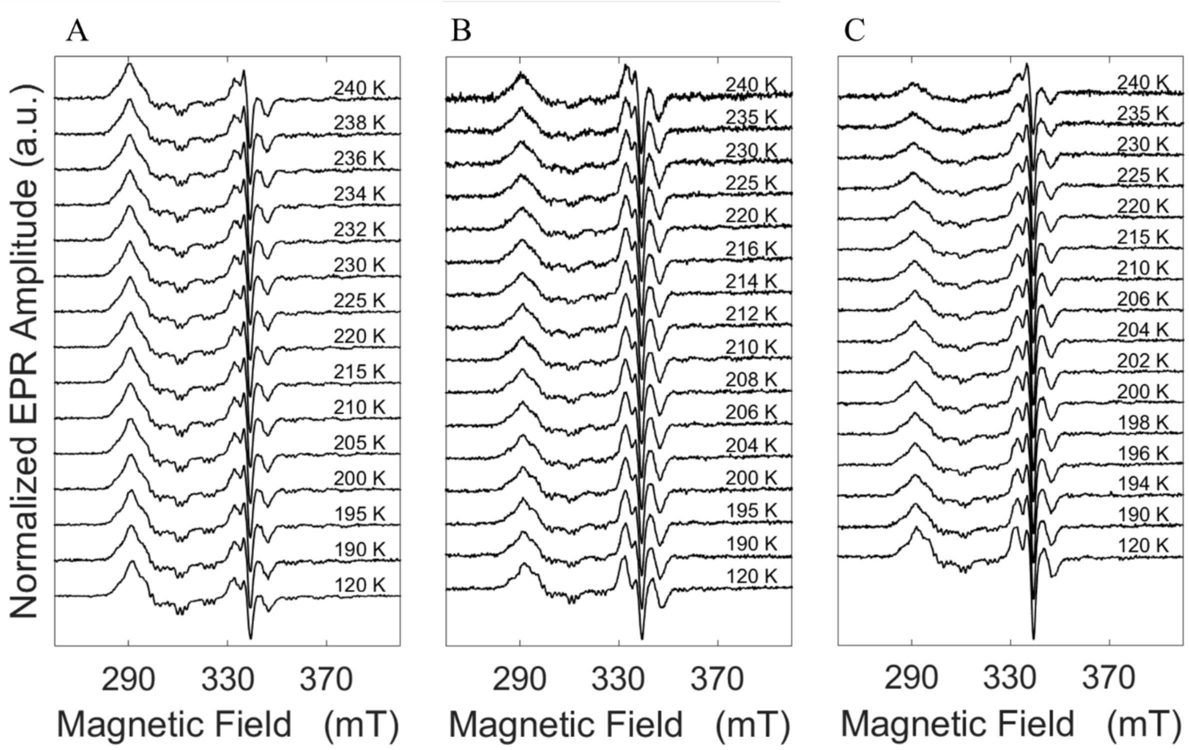

Figure 4.2. Temperature dependence of the Cbl(II)-substrate radical and uncoupled Cbl(II) + radical species spectra for the decayed cryotrapped Cbl(II)-2-aminopropanol substrate radical pair in EAL solution in the presence of different added % v/v DMSO: (A) 0 %; (B) 2 %; (C) 4 %. Spectra are normalized to the peak amplitude of the Cbl(II).

4.3.3. Temperature dependence of the EPR amplitudes of residual and terminal species in EAL after reaction with 2-aminopropanol

The *T*-dependence of the EPR amplitude over the range of the kinetic and spin probe measurements for the substrate radical in the radical pair and the uncoupled Cbl(II) and radical in the absence and presence (2 or 4 % v/v) of cryosolvent are presented in Figure 4.3. The amplitudes of all species show a general trend of a decrease with increased *T* value, which is consistent with the effect of a *T*-dependent decrease in the spin-lattice relaxation time (T_1) under the weak saturation condition and constant incident microwave power (2 mW). In addition, each species shows a kink in the dependence at the same T value. Pairs of lines fitted to the linear regions on either side of the kinks intersect at $T_{intersect}$=Δy/Δm K (Table 4.1), where dy represents the difference in the Δy intercept for each line and Δm represents the difference in the slopes. The results suggest that the T_1-relaxation processes at T values higher than the kink are enhanced. The T values of the kink and ODT are the same for both radical species measured in the 0 and 2 % v/v DMSO condition, to within the measurement uncertainties. For the 4 % v/v DMSO the correlation between the kink and ODT is maintained only for the substrate radical feature. The uncoupled Cbl(II) kink is shifted to above the ODT values.

Table 4.1. Parameters of the linear fits to the T-dependence amplitudes of the uncoupled Cbl(II) and substrate radical features at different % v/v DMSO in the regions below and above the T_{ODT}.

Radical species	**% v/v DMS0**	$T<T^{*}_{\mathrm{ODT}}$		$T>T^{*}_{\mathrm{ODT}}$		$T_{INTERSECT}$ **(K)**
		m_1	y_{01}	m_2	y_{02}	
Cbl(II)	0	-0.004	1.476	-0.009	2.522	230
	2	-0.005	1.579	-0.012	3.127	212
	4	-0.005	1.586	-0.010	2.819	214
$\mathbf{S^{\bullet}}$	0	-0.004	1.515	-0.015	4.134	232
	2	-0.005	1.639	-0.015	3.831	214
	4	-0.004	1.403	-0.014	3.501	199

T^{*}_{ODT} is represented in Figure 4.3 as vertical bars and its value is a characteristic of the % v/v DMSO present in sample solution.

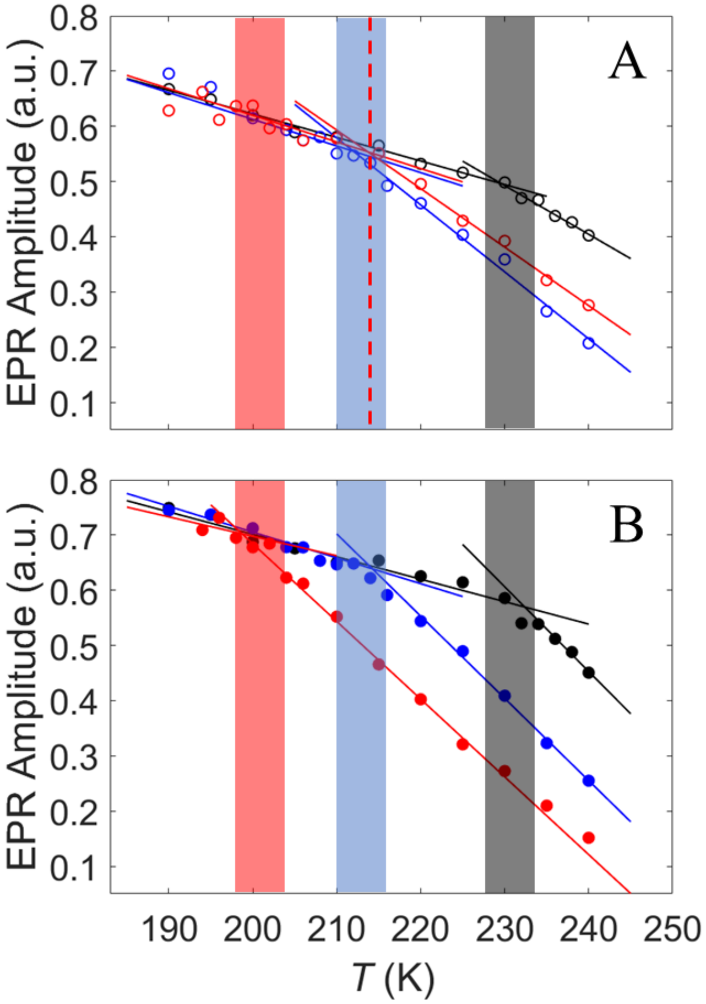

Figure 4.3. *T*-dependence of the amplitude of the uncoupled Cbl(II) (A) and substrate radical (B) features at constant microwave power and at different % v/v DMSO: 0 % (black), 2 % (blue) and 4 % (red). The uncoupled Cbl(II) feature is shown as open circles and the substrate radical feature as solid circles. The data are normalized to the amplitude at 120 K. The vertical bars represent the T_{ODT} as determined in chapter 2 and in previous work[79] for the different % v/v DMSO: 235 K for 0 % , 210 K for 2 %, and 200 K for 4 %. The 5 K width of the bars originates from the *T*-step increment in the experimental methods. The lines represent linear fits for the amplitudes in the two regions, below and above ODT temperature. The vertical dashed line indicates the intersection point of the fitted lines for the uncoupled Cbl(II) feature, determined from samples in 4 % DMSO solution, which deviates from the characteristic T_{ODT}.

4.3.4. Progressive Power Saturation

When not in the saturation regime, the intensity of the EPR signal increases linearly with the square root of the microwave power. The microwave power saturation occurs when the rate of absorption exceeds the rate at which the system returns to equilibrium, and the degree of saturation is dependent on the type of paramagnetic center, the temperature and the spin-relaxation times. In this regime, the increase in the EPR signal is not linear with increasing microwave power, but instead follows a trend that can be fit to analytical expressions to extract information of relaxation properties. [136] For the spin-spin interaction between the rapidly relaxing metal center coupled [Cbl(II)] to a slowly relaxing organic radical (substrate radical) in EAL, the method of microwave progressive power saturation is used to evaluate the relaxation mechanism. The complex relaxation behavior of the Cbl(II)-substrate radical pair leads to inhomogeneous broadening of the EPR signal and T_1 and T_2 cannot be determined. However, $P_{1/2}$ is proportional to $1/(T_1T_2)$ meaning this method allows for the observation of trends in relaxation properties through monitoring trend in $P_{1/2}$ for the different % v/v DMSO conditions.

In figure 4.4 the log ($I(P)$) versus log$P$ plot shows the saturation curves for the two paramagnets in EAL, uncoupled Cbl(II) and substrate radical in the radical pair, in the different % DMSO and T conditions. The presented data correspond to measurements for which the signal-to-noise ratio (SNR) of the EPR signal is greater than 10. The saturation data show two linear regions which intersect at $P = P_{1/2}$. The progressive saturation data for the substrate radical feature measured at 235 K in solution of 2 and 4 % DMSO display noise and the saturation curve is not well defined. Thus, the fitting results for these data present low values for R^2 (0.49 and 0.25) and this is a result of a low SNR (<10) of the measured EPR signal at power values lower than 6 mW. The values for $P_{1/2}$ obtained from the saturation equation fits are shown in Table 4.2. The increase in *T*, from 200 to 235 K, causes an increase in the $P_{1/2}$ values. At the 0 % DMSO condition the increase is larger for the substrate radical ($\Delta P_{1/2}$ = 114 mW) than for Cbl(II) ($\Delta P_{1/2}$ = 24 mW), while for 2 % DMSO condition the *T* increase has a more pronounced effect on the Cbl(II) ($\Delta P_{1/2}$ ≈ 283 mW) relaxation rate than on the substrate relaxation rate increase ($\Delta P_{1/2}$ ≈ 163 mW). Similarly, the effect of DMSO on the spin relaxation rate of Cbl(II) and substrate radical is revealed by the increase value of $P_{1/2}$. Therefore, when comparing the samples without and with 2 % v/v DMSO the half-saturation power of the substrate radical is increased by 9 mW at 200 K and 58 mW at 235 K. Moreover, uncoupled Cbl(II) shows a more pronounced effect of the DMSO with an increase in the $P_{1/2}$ by 31 mW at 200 K and 290 mW at 235 K.

Table 4.2. Progressive power saturation parameter, $P_{1/2}$, determined at 200 K and 235 K for uncoupled Cbl(II) and substrate radical, **S•**, in EAL and different % DMSO.

	$P_{1/2}$ (mW)			
% v/v DMSO	**S•**		Cbl(II)	
	200 K	235 K	200 K	235 K
0	107	221	21.6	45.6
2	116	279	53.5	336
4	109	336	26.6	138

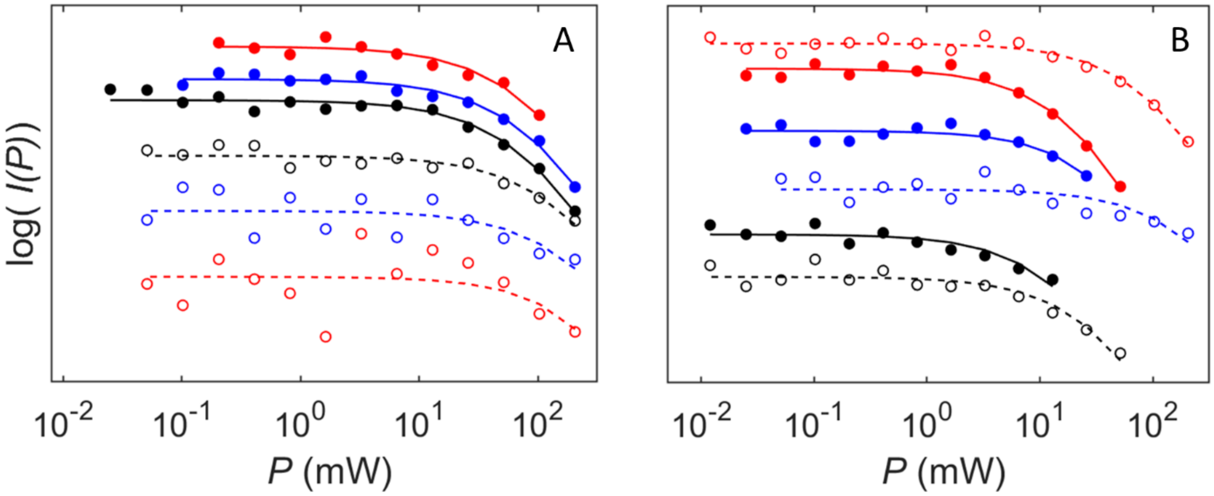

Figure 4.4. Progressive power saturation for the decayed EAL-bound paramagnets [substrate radical (A) and uncoupled Cbl(II) (B)] in reaction solution with different % v/v DMSO: 0 % (black), 2 % (blue) and 4 % (red). The Y axis, log(*I(P)*), is the log of normalized EPR amplitude divided by the square root of *P*. The data were measured at 200 K (solid circles) and 235 K (open circles), respectively. The lines (solid for 200 K and dashed for 235 K) represent fits to the respective data set using Eq 4.1.

4.4. Conclusions

The TEMPOL spin probe detects the ODT in the PAD solvent dynamics, in the presence of 10 mM (0.075 % v/v) 2-aminopropanol in the *T* interval, 230-235 K for 0 % DMSO, 210-215 K for 2 % DSMO and 200-205 K for 4 % DMSO as determined in Chapter 2, and in agreement with previous work in which only DMSO was present as cryosolvent.[79] The kink in the *T*-dependence of the EPR amplitude at 230 K for 0 % DMSO and at 214 K for 2 % DMSO falls in the *T* interval for the ODT, as determined for the spin probe method. For the 4 % v/v DMSO condition, the kinks lies just outside of [uncoupled Cbl(II)] and at the boundary (substrate radical) of the range of the ODT defined by the *T*-region of the spin probe component weight tranzition. Overall, comparison of the *T* values of the TEMPOL spin probe-detected *W* and log$\tau_{c,f}$ transitions with the *T* values of the kinks in EPR amplitude versus *T* dependence shows that they are comparable. Therefore, the events are all associated with the previously assigned ODT in the PAD.

Insight into the origin of the kinks in the *T*-dependence of the EPR amplitudes of the endogenous paramagnetic species in EAL is provided by the *T*-dependence of the EPR line shapes, and by the microwave power saturation. The EPR line shapes of the different species in Figure 4.2 are independent of *T*, which suggests that the spin-spin relaxation, T_2, does not change significantly across the kink. This is consistent with the microwave power saturation studies, which show that the *P* value of 2 mW for collection of the *T*-dependence lies well below the $P_{1/2}$ values for saturation. Therefore, contributions of T_2 and the spin-lattice relaxation time, T_1, to the kink in the *T*-dependence of the EPR signal intensity can be neglected.[137] For these non-lossy, paramagnetically dilute samples, changes in magnetic permeability and the distribution of the microwave electric field in the resonator over the examined *T*-range are also expected to be negligible.[137] Therefore, the kink in the *T*-dependence of the EPR amplitude is proposed to arise from a change in the sample dielectric properties at the ODT, that is detected in the measurement circuit, through a change in the interaction (capacitive and inductive coupling) of the microwave radiation with the sample in the EPR experiment configuration.[137, 138] This change in the dielectric properties, and specifically, the imaginary part of the complex electric permittivity (dissipative or loss component; corresponding to the microwave frequency of 9.5 GHz), ε'', influences the detection sensitivity through modification of the resonator quality factor, Q. [138] It is proposed to arise from the change in solvent freedom in the coupled mesodomain and PAD phases, that occurs at the ODT. In the direction of increasing *T*, an increase in solvent freedom (order-to-disorder) would increase ε'', and lower *Q*, which is consistent with the observed decrease in slope of the EPR amplitude versus *T* dependence, above the ODT. The *T*-dependence of the

EPR amplitude of endogenous paramagnetic species in EAL therefore provides a direct probe of the solvent dynamical behavior.

Chapter V

Preliminary Studies Towards Structural Investigation in Bacterial Microcompartment Proteins EutL and EutS by Electron Paramagnetic Resonance Spectroscopy

5.1. Introduction

Bacterial microcompartments (BMCs) are polyhedral, protein-based organelles that isolate specific metabolic processes within the cell, and can play a role in survival in inhospitable environments.[33-37] These BMCs encapsulate enzymes which form the core structure and are involved in different metabolic pathways. The encapsulation enhances the enzymatic reaction efficiency and sequesters toxic and/or volatile intermediates, enabling growth in a nutrient-depleted environment. This adaptability to low nutrient conditions enabled by BMCs affords a competitive advantage to bacterial pathogens that encode these organelles.[37] The proteins that form the shell of these organelles are hexamers or trimers of dimers and some present central pores that are thought to mediate transport of substrate, cofactors or products.[85, 86] These shell proteins are categorized into three types, BMC-H (hexamers), BMC-T (pseudohexamers) and BMC-P (pentamers).[34] The most abundant, BMC-H, is a homohexamer with a concave and a convex side that together with BMC-T, a pseudohexamer of a trimer of dimers with a central pore, form the facets of the shell. In addition, BMC-P, a pentameric protein, is suggested to form the vertices, completing the icosahedral shape of the BMCs.

Under anaerobic, nutrient-depleted conditions in the human gut, pathogenic *Escherichia coli* and *Salmonella* bacteria disrupt the epithelial layer to extract ethanolamine (EA), which is processed in the ethanolamine utilization (Eut) BMCs by the B_{12}-dependent ethanolamine ammonia-lyase (EAL) and other enzymes, and used as a carbon and nitrogen source.[13, 30, 32] Moreover, in the EA metabolic pathway acetaldehyde has been reported to be a volatile and toxic intermediate for the cells. [30] The proteins that form these Eut BMCs are encoded in a 17-gene *eut* operon and five proteins build these shells (EutS, EutK, EutM, EutL and EutN). The BMC shell proteins adopt a hexameric (EutS, EutM, EutL and EutK) or a pentameric (EutN) structure, and with the exception of EutK, they all oligomerize in solution at physiological pH.[37, 85] The EutL hexamer is formed by a trimer of dimers with two domains in its monomeric structure.(Figure 1.8 from Chapter I) Additionally, lateral interactions between identical proteins were suggested for EutM, EutL and EutS shell proteins as each crystalizes in a 2-dimensional (2D) sheet.[37] However, a 2D structure of both EutL and EutM was not successfully obtained.[37]

EutL is hypothesized to be involved in transport of substrate and cofactor [83, 91] while EutS has been shown to form shells alone.[88, 139] EutS crystal structure showed an asymmetric assembly of the monomers into a homohexamer which can be visualized as two trimers that form a concave bend with respect to each other of 40°.(Figure 1.7 from Chapter I) The homolog shell protein PduU from propanediol utilization microcompartment has a flat structure with a valine at position 39 that is not conserved for EutS, which has a glycine. The EutS mutant G39V crystallized into a flat structure indicating the importance of the glycine in the bending of the protein. The bend has been proposed to form the edges in the BMC shell structure, and its is suggested that this feature allowed to engineer BMCs in cells from EutS expression alone.[85, 88] EutL structure was solved for two conformations associated with a closed state and an open state for the EutL trimer of dimers.[83, 85] The functional protein structure shows three small pores (2.2 Å in diameter) in the closed state and a central triangular pore (11 Å and 8 Å sides) in the open state.[83] The rearrangement that shifts the conformation from closed to open induces a backbone movement of 15 Å in the two loops of each monomer that form the pores. The repositioning of the loops upon conformational change indicated structural flexibility.[89, 140] Studies that reveal the structure of the EutL protein and characterize the conformational change and assign a transport function to the pores do not explain the mechanism of opening or the mechanism of transport. How the open or closed conformations are triggered still remains an unanswered question. In addition, the mechanism of association and the spatial arrangement of the shell proteins in the BMCs is not well-characterized. Nucleation of the core enzymes is suggested to be promoted by encapsulation peptides, extensions at C- or N-terminal of the enzymes that interact with shell proteins.[88, 141] Through these interactions structural proteins are recruited around the core forming the shell. However, the Eut BMC shell proteins have not been fully characterized.

The aim of the project is to identify and structurally characterize the proposed conformational shift in EutL and to characterize the interactions that promote shell formation by EutS alone. Here we employ site directed spin labeling (SDSL) in combination with X-band, continuous wave - electron paramagnetic resonance (CW-EPR) spectroscopy in an attempt to characterize Eut shell proteins and the assembly mechanism and structure of the BMC. An *E. coli* overexpression system for the *Salmonella Enterica* LT2 EutS and EutL proteins has been created, and the proteins have been isolated. EutS protein alone can form BMC shells in *E. coli*, and our preliminary results confirm its propensity to form higher-molecular mass entities. The reorientation correlation times and component amplitudes, and electron spin-spin interactions of sulfhydryl-specific spin labels, at the single cysteine (Cys, C) site on EutS and EutL have the potential to reveal site-specific dynamics and inter-protein distances, that can be used to generate models for the structure of EutS BMCs as well as models for structure and dynamics involved in the EutL conformational change. SDSL CW-EPR is highly sensitive to the distance between the labeling residues, with a distance-dependence of $1/r^3$, where r is the distance between the electron spins.[97, 142-144] An understanding of the shell structure and assembly mechanism of EutS BMCs, and transport properties for EutL, will provide a path to new drug targets, and information applicable for nano-bioreactor engineering. [139, 145-147]

5.2. Materials and methods

5.2.1. Protein cloning and expression

EutS and EutL protein genes were cloned from the genomic DNA of *Salmonella enterica serovar Typhimurium* LT2 (ATCC® 700720™). The dried genomic DNA was rehydrated before use in 1 ml deionized water (resistivity, 18.2 MΩ·cm; Nanopure system, Siemens).

The pET-22b expression vector from Millipore () was used. This vector is ampicillin resistant and incorporates a noncleavable His6 tag at the C-terminal of the expressed proteins. Restriction sites NdeI (CAT ATG) and XhoI (CTC GAG) were used to insert the DNA fragment. The plasmid was transformed into TOP10 Chemically Competent *E. coli* (Invitrogen, Life Technologies) for storage and further use. For protein overexpression system, the *E. coli* BL21 (DE3, ThermoFisher) was used.

Genes of interest (*eutS* and *eutL*) were amplified from the genomic DNA by PCR using specific gene primers (Integrated DNA Technologies): *eutS*_FWD – GGG **CAT ATG** GAG ACG GTG AGC AAT GAA TAA AGA ACG, *eutS*_Rev – GGG G**CT CGA G**AC TTT TTG TTA ACT CAC ACA GGG TAA AGT TTA, *eutL*_FWD – **CAT ATG** AGG AGA CAT CAT GCC TGC ATT AGA, and *eutL*_Rev – **CTC GAG** CGC ACG CTG GAC AGG GTT ACG. The PCR product was purified from 1.5 % agarose Tris-Acetate-EDTA gels by using the illustra GFX PCR DNA and Gel Band Purification kit (GE Healthcare, Life Sciences). The nucleotides presented in bold at the 5’ end of the forward and reverse indicated primers encode the restriction sites for the enzymes NdeI and XhoI (Millipore) which in the digestion process create sticky ends in the PCR DNA products. A T4 DNA ligase inserts the DNA fragments into the digested pET-22b. All constructs were verified via DNA sequencing (GeneWiz) and plasmids with 100% sequence purified plasmids were further transferred into BL21 cells, and 50% glycerol stocks of TOP10 and BL21 cells were stored at -80° C.

For protein expression, cells from glycerol stocks were plated on Luria Bertani (LB) Agar (EMD Millipore, Merck kGaA) plates with 50 mg/ml ampicillin (Sigma-Aldrich). Cells were inoculated in 1 L LB broth (EMD Millipore, Merck kGaA) with 50 mg/ml ampicillin from an overnight LB culture of BL21 colony from plate and were grown at 37° C while shaking at 225 rpm. When the OD_{600} reached 0.7, protein overexpression was induced by adding 0.8 mM of isopropylβ-d-1-thiogalactopyranoside (IPTG, TEKnova) while shaking at 225 rpm and 30° C. EutS expression was induced for 4 h, while EutL required overnight expression.

5.2.2. Site directed mutagenesis

Site-directed mutagenesis (SDM) was carried out by using the Q5 High-Fidelity 2X Master Mix site-directed mutagenesis kit (New England BioLabs) according to manufacturer instructions. Mutations in the *eutS* and *eutL* genes targeted amino acids substitutions in the EutS (Gly 39 for Val) and EutL (Ala at position 73 for Cys, Cys at position 201 for Ser) proteins. The plasmids containing the DNA inserts of the wild type (WT) proteins were used as template for the respective primers that contain the substitution. The oligonucleotide primers were designed using the Agilent Technologies primer design tool and NEB for T_m calculator: EutS-G39V_FWD – CCC GAT GCT GTC GCG ATT GGC, EutS-G39V_Rev – AAC GCC GAT CTT TTT CGC, EutL-A73C_FWD – CTA TGC CGG GTG CGC TCA CGG, EutL-A73C_Rev – AGG GAG CGG CCA TAG ACC, EutL-C201S_FWD – GTA AAG CCG CCT CCA ACG, and EutL-C201S_Rev – ACG CGG CCT GGC TTC. A73C was achieved through a codon change (gcg->tgc), while a nucleotide was changed in the codon for C201S (tgc->tcc) and G39V (ggc->gtc). Double mutant for EutL A73C C201S protein was constructed from the plasmid containing the EutL A73C mutation as template for the primers with C201S mutation. The sequence for all mutant plasmids were verified via gene sequencing and plasmids containing the correct constructs were then transformed intoTOP10 and BL21 (DE3) cells. Protein overexpression was induced in BL21 cells by using IPTG and same procedure steps as their respective WT.

5.2.3. Protein purification

The cultures expressing the desired proteins (1-1.5 L culture) were centrifuged for 30 min at 5000 rpm and 4° C by using a RC5C centrifuge (Sorvall Instruments) with a GSA rotor, and the supernatant was discarded. The protein EutS and EutL extraction was reported previously by either French press or cell lysis.[83, 148-150] Here the pellet was homogenized at room temperature for 30 min by stirring in 20 ml buffer (20 mM Tris, 300 mM NaCl) at pH 8 mixed with 1 mM phenylmethylsulfonyl fluoride (PMSF, Sigma-Aldrich), 10 mg/20 ml lysozyme (Sigma-Aldrich), 2 mM mercaptoethanol (BME, Sigma-Aldrich). The supernatant was collected after 15 min centrifugation at 12000 rpm using the SS34 rotor, and run on a gravity nickel-nitrilotriacetic acid (Ni-NTA) agarose (Qiagen) column for purification. The Ni-NTA agarose resin is a chromatography matrix with four Ni ions bound to NTA. The hexahistidine tag or imidazole have high affinity for Ni. Thus, in the purification process low concentrations of imidazole in the buffers avoid binding of host cell proteins allowing for only the recombinant proteins to bind, while high imidazole concentrations elute the purified protein. The purification procedure includes three steps: sample loading (supernatant containing the overexpressed protein of interest); binding of the His-tag protein to the column; and washing the His-tag protein out of the column. Previous to sample loading, the column was washed with buffer to clean the storage solution (water/ethanol). For the binding step a buffer (20 mM Tris, 300 mM NaCl, 2 mM BME, pH 8; 50 ml for a 3 ml resin column) with low imidazole concentration (10 mM imidazole) was used, while for the washing step a 300 mM imidazole buffer was used. The washed (eluted) protein sample was dialyzed overnight at 4° C in 3.5 K dialysis cassettes (Slide-A-Lyser, Thermo Scientific) or 6 K membrane dialysis tubing (Thermo Scientific) against 1 L buffer (20 mM Tris, 100 mM NaCl, pH 8) with two buffer changes. In addition, if protein concentration was needed, after dialysis the sample was incubated in aquacide up to 5h.

5.2.4. Fast protein liquid chromatography (FPLC)

Protein purification and separation of oligomer compounds were performed by using a fast protein liquid chromatography (FPLC, AKTA GE Healthcare) and Superdex 200 Increase 10/300 GL (GE Healthcare, Life Sciences) column. The size exclusion chromatography column provides high-resolution analysis for biomolecules with molecular weights in the range 10 – 600 kDa. Volumes of 1-2 ml of purified protein were injected into the column preequilibrated with buffer (20 mM Tris, 300 mM NaCl, pH 8) and run at a flow rate of 0.5 ml/min while monitoring the absorbance at 280 nm of the eluted solution. The column was calibrated in buffer at a flow rate of 0.5 ml/min. (Figure E.10 in Appendix E)

5.2.5. SDS and native PAGE

Sodium dodecyl sulphate (SDS) and native polyacrylamide gel electrophoresis (PAGE) was carried out for denatured and native protein samples by using a 12 % and 10 % Mini-PROTEAN TGX (Tris-Glycine eXtended) Precast Protein Gels (Bio-Rad Laboratories). For SDS PAGE protein aliquots were denatured by incubation at 99° C for 20 min after 1:1 mixing with 4x Laemmli Sample Buffer (Bio-Rad Laboratories). After running the probes on the SDS gel in 1xTG SDS buffer (Bio-Rad Laboratories), the bands were fixed in solution of 40 % methanol, 10 % acetic acid and 50 % water, for 30 min, then stained in Coomassie Brilliant Blue dye (Bio-Rad

Laboratories) for 1-2 h and destained overnight. Native PAGE was carried on the non-denatured protein samples following the same steps, but in the absence of SDS in the running buffer, loading sample buffer and gels.

5.2.6. SDSL

SDSL is a technique where a stable free radical is chemically tethered to a defined site in a biomacromolecule.[94, 142, 151, 152] The labeling occurs through covalent bonding to the sulfhydryl group of Cys residues. Among the spin labels available for these studies, the maleimido-nitroxide, 4MT, is used.

Simulations of the spin label configurations at Cys residues. MMM (www.epr.ethz.ch/software/index) is a Matlab program that allows modeling of macromolecular systems or manipulating the existent macromolecular assemblies using Protein Data Base (PDB) files. The program describes the configurational mobility of the spin labels through rotamers, which are alternative conformations of the label within the protein. MMM currently supports rotameric libraries for only two spin labels, methanethiosulfonate (MTSL) and iodoacetamido-PROXYL (IA-PROXYL). The rotamer predictions take into consideration the spin label internal energy and the interaction energy with the protein at 175 K, providing a good estimate of its position without clashes with atoms or residues within the protein. PDB files of the EutS and EutL BMCs together with MMM were used to model spin labels at desired sites in the proteins. Specifically, the MTSL spin label was modeled into the protein structure at the desired sites using the rotamer library approach. MTSL was chosen over IA-PROXYL due to its flexibility and specificity. Although the choice was limited for modeling the configurational mobility of the label, the experiments were done using 4MT spin label which is a stable thioether bond with irreversible reaction. Possible rotamers at the selected sites in the proteins are shown in Figures E.5- E.7 of Appendix E.

PyMol, which is a program for visualization and manipulation of molecular structures[153], was used to construct the EutS hexamer and EutL trimer from the PDB files available. The PDB library gives access to crystal structures of different EutS and EutL homologs, available in each of the conformations, bent and flat (EutS), open and closed (EutL). The *E. coli* EutS and EutL PDB structures were used for these studies.[85] In PyMol, the mutagenesis function allowed substituting amino acids at desired positions in the PDB structure files. With this substitution in our protein sequence the new file was used in the MMM program to simulate the rotamers for the MTSL. This approach was applied to EutL in both open and closed conformation files, 3i87.pdb and 3i82.pdb. The EutS PDB file 3i96.pdb was used without changes in the MMM program. MMM together with PyMol were used for visualization of the rotamers at the desired positions, and for determination of approximate distances and orientations between nitroxides in each protein. The distances can be then translated to interactions between the spin labels which together with orientations, the electron-electron spin-spin coupling matrices and their orientation in the tensor frame described by Euler angles are defined to simulate EPR spectra expected in the SDSL CW-EPR spectroscopy expriments.

Labeling procedure. Purified WT EutS constructs were mixed in 1:1 ratio with 4MT spin label nitroxide at room temperature under aerobic conditions in buffer of 20 mM tris, 100 mM NaCl, pH 8. Samples without and with 2 M urea were prepared. For sonicated samples, prior to adding the other components, EutS protein (120 μM) was subjected to 3 rounds of sonication on ice bath for 10 s with 30 s incubation on ice. The sonication was used to promote unfolding of the studied protein and asses the accessibility of the Cys residue for labeling. The samples had a total volume of 200 μl and were loaded in 2 mm outer diameter EPR tubes (Wilmad-LabGlass, Vineland, NJ).

Purified samples of WT EutL and single and double mutants (A73C and C201S) of EutL were used to make 120 μM labeled protein samples. The protein was incubated with 1 and 10-fold molar ratio of 4MT for 2 h at room temperature. Samples with 1 M $ZnCl_2$ were prepared and 1 min incubation time was allowed prior to adding 4MT. The labeled probes were then dialyzed in buffer (20 mM tris, 100 mM NaCl, pH 8) for 4 h by using dialyzers (3.5 MWCO 0.5 ml, Thermo Scientific), with buffer change every hour, in order to eliminate the excess/unbound 4MT and Zn^{2+} when used. Three control samples were used and they consisted of protein, protein and Zn^{2+} and 4MT alone. Samples with a total volume of 300 μl were loaded into 4 mm outer diameter EPR tubes and frozen by rapidly submerging in liquid nitrogen isopentane pre-cooled to 140 K.

5.2.7. CW-EPR spectroscopy

The CW-EPR spectra were collected by using a Bruker E500 ElexSys EPR spectrometer equipped with a Bruker ER4122 SHQE X-band cavity resonator. Room temperature (294 K) and 120 K EPR spectroscopy experiments were carried out for EutS and EutL labeled samples. The 120 K temperature (*T*) was achieved by using a Bruker ER4131VT temperature controller and cooling system that consists of a nitrogen gas flow through a coil immersed in liquid nitrogen bath contained in a 4 L dewar. The EPR acquisition parameters used for EutS experiments at 294 K were: 9.45 GHz microwave frequency; 0.2 mW microwave power; 2 Gauss magnetic field modulation; 100 kHz modulation frequency; 3300-3440 Gauss sweep width; 1024 points and 16 averaged spectra. EPR acquisition parameters for EutL experiments at 120 K were: : 9.45 GHz microwave frequency; 0.2 mW microwave power; 2 Gauss magnetic field modulation; 100 kHz modulation frequency; 3280-3460 Gauss sweep width; 1024 points and 16 averaged spectra.

5.2.8. CW-EPR simulations

The CW-EPR signal of interacting spin labels was simulated using the Pepper algorithm in the EasySpin program (http://www.easyspin.org/). [122] The parameters for the simulations were taken from the modeled structures in PyMOL. A system with three or six pairs of electron spins and nuclear spins were defined according to specifications. Each of the electron spin systems was described by a set of g tensor ($g_x = 2.0120$, $g_y = 2.0130$, $g_z = 2.0073$) and axial ^{14}N hyperfine tensor parameters ($A_x = A_y = 20.2$, $Az = 103.2$ MHz), isotropic dipolar coupling tensor and its orientations calculated from the PyMOL determinations of the distances and Euler angles.

5.3. Results and Discussion

5.3.1. Structure and sequence analysis to identify SDSL sites

EutS and EutL proteins from *E. coli* were crystallized and their structures have been solved.[83, 85] The homolog proteins from *E. coli* and *S. typhimurium* present 95 % and 97 % sequence identity. (Figure 5.1)

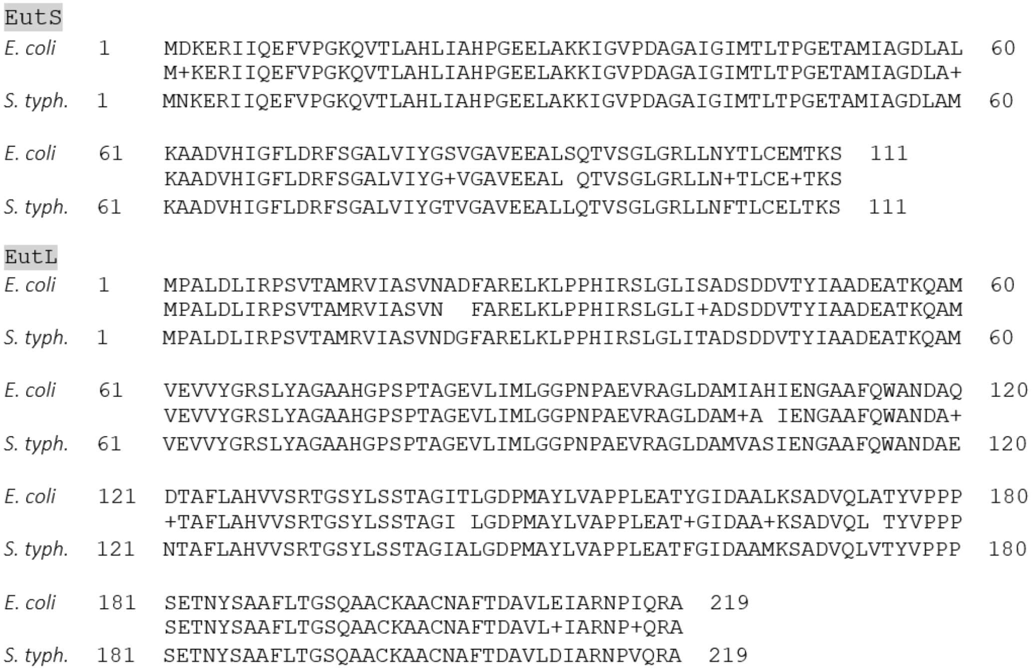

```
EutS
E. coli   1    MDKERIIQEFVPGKQVTLAHLIAHPGEELAKKIGVPDAGAIGIMTLTPGETAMIAGDLAL  60
               M+KERIIQEFVPGKQVTLAHLIAHPGEELAKKIGVPDAGAIGIMTLTPGETAMIAGDLA+
S. typh.  1    MNKERIIQEFVPGKQVTLAHLIAHPGEELAKKIGVPDAGAIGIMTLTPGETAMIAGDLAM  60

E. coli   61   KAADVHIGFLDRFSGALVIYGSVGAVEEALSQTVSGLGRLLNYTLCEMTKS  111
               KAADVHIGFLDRFSGALVIYG+VGAVEEAL QTVSGLGRLLN+TLCE+TKS
S. typh.  61   KAADVHIGFLDRFSGALVIYGTVGAVEEALLQTVSGLGRLLNFTLCELTKS  111

EutL
E. coli   1    MPALDLIRPSVTAMRVIASVNADFARELKLPPHIRSLGLISADSDDVTYIAADEATKQAM  60
               MPALDLIRPSVTAMRVIASVN  FARELKLPPHIRSLGLI+ADSDDVTYIAADEATKQAM
S. typh.  1    MPALDLIRPSVTAMRVIASVNDGFARELKLPPHIRSLGLITADSDDVTYIAADEATKQAM  60

E. coli   61   VEVVYGRSLYAGAAHGPSPTAGEVLIMLGGPNPAEVRAGLDAMIAHIENGAAFQWANDAQ  120
               VEVVYGRSLYAGAAHGPSPTAGEVLIMLGGPNPAEVRAGLDAM+A IENGAAFQWANDA+
S. typh.  61   VEVVYGRSLYAGAAHGPSPTAGEVLIMLGGPNPAEVRAGLDAMVASIENGAAFQWANDAE  120

E. coli   121  DTAFLAHVVSRTGSYLSSTAGITLGDPMAYLVAPPLEATYGIDAALKSADVQLATYVPPP  180
               +TAFLAHVVSRTGSYLSSTAGI LGDPMAYLVAPPLEAT+GIDAA+KSADVQL TYVPPP
S. typh.  121  NTAFLAHVVSRTGSYLSSTAGIALGDPMAYLVAPPLEATFGIDAAMKSADVQLVTYVPPP  180

E. coli   181  SETNYSAAFLTGSQAACKAACNAFTDAVLEIARNPIQRA  219
               SETNYSAAFLTGSQAACKAACNAFTDAVL+IARNP+QRA
S. typh.  181  SETNYSAAFLTGSQAACKAACNAFTDAVLDIARNPVQRA  219
```

Figure 5.1. Sequence alignment of amino acids for EutS and EutL proteins from *E. coli* and *S. typhimurium*. The alignment was done using the NCBI tool (BLAST).[154]

Homology model using a protein molecular modeling server Geno3D (http://geno3d-pbil.ibcp.fr) was done for both EutS and EutL proteins from *S. typhimurium*. [155] A comparison of the model to the *E. coli* structures is described in the Appendix E. (Figure E.1 and Table E.1) Based on the results and the high residue conservation, the PDB structures were used for closed (3I82) and open (3I87) conformations of EutL and, bend (3I96) and flat (3IAO) structures of EutS. The structures were manipulated in PyMOL, where the fully functional quaternary structures of the proteins were constructed. The conformations were analyzed to determine the approximate orientations and distances between residues and attached nitroxides.

To analyze the structure, dynamics and assembly mechanism of the EutS and EutL proteins by using SDSL, solvent accessible cysteines are needed to react and cross-link the maleimido-nitroxide label. The *S. typhimurium* EutS presents one Cys per monomer at position 106 and EutL has two Cys residues at position 197 and 201. In many cases the presence of more than one Cys residue in a protein may lead to formation of a disulfide bond which is known to have a functional role in stabilizing the folded structure of proteins.[156] In particular, the crystal structures of EutL from *Clostridium perfringens* have indicated the presence of three Cys residues from which two are involved in a disulfide bond (C127 and C200) suggested to play an important role in opening and closing of the pore.[157] If this is the also the case for the wild type Cys residues of our EutL, they cannot be considered as labeling sites. However, the Cys triad is absent among other EutL orthologs (homologous gene sequence found in different species) and the C127 involved in this particular case in the disulfide bond is not conserved. In order to better asses the structural importance of the Cys residues in our protein, a search through different pathogenic strains of *E. coli*, *Salmonella*, *Clostridium tetani*, *Mycobacterium*, *Klebsiella* and *Enterococcus* indicated the absence of the disulfide bond and thus the possibility of using the wild type Cys as labeling sites. (Figure E.2 in Appendix E)

These EutS and EutL corresponding Cys residues were analyzed for SDSL labeling. Surface accessibility of the residues was evaluated in PyMOL and by using the Protein Data Bank in Europe Proteins, Interfaces, Structures and Assemblies (PDBePISA) web server.[158] The analysis indicated an accessible surface area for EutS C106 of 31 Å^2 for WT and 29 Å^2 for the G39V mutant. For EutL, PDBePISA evaluated no accessible surface area for C197 while C201 has a 1.8 Å^2 accessible surface area for both open and closed conformations.

Solvent accessibility of Cys residues was also evaluated experimentally by using Ellman's test on purified EutS and EutL protein samples. The test uses 5,5'-Disulfanediylbis(2-nitrobenzoic acid) (DTNB) whose thiols react with the accessible Cys. The cleavage of the disulfide bond gives a 2-nitro-5-thiobenzoate (TNB^-) which in water ionizes to TNB^{2-} and gives an absorbance at 412 nm (ε=14150 $M^{-1}cm^{-1}$). A calibration curve was constructed using cysteine as indicated previously.[159] (Figure E.3 in Appendix E) The test associates concentrations of TNB^{2-} with the concentration of accessible Cys. For EutS the results indicated low concentrations of accessible Cys compared to concentrations of protein. Similarly, Ellman's test for EutL WT indicated an accessible concentration of Cys on the order of nM, compared to μM range of protein concentrations. Concentration of protein was most accurately determined by absorption at 280 nm where the molar extinction coefficients for EutS and EutL are 1490 M^{-1} $cm^{-1}$and 15930 M^{-1} cm^{-1}, respectively.(https://web.expasy.org/protparam/) Unreproducible EutS concentration measurements did not allow proper evaluation of the C106 accessibility for SDSL, whereas EutL concentrations assays were reproducible. This is most likely caused by the low number of aromatic residues present in EutS (1 tyrosine) compared to EutL (7 tyrosine and 1 tryptophan) which give absorption in the range 230 – 300 nm. However, the EutS C106 was considered and used for further labeling.

In addition, for EutL, analysis of surface solvent exposure of C201 done by PDBePISA and experiments suggested low solvent accessibility. Moreover, this Cys residue does not exhibit any movement upon conformational shift from closed to open.(Figure 5.2) Thus, SDSL of this residue would not provide information on the structural and dynamical changes of the protein upon conformation shift. As a result, the site is not of interest in labeling and to avoid the likelihood of attaching a nitroxide at this position, C201 was subjected to substitution with a serine to conserve the hydrophobicity.

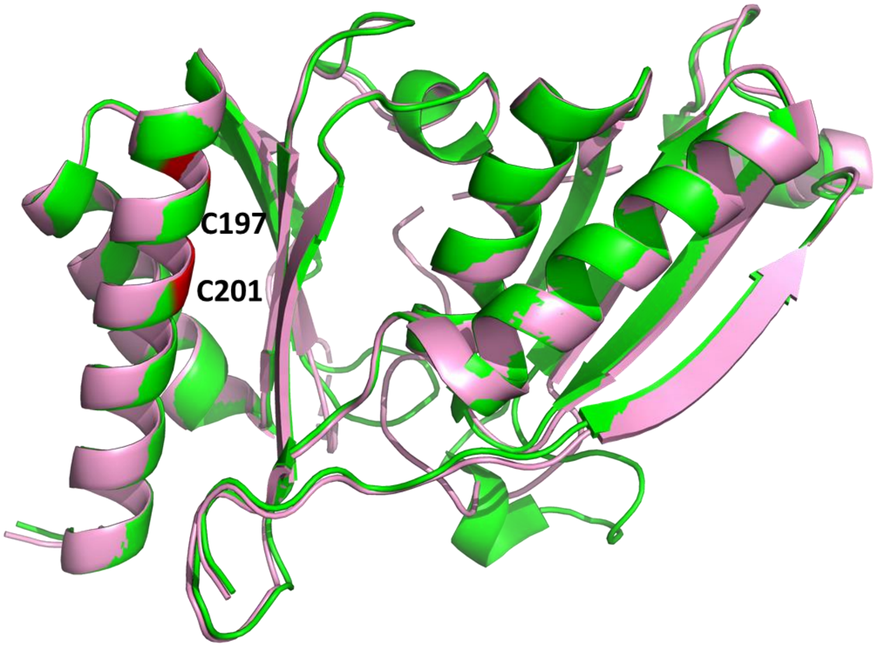

Figure 5.2. EutL monomers in closed (green) and open (light pink) conformations overlapped (PyMol capture). The Cys residues are highlighted in red and show negligible movement between the two conformations (0.4 Å displacement).

So far, the analysis for EutL wild type Cys residues indicated that none of the two could be considered for SDSL. Therefore, to analyze the structure and dynamics of EutL by using SDSL, an engineered cysteine was needed. The choice of a site was done by analyzing the changes in residue positions between open and closed conformations. The alignment of the open and closed conformations of the EutL protein in PyMOL gave a RMSD of 0.603 Å, with a more unstructured form in the pore region for the open state of the protein. (Figure 5.3, and Figure E.9 in Appendix E) The backbone movement of 15 Å in the loops from each monomer that participate in the formation of the pores in the closed conformation and the large pore in the open conformation happens as follows: the loop between β3-β4 in domain 2 exhibits a movement that repositions Thr183 at 6.7 Å and Glu182 at 10.1 Å distance, yielding a path for the loop between β3-β4 in domain 1 to reposition within the two domains, occluding now the small pores and structuring the large central pore. (Figure 5.3 and Figure 1.8 of Chapter I) The loop in domain 1 rearranges, exhibiting amino acid movements from Ala71 to Val84 that ranges between 4.2 Å for Glu83 to 16.4 Å for Ala71. (Table 5.1) All residues in this region are conserved between *E. coli* and *S. typhimurium.*

Table 5.1. Solvent accessible surface area of residues that reposition, revealing movement upon conformational change between open and closed states of EutL.

Residue	**Accessible Surface Area of EutL (Å^2)**	
	Open conformation	Closed conformation
A71	12.4*	92.8
G72	0.12*	83.1
A73	35.1	5.7*
A74	2*	33.2*
H75	55.9*	25
G76	7.7*	3.5
P77	84.5*	19.4
S78	36.9*	16.7
P79	42.9*	122.9
T80	66.3*	8.5*
A81	19.3*	28.3*
G82	5.27	31.9*
E83	21.5	97.9*
V84	1.2*	13.2*

* Interfacing residues between monomers.

Candidates for the site directed mutagenesis (SDM) were selected after an analysis of the structure, interface involvement within the EutL trimer, and possible hydrogen/disulphide bond, salt bridge or covalent link formation between residues in both conformational states by using PDBePISA and PyMol. (Table 5.1, and Table E.2 in Appendix E) Among all amino acids, alanine (Ala, A) presents a nonpolar, non-reactive aliphatic side group with no major contribution to protein conformation and thus rarely involved in protein function. Thus, Ala is a favorable choice for cysteine SDM and A73 shows accessibility when the protein is in the functional form (trimer).

Thus, to assess the conformational change, the mutant EutL A73C C201S will be used. There will be three spin labels per BMC, each with an unpaired electron.

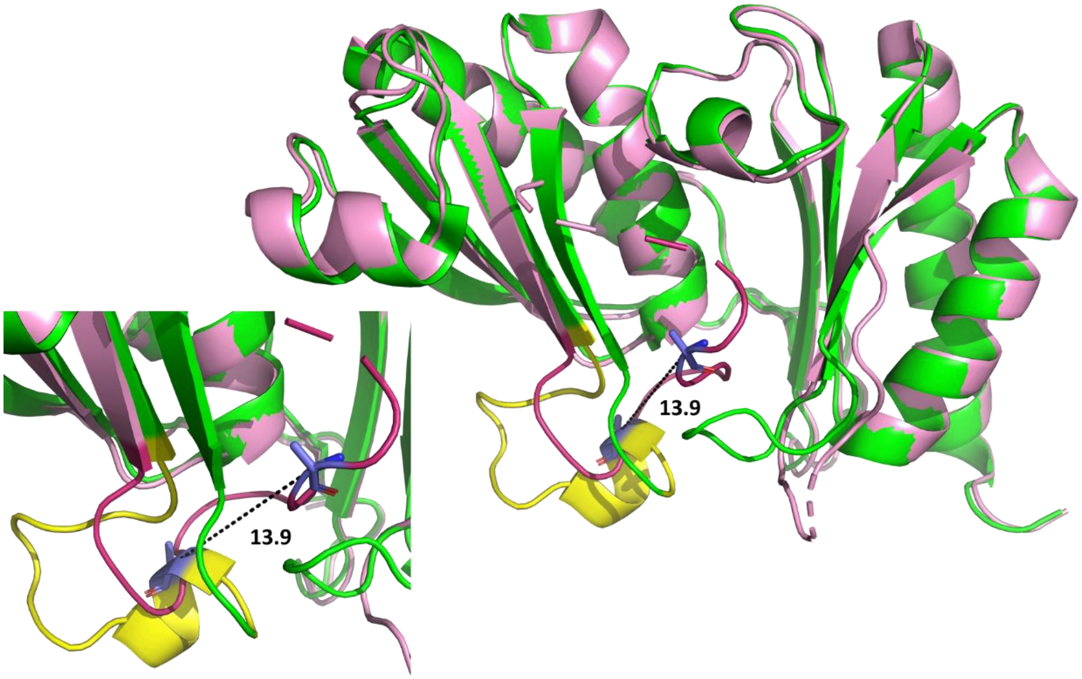

Figure 5.3. Overlap of the closed (green) and open (light pink) conformations of EutL that shows the rearrangement in the loop of domain 1. The region is highlighted by yellow for closed form and dark pink for open form. The insert on the lower left shows the enlarged region of the loop with the movement distance for A73 residue between the two conformations.

5.3.2. Purified Protein oligomers

EutS monomer has a molecular weight (MW) of 11.6 kDa while the homohexameric protein has a MW of 70 kDa. In EutL the two domains that form the monomer have a MW of 22.7 kDa and form a trimer of MW of 68 kDa. SDS gels of the purified systems showed associated bands for EutS and EutL monomers at corresponding masses. (Figure 5.4 left side) The observation is consistent with the expected MW increase of about 1.2 kDa per monomer introduced by the 6 His tag.

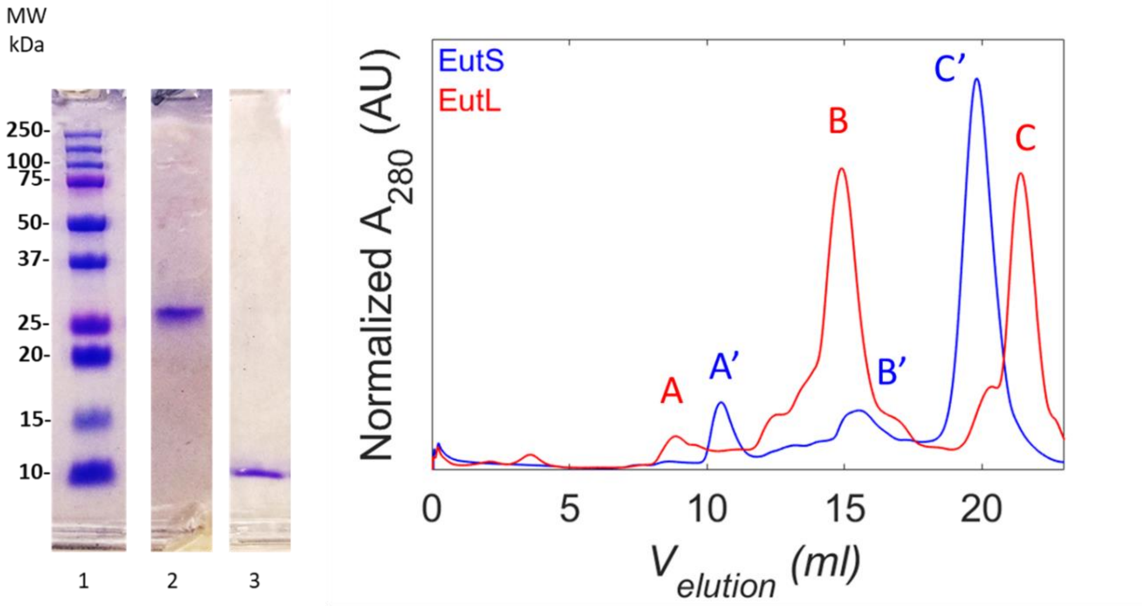

Figure 5.4. SDS PAGE and gel filtration on Superdex 200 of purified proteins. Left image shows the SDS gel (denaturing gel image) where lane (1) has the molecular mass ladder; (2) has the EutL purified protein; and (3) has the EutS purified protein. The ladder lane has the MW indicated for each band. The bands are characteristic for monomers. Right image shows the retention profiles for the oligomeric structures of the proteins: EutS (blue) and EutL (red). The absorbance was normalized to the highest peak of EutS. The peaks A and B correspond to oligomers with MW of ~1700 kDa and ~72 kDa formed by EutL monomers; while A' and B' retention peaks correspond to oligomers with MW of ~700 kDa and ~55 kDa formed by EutS monomers. The far-right peaks in the retention profiles for EutS (C', 6 kDa) and EutL (C, 3 kDa) corresponds to the aquacade and BME.

EutS and EutL proteins are expressed with a 6 His tag at the C-terminal which allow the proteins to be selectively purified from the lysate. Purification is performed by using Ni-NTA gravity column together with Superdex 200 column used on a FPLC system. Purified protein samples run on the Superdex 200 after His tag purification are shown in Figure 5.4, right panel. The 6 His tag per monomer is increasing the total mass by 7.2 kDa for EutS (hexamer, 1.2 kDa x 6) and by 3.6 kDa for EutL (trimer, 1.2 kDa x 3). Purified EutS protein show retention times that are covered between labeled peaks A’ and B’, associated with MW in the range 700-55 kDa. The broad range of MW indicates existence of different sizes oligomers in sample solutions, with the low-end region representing oligomers formed from at least 4 EutL monomers. (left of Figure E.11 in Appendix E) Similarly, EutL protein shows a pronounced peak (B) at retention volumes in the region of the trimer (~ 72 kDa) and a much smaller peak (A) for higher order oligomers (~ 1700 kDa). (right of Figure E.11 in Appendix E) Because the amplitude of the absorption peaks is proportional to the concentration of the oligomer eluted Figures 5. 4 and E. 11 indicates that EutL is mostly forming trimers. Previous studies have reported that EutS and EutL form sheets/tiles and EutS can also form BMCs alone. [37] The higher MW oligomers indicated by peak A for EutL (~1700 kDa) and A’ for EutS (700 kDa) can be associated with sheet formation. Circular dichroism and dynamic light scattering measurements on purified samples of EutS and EutL indicated the presence of alpha-helices and beta-sheets, and sizes of the particles of 2.6 – 5.7 μm which suggest that the large oligomers are folded. Both purified protein samples presented aggregates in solution and the dynamic light scattering experiments identified that soluble and insoluble particles were present. Centrifugation separated the soluble protein in the supernatant.

5.3.3. Predicted nitroxide rotamers at Cys residues in EutL and EutS

MTSL rotamer available in the MMM data base was modeled at the C106 sites in EutS protein and at A73C sites in EutL protein. This will provide a label per monomer with a total of 6 and 3 labels per EutS and EutL BMC protein. The MTSL was used because MMM does not provide rotamer libraries for 4MT. Predictions for the most probable rotamers allowed for visualization of the labeling sites in PyMOL. Compared to 4MT nitroxide, MTSL is les bulkier and therefore it has more flexibility which will give more possible orientations at the active site modelled by MMM. (Figure E.4 in Appendix E) However five possible rotations are allowed for

MTSL, when attached only two bonds are mobile,[151] while 4MT has four rotatable bonds but considered rigid with limited mobility when attached. Thus, it is expected that MTSL provides more orientations than 4MT would have and the selection of the rotamers that will be used in the analysis should be carefully done. Distances and orientations were determined for selected rotamers and used to calculate the dipolar coupling matrix that describe the interactions between the spin labels. The interaction strength is a measure of positions between labels and in consequence between the respective labeled monomers. Therefore, simulations of the EPR experiments quantify the dipolar coupling between the attached spins and characterize the conformational structure of the BMC proteins and of their assembly to form sheets.

Using the structural model for the MTSL labeling given by the MMM program, different rotamers were chosen for EutS C106 and EutL A73C. (Figure E.5 and E.6 in Appendix E) WT EutS whose structure presents a bend gave two different sets of rotamer populations for the monomers: four monomers from the hexameric protein had two possible rotameric states of the MTSL at their C106 while the other two monomers that occupy opposite positions in the EutS presented about 20 possible orientations of the MTSL. The leading rotamers with the higher probability were R80 for the four monomers and R84 for the other two monomers. (Figure 5.5 A) EutS G39V, which is in the flat conformation of the protein, had only one or three rotameric states at the C106 position and R36 was the most probable rotamer. (Figure 5.5 B) For EutL open and closed conformations the rotamer libraries gave 27 possible states at each A73C position, and the most probable ones were R124 for the closed conformation (Figure 5.5 C) and R34 for the open conformation (Figure 5.5 D). In consequence, distances between nitroxide groups of EutL A73C within the protein (between neighboring monomers) differ from closed to open by 3.1 Å, resolution, which is a difference that can be resolved by CW-EPR. (Figure 5. 5 and Table 5. 2) For

EutS WT and G39V protein structures, the distances between nitroxide labels are shown in Figure 5.5, panels A and B. The distances between nitroxide labels on adjacent EutL BMCs that group to form tiles have values for which the dipolar interaction becomes unresolved in the CW-EPR spectrum. Similarly, in the WT EutS BMC tiles the distances between the nitroxide labels on neighboring hexamers are larger than 25 Å, the limit of electron-electron dipolar interactions by CW-EPR. However, the flat EutS structures controlled by mutation G39V have intermolecular distances for which the electron dipole-dipole interaction can be detected. The ability to distinguish between the two conformation can be used to gain information on the conformational structure in tile arrangement for EutS. (Figure 5.6)

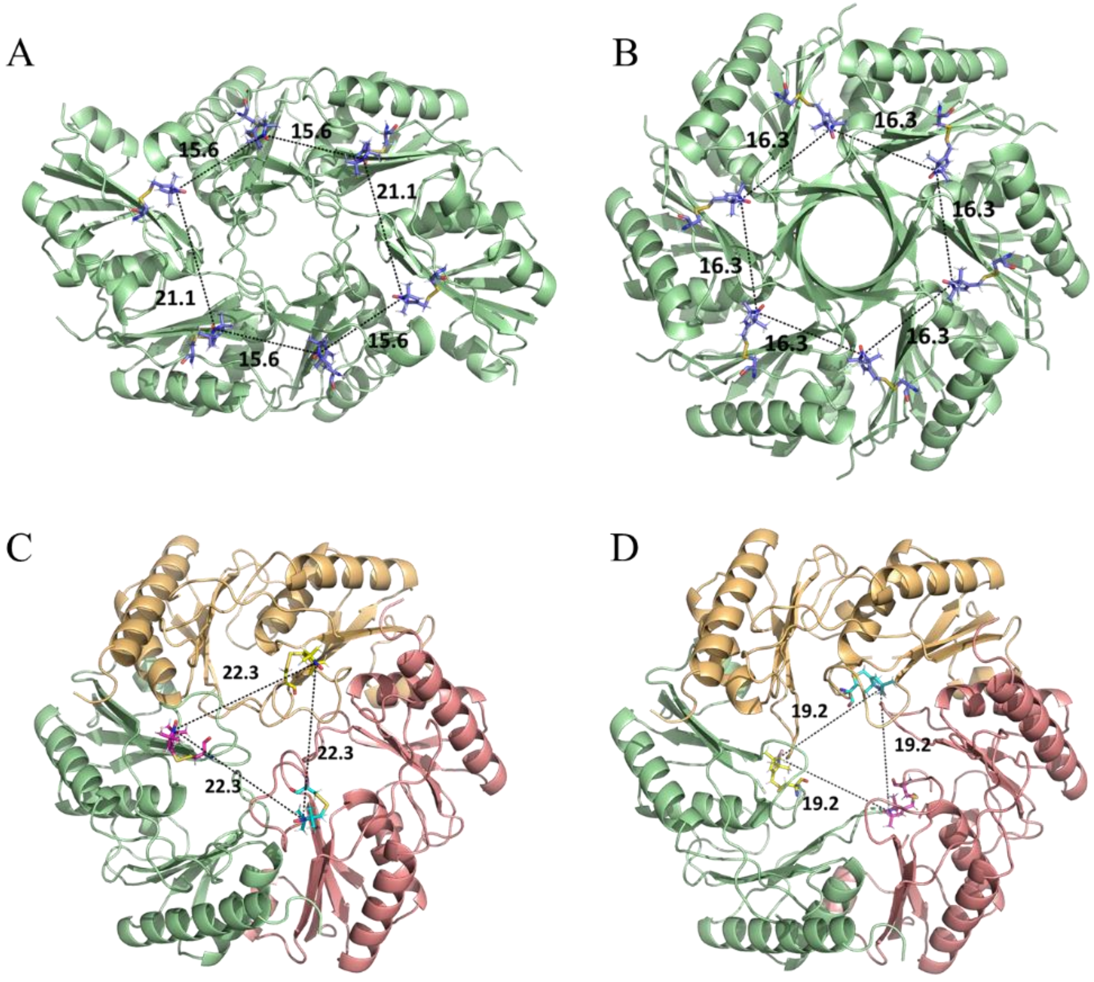

Figure 5.5. PyMOL cartoon representation for the shell proteins EutS and EutL with the most probable MTSL rotamers. The figure shows EutS WT (A) and mutant G39V (B), and EutL closed (C) and open (D) conformations. The distances between the most probable rotameric states with the values in Å are indicated. Distances are determined in PyMOL between the N-O groups from the MTSL imidazole.

Table 5.2. Distance calculations in PyMOL between modelled MTSL nitroxide labels attached to the protein at indicated sites.

Interaction type	**Distances between two interacting nitroxides (Å)**			
	EutL A73C		EutS C106	
	Open	Closed	WT	G39V
intramolecular	19.2	22.3	15.6 - 21.1	16.3
intermolecular	-	-	35 - 47	21.4

5.3.4. SDSL CW-EPR of EutS

The presence of one accessible cysteine at position 106 in each monomer of EutS is an advantage in studying this protein by using the SDSL technique. The two conformations, WT with the 40^{o} bend, and mutant G39V with the flat symmetric structure, of the EutS BMC protein are predicted to be distinguishable by SDSL CW-EPR. In addition, the six labeling sites per hexamer provide a means to characterize the structural assembly of BMC shell formed by the EutS alone. Lateral interactions between flat hexamers can be predicted by CW-EPR. Moreover, the conformation of the protein in the flat or bent forms can potentially be distinguished within the BMCs. The information from the structural analysis of the two available conformations of EutS from the PDB structures is used and the distances between the labeling sites were determined and used to predict the changes in the EPR spectra. Simulations of the dipolar interaction characteristic for the two sets of distances for EutS WT and G39V were performed for low T conditions. (Figure 5.6) Differences in the predicted EPR line shapes are indicated by the simulation between noninteracting (WT EutS) and interacting (G39V EutS) spin systems. Similarly, the characteristic line shape is simulated by the interacting spin systems characterized by dipolar coupling tensors associated with the distances that describe the two conformations and three flat proteins association. Figure 5.6 shows differences in the EPR line shapes that distinguish the different interactions.

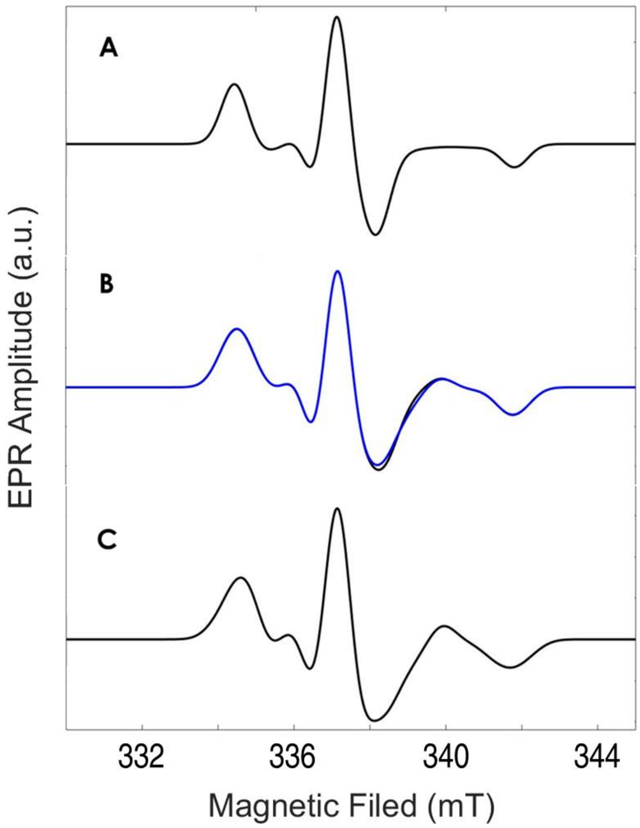

Figure 5.6. Simulated EPR signal using easyspin for the dipole-dipole interaction between the nitroxide labels predicted at the Cys106 position: A. the rigid limit spectrum; B. dipolar interaction within the hexamer of wild type (WT, black) (bend) and mutated (flat, blue) conformation of EutS; and C. the dipole-dipole interaction between three spin labels from different hexamer of the flat EutS.

EPR measurements of EutS with 4MT in a 1:1 mixture were performed at room T as the sample used showed aggregates. The results are shown in Figure 5.3. The room T lineshape of the 4MT EPR spectrum is described by the hyperfine interaction of the unpaired electron spin (S = 1/2) with the ^{14}N nuclear spin (I = 1). The electron-nuclear interaction gives three narrow EPR lines characteristic for mobile, fast motional regime with spectral width that corresponds to the isotropic hyperfine interaction with $2A_{iso}$ of 3.6 mT (or 101 MHz). The attachment of the spin label was modeled as specified above and one of the possible rotamers is shown in Figure 5.5, A and B. The low number of rotameric states at the C106 residue suggests restriction of motions and the dipolar interaction between labeled C106 would sample a small range of distances. In this case, the interaction is expected to give broadened EPR line shape at low *T* values as simulated and shown in Figure 5.6. At high *T*, the rapid tumbling of the protein would contribute to averaging out the anisotropy in the hyperfine coupling and lead to narrow lines. However large aggregates are expected to slow the motion and introduce broadening in the EPR lineshape, even at high *T* values. The experimental results of the 4MT in samples with EutS from purified protein that presented aggregates, show narrow lines in the EPR signal which suggest mobile components. This can be an indication of labeled soluble EutS oligomers, or of 4MT free in solution due to lack of labeling of aggregates which might have the C201 site buried.

In order to investigate the labeling of C106 the protein was exposed to denaturing conditions. Unfolding the samples and exposing the possible buried sites to 4MT could enable labeling. Samples that were sonicated shortly before adding the 4MT and samples containing urea were measured. The EPR signal was identical to the native labeled protein.

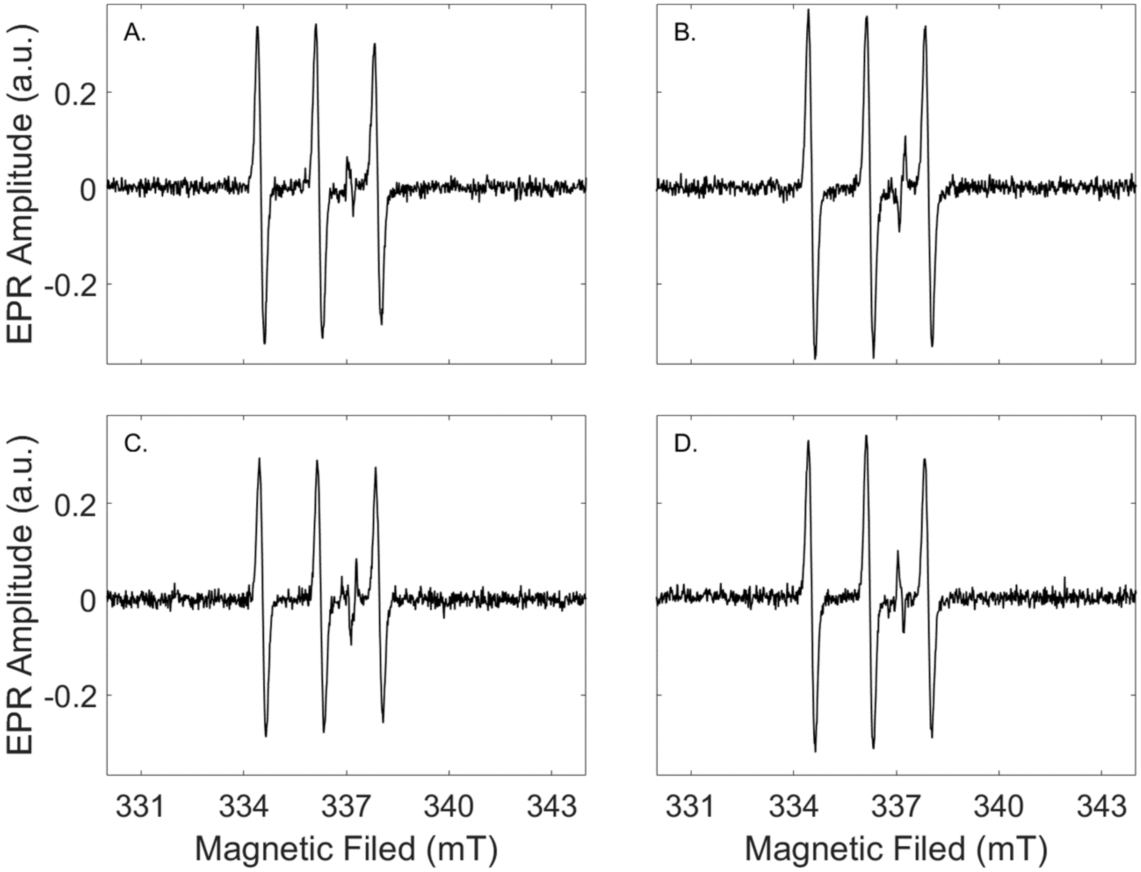

Figure 5.7. 4MT EPR spectrum for EutS protein at room *T*. Samples include 1:1 ratio of EutS to 4MT spin label with (C, D) and without (A, B) 2 M urea. Samples shown in panels B and D were subjected to sonication.

5.3.5. SDSL CW-EPR of EutL A73C C201S

The EPR lineshape of the 4MT spin label in the presence of EutL A73C C201S at different *T* condition is shown in Figure 5.8. The EPR spectrum at 120 K shows the rigid limit powder pattern line shape of the 4MT spin label. The dominant spectral features of a nitroxide spectrum arise from the electron-nuclear hyperfine interaction of the unpaired electron spin with the nuclear spin which gives $2I + 1$ EPR lines associated to the electron spin transitions between $m_I = 0, \pm 1$ energy states. The *z*-component of the anisotropic hyperfine tensor, A_{zz}, characterizes the rigid-limit line shape by a spectral width of $2A_{zz}$ of 7.5 mT (or 210 MHz). The presence of EutL was expected to broaden the lineshape due to dipolar interaction between the 4MT labels at the A73C residue within each monomer. The distances between the MTSL models determined from PyMOL predicted a dipolar coupling of ~ 5 MHz for the closed conformation and ~7 MHz for the open conformation.

The presence of EutL A73C C201S does not show changes to the 4MT EPR line shape for 120 K condition. The induced open conformation by adding Zn was predicted to cause larger broadening and that was expected to be observed in the EPR spectrum. However, no significant changes in the line shape were observed at 120 K. Including Zn to the sample prior to 4MT could create two different scenarios due to dialysis step: the sample can be locked to the open conformation by bound Zn; or a closed conformation can be obtained by losing Zn from solution and consequently from the protein bound state. The spectral width $2A_{zz}$ was determined to be about 7.6 mT (212.8 MHz) for the sample with EutL in the closed conformation, and about 7.8 mT (218.4 MHz) for the open induced conformation. Stepping to higher T values the EPR signal of 4MT with protein or protein and Zn exhibits a characteristic lineshape of a lower mobility nitroxide. The addition of Zn indicates a rigid-to-mobile transition at higher T which suggest a more restricted motional environment of the spin label molecule.

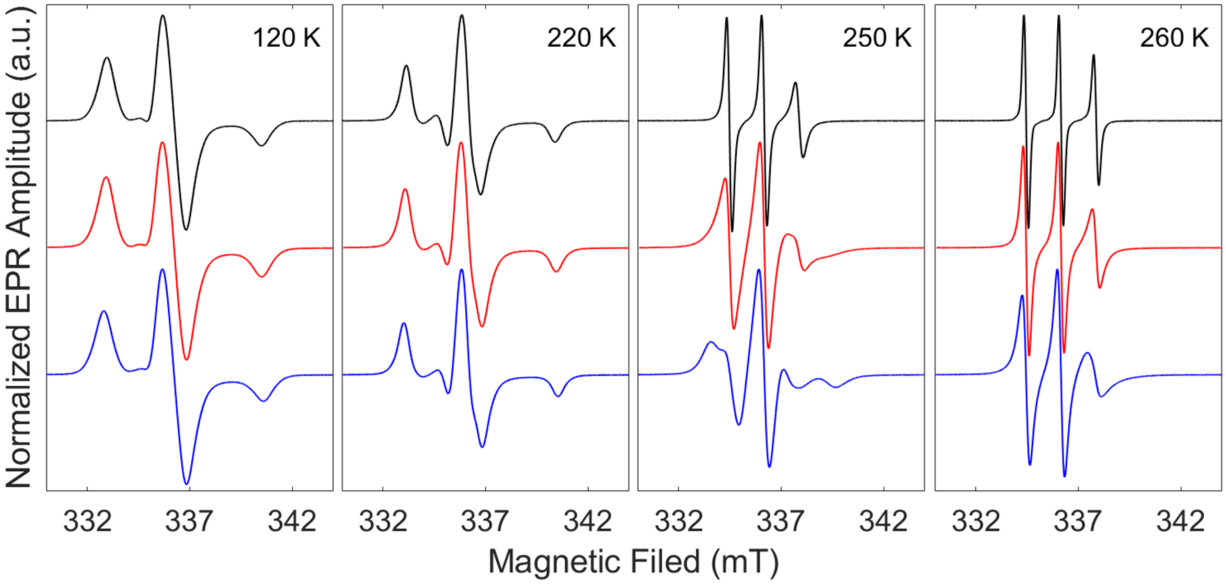

Figure 5.8. 4MT EPR spectrum for EutL A73C C201 labeled protein. EPR lineshape was observed at different *T* values, 120 K, 220 K, 250 K and 260 K. Samples contain 1:10 ratio of EutL A73C C201 to 4MT label, and 6 % v/v DMSO. A 4 h dialysis was done for each. The spectra shown for each *T* value are: 4MT (black) in buffer, 4MT in solution with EutL A73C C201 (red) and 4MT in solution with EutL A73C C201 and 1 M Zn (blue). The EPR amplitude is normalized to the central feature amplitude.

5.4. Summary

The EutS protein alone can form BMC shells in *E. coli*,[88, 139] and our preliminary results confirm its propensity to form higher-molecular mass entities. The engineered EutS shells were reported to have diameters of 50 nm, which would account for a MW of about 3000 kDa. Only a fourth of this MW was detected in our EutS purified samples. The size exclusion separation using the FPLC Superdex 200 suggests the existence of different oligomeric structures in the EutS and EutL purified samples with the higher MW of ~700 and ~1700 kDa. There is a significant tendency in forming higher order oligomers of MW of 700 kDa over hexamers for EutS, while EutL is mostly purified as trimer. Although EutS higher MW oligomer is only a small fraction of what a shell would be, this protein can also associate to form tiles.

The distances between the spin labels at selected sites in EutS and EutL A73C C201S proposed to identify intra- and intermolecular interactions for the shell proteins were determined using MMM rotameric states models and PyMOL, and were used to simulate the CW-EPR spectra. The line shape of the EPR simulated signal obtained in the presence or absence of three electron spins interaction, that describe the distances between EutS hexamers of flat or bent conformation, show distinction between the two EutS structures. The ability to distinguish between the two EutS conformations suggests the possibility to characterize the structural composition of the EutS BMC shell. However, the experimental results do not identify changes in the EPR spectra. EutL labeled with 4MT did not show evidence of electron-electron spin interactions at 120 K. The 3.1 Å difference in the 4MT labels distances between the open and closed conformations in the EutL trimer predicted interactions that would identify the conformational change. At higher *T* values the EPR lineshape changes between samples, and the transition mobile-to-rigid happens at higher temperature for 4MT in the presence of EutL and Zn than 4MT with EutL. However, reorientational correlation times and electron spin-spin interactions of sulfhydryl-specific spin labels, at the single cysteine site on EutS and EutL could not be determined. Future experiments that would include better control samples could confirm the labeling. In addition, a repeat of these experiments can confirm the presented results and could assign the broadening effects to the specific conformations whose interactions were predicted here.

Chapter VI

Final conclusions

6.1. Summary

In an exceptional way, enzymes increase the reaction rate by 6-12 orders of magnitude relative to uncatalyzed reactions under similar conditions by lowering the activation energy and thus the transition state energy between reactants and products.[3] The enzyme adenosilcobalamine-dependent EAL is the signature enzyme of the ethanolamine utilization pathway (Eut) in pathogenic strains of *Salmonella* and *Escherichia coli* [34] associated with microbiome disease conditions in the human gut, and has been shown to perform at the upper end of the scale.[65-67] In order to achieve lower energy barriers, it was suggested that EAL undergoes specific configurational changes during the reaction that are proposed to be coupled to both the reaction and surrounding solvent.[68] The folded native state of the proteins is strongly controlled by both intramolecular interactions and dynamics of hydration water through a series of interactions that couple to maintain the protein structure and function integrity.[69-75] Studies towards understanding the molecular mechanism of EAL catalysis and modulation by the surrounding environment by using low-*T* CW-EPR spectroscopy include advances in characterizing the kinetics and mechanism of particular steps in the catalytic cycle with insights on the effect that the solvent has on the protein surface fluctuations and catalysis.

The cosolvent-tunable dynamics determined in Chapter 2 are used to address the role of solvent dynamics in the native, productive substrate radical reaction and a well-defined non-native destructive pathway of substrate radical reaction in EAL. The catalytic machinery of EAL is sensitive to substrate structure – only the S-isomer of 2-amino-1-propanol, of the four 1,2-heteroatom aminopropanols was reported to undergo direct turnover. The cryo-*T* reaction of 2-aminopropanol described in Chapter 3 occurs with observed rate constants that are approximately 10^2-fold slower than for aminoethanol, and thus provides a stringent test of specificity of the protein guidance mechanism, and specifically, the role of fluctuations/dynamics. Additionally, the non-native destructive pathway enabled by 2-aminopropanol substrate in the EAL catalytic process generates a stable EPR probe of solvent dynamics, as described in Chapter 4. This provides a means to interrogate the coupling of the fluctuations in the PAD to configurational fluctuations in the interior of the EAL protein, and in particular at the enzyme active site.

Furthermore, the ethanolamine metabolism, initiated by EAL in the presence of substrate, has been associated with disease conditions caused by pathogenic bacteria. The implicated bacteria developed the ability to survive in low nutrient conditions by isolating the enzymes of the Eut pathway in the associated bacterial microcompartment (Eut BMC). The BMC shell, with role in regulation, efficiency and optimization of ethanolamine catabolism [30-32], is composed of five proteins [33-37] (EutS, EutM, EutN, EutL and EutK). These Eut BMCs are a topic of ongoing research due to their potential in therapeutics and new approaches to engineering multi-enzymatic synthesis. A characterization of the EutS and EutL shell proteins in Chapter 5 attempts to initiate studies on *S. typhimurium* native Eut BMC. Preliminary results report on identifying and characterizing the conformational shift in EutL and the interactions that promote shell formation by EutS alone. An understanding of how the Eut BMC mediates transport of substrate and products through its proteins, across the shell and how certain products are sequestered inside the organelle will provide a path to new drug targets, and information applicable for nano-bioreactor engineering.

6.2. Solvent-protein-reaction coupling in EAL

The correlation of the solvent and protein order and dynamics with the kinetics of the 2-aminopropanol substrate radical reactions that form native products and the non-native uncoupled species confirms and extends the model of solvent-protein-reaction coupling in EAL. Measurement of the *T*-dependance of the EPR amplitude of the paramagnetic reactants in their protein interior sites described in Chapter 4 provides a new window onto the dynamics in the PAD and mesodomain, by directly detecting the solvent dynamics. This brings the first direct evidence that changes in PAD (hydration layer) solvent order and dynamics, heretofore shown to be coupled to the reactions, are coupled to the protein interior. As found for the native substrate, aminoethanol, the ODT in the PAD perturbs the microscopic protein configurational change-mediated step of 2-aminopropanol-generated microstates $\mathbf{S_1}^{\bullet}$ and $\mathbf{S_2}^{\bullet}$ interconversion in EAL.

The finding described in Chapter 2 that the ODT in the low-*T* system with EAL and 10 mM 2-aminopropanol occurs at ~235 K, a *T* value at which the biphasic behavior of the substrate radical reaction is fully developed, suggests that the origin of the biphasic behavior (Chapter 3) at all *T* values is the interaction of the protein and the 2-aminopropanol substrate. Previous studies have shown that reaction of 2-aminopropanol with EAL is sensitive to 2-methyl isomer ([S] versus [R]), and 1-methyl-2-aminopropanols bind to the substrate binding site but are not reactive (unpublished work). The substitution of a methyl-group at C2 of aminoethanol lowers the rate of the $\mathbf{S_1}^{\bullet}$, $\mathbf{S_2}^{\bullet}$ interconversion, which is assigned to a protein configurational change step. Thus, the local intrusion of a relatively small, non-native substituent group significantly alters the ability of the protein that surrounds the substrate to reconfigure, equivalent to a 10^{-1} to 10^{-5} s^{-1} decrease in rate or +4 kcal/mol in free energy barrier (at 230 K). This suggests that the change in protein configuration proceeds by a change in a relatively few, selected coordinates. The consequence of this mismatch is critical: $\mathbf{S_1}^{\bullet}$ reacts rapidly relative to conversion to $\mathbf{S_2}^{\bullet}$ to form dead-end uncoupled Cbl(II) and radical species, inactivating the enzyme active site. The rates of the chemical reactions of $\mathbf{S_1}^{\bullet}$ and $\mathbf{S_2}^{\bullet}$ are similarly influenced by the 2-methyl substitution, but are less sensitive to the

ODT, indicating that the steric constraints dominate the determination of reaction rates over the effect of solvent.

The findings herein provide a significant step in identifying the coupling of the fluctuations in the PAD to configurational fluctuations in the interior of the enzyme. This was achieved by investigating the *T*-dependent kinetics of resolved steps in the catalytic cycle of EAL, and correlating the reactivity with the *T*-dependence of the solvent dynamics, measured by using the spin probe method, and the new approach of direct detection of the solvent dynamics by using the sensitivity of the EPR amplitude to solvent dielectric properties.

BIBLIOGRAPHY

1. Franzosa, E.A., et al., *Gut microbiome structure and metabolic activity in inflammatory bowel disease.* Nature microbiology, 2019. **4**(2): p. 293.
2. Dadswell, K., et al., *Bacterial microcompartment-mediated ethanolamine metabolism in E. coli urinary tract infection.* Infection and immunity, 2019: p. IAI. 00211-19.
3. Lodish, H., et al., *Molecular Cell Biology (Lodish.* Molecular Cell Biology, sixth ed. WH Freeman, 2007.
4. Francisco Guarner, J.-R.M., *Gut flora in health and disease.* THE LANCET, 2003. **360**.
5. Hooper, L.V. and J.I. Gordon, *Commensal host-bacterial relationships in the gut.* Science, 2001. **292**(5519): p. 1115-1118.
6. Thursby, E. and N. Juge, *Introduction to the human gut microbiota.* Biochemical Journal, 2017. **474**(11): p. 1823-1836.
7. Wu, H.-J. and E. Wu, *The role of gut microbiota in immune homeostasis and autoimmunity.* Gut microbes, 2012. **3**(1): p. 4-14.
8. Kaval, K.G. and D.A. Garsin, *Ethanolamine utilization in bacteria.* MBio, 2018. **9**(1): p. e00066-18.
9. White, D., *The phospholipid composition of mammalian tissues.* Form and function of phospholipids, 1973: p. 441-482.
10. Randle, C.L., P.W. Albro, and J.C. Dittmer, *The phosphoglyceride composition of Gram-negative bacteria and the changes in composition during growth.* Biochimica et Biophysica Acta (BBA)-Lipids and Lipid Metabolism, 1969. **187**(2): p. 214-220.
11. Vance, J.E., *Phosphatidylserine and phosphatidylethanolamine in mammalian cells: two metabolically related aminophospholipids.* J Lipid Res, 2008. **49**(7): p. 1377-1387.
12. Menon, A. and V. Stevens, *Phosphatidylethanolamine is the donor of the ethanolamine residue linking a glycosylphosphatidylinositol anchor to protein.* Journal of Biological Chemistry, 1992. **267**(22): p. 15277-15280.
13. Roof, D.M. and J.R. Roth, *Ethanolamine Utilization in Salmonella-Typhimurium.* J Bacteriol, 1988. **170**(9): p. 3855-3863.
14. Kaval, K.G., et al., *Ethanolamine Utilization and Bacterial Microcompartment Formation Are Subject to Carbon Catabolite Repression.* Journal of bacteriology, 2019. **201**(10): p. e00703-18.
15. BLACKWELL, C.M., F.A. SCARLETT, and J.M. TURNER, *Ethanolamine Catabolism by Bacteria, Including Escherichia coli.* Biochemical Society Transactions, 1976. **4**(3): p. 495-497.
16. Fox, K.A., et al., *Multiple posttranscriptional regulatory mechanisms partner to control ethanolamine utilization in Enterococcus faecalis.* Proceedings of the National Academy of Sciences, 2009. **106**(11): p. 4435-4440.
17. Bertin, Y., et al., *Enterohaemorrhagic Escherichia coli gains a competitive advantage by using ethanolamine as a nitrogen source in the bovine intestinal content.* Environmental microbiology, 2011. **13**(2): p. 365-377.
18. Del Papa, M.F. and M. Perego, *Ethanolamine activates a sensor histidine kinase regulating its utilization in Enterococcus faecalis.* Journal of bacteriology, 2008. **190**(21): p. 7147-7156.
19. Tsoy, O., D. Ravcheev, and A. Mushegian, *Comparative genomics of ethanolamine utilization.* Journal of bacteriology, 2009. **191**(23): p. 7157-7164.
20. Dussurget, O., J. Pizarro-Cerda, and P. Cossart, *Molecular Determinants of Listeria monocytogenes Virulence.* Annual Review of Microbiology, 2004. **58**(1): p. 587-610.
21. Korbel, J.O., et al., *Systematic association of genes to phenotypes by genome and literature mining.* PLoS biology, 2005. **3**(5): p. e134.

22. Bertin, Y., et al., *Enterohaemorrhagic Escherichia coli gains a competitive advantage by using ethanolamine as a nitrogen source in the bovine intestinal content.* Environ. Microbiol., 2011. **13**: p. 365-377.
23. Thiennimitr, P., et al., *Intestinal inflammation allows Salmonella to use ethanolamine to compete with the microbiota.* Proc. Natl. Acad. Sci., 2011. **108**(42): p. 17480-17485.
24. Sintsova, A., et al., *Role of ethanolamine utilization genes in host colonization during urinary tract infection.* Infection and immunity, 2018. **86**(3): p. e00542-17.
25. Li, H., et al., *Detection of biochemical pathways by probabilistic matching of phyletic vectors.* PloS one, 2009. **4**(4): p. e5326.
26. Sun, M., et al., *Microbiota metabolite short chain fatty acids, GPCR, and inflammatory bowel diseases.* Journal of gastroenterology, 2017. **52**(1): p. 1-8.
27. Garsin, D.A., *Ethanolamine utilization in bacterial pathogens: roles and regulation.* Nat. Rev. Microbiol., 2010. **8**(4): p. 290-5.
28. SCARLETT, F.A. and J. Turner, *Microbial metabolism of amino alcohols. Ethanolamine catabolism mediated by coenzyme B12-dependent ethanolamine ammonia-lyase in Escherichia coli and Klebsiella aerogenes.* Microbiology, 1976. **95**(1): p. 173-176.
29. Faust, L.R.P., et al., *Cloning, Sequencing, and Expression of the Genes Encoding the Adenosylcobalamin-Dependent Ethanolamine Ammonia-Lyase of Salmonella-Typhimurium.* J. Biol. Chem., 1990. **265**(21): p. 12462-12466.
30. Stojiljkovic, I., A.J. Baumler, and F. Heffron, *Ethanolamine utilization in Salmonella typhimurium: nucleotide sequence, protein expression, and mutational analysis of the cchA cchB eutE eutJ eutG eutH gene cluster.* J. Bacteriol., 1995. **177**(5): p. 1357-1366.
31. Kofoid, E., et al., *The 17-gene ethanolamine (eut) operon of Salmonella typhimurium encodes five homologues of carboxysome shell proteins.* J. Bacteriol., 1999. **181**(17): p. 5317-29.
32. Penrod, J.T. and J.R. Roth, *Conserving a volatile metabolite: A role for carboxysome-like organelles in Salmonella enterica.* J. Bacteriol., 2006. **188**: p. 2865-2874.
33. Ravcheev, D.A., et al., *Comparative genomic analysis reveals novel microcompartment-associated metabolic pathways in the human gut microbiome.* Frontiers in genetics, 2019. **10**: p. 636.
34. Kerfeld, C.A., et al., *Bacterial microcompartments.* Nat. Rev. Microbiol., 2018. **16**(5): p. 277-290.
35. Lee, M.J., D.J. Palmer, and M.J. Warren, *Biotechnological advances in bacterial microcompartment technology.* Trends in biotechnology, 2019. **37**(3): p. 325-336.
36. Kerfeld, C.A., S. Heinhorst, and G.C. Cannon, *Bacterial microcompartments.* Annu. Rev. Microbiol., 2010. **64**: p. 391-408.
37. Chowdhury, C., et al., *Diverse bacterial microcompartment organelles.* Microbiol. Molec. Biol. Rev., 2014. **78**: p. 438-468.
38. Guarner, F. and J.-R. Malagelada, *Gut flora in health and disease.* The Lancet, 2003. **361**(9356): p. 512-519.
39. Brinsmade, S.R., T. Paldon, and J.C. Escalante-Semerena, *Minimal functions and physiological conditions required for growth of Salmonella enterica on ethanolamine in the absence of the metabolosome.* J. Bacteriol., 2005. **187**(23): p. 8039-8046.
40. Bobik, T.A., B.P. Lehman, and T.O. Yeates, *Bacterial microcompartments: widespread prokaryotic organelles for isolation and optimization of metabolic pathways.* Mol. Microbiol., 2015. **98**: p. 193-207.
41. Marsh, E.N.G. and G.D.R. Meléndez, *Adenosylcobalamin enzymes: Theory and experiment begin to converge.* Biochimica et Biophysica Acta (BBA)-Proteins and Proteomics, 2012. **1824**(11): p. 1154-1164.

42. Sheppard, D.E., et al., *Evidence that a B₁₂-Adenosyl Transferase Is Encoded within the Ethanolamine Operon of Salmonella enterica.* Journal of Bacteriology, 2004. **186**(22): p. 7635-7644.
43. Sheppard, D.E. and J. Roth, *A rationale for autoinduction of a transcriptional activator: ethanolamine ammonia-lyase (EutBC) and the operon activator (EutR) compete for adenosyl-cobalamin in Salmonella typhimurium.* Journal of bacteriology, 1994. **176**(5): p. 1287-1296.
44. Neil, E. and G. Marsh, *Coenzyme B12 (cobalamin)-dependent enzymes.* Essays in biochemistry, 1999. **34**: p. 139-154.
45. Bradbeer, C., *Clostridial Fermentations of Choline and Ethanolamine .I. Preparation and Properties of Cell-Free Extracts.* J. Biol. Chem., 1965. **240**(12): p. 4669-4674.
46. Chang, G.W. and J.T. Chang, *Evidence for the B12-dependent enzyme ethanolamine deaminase in Salmonella.* Nature, 1975. **254**(5496): p. 150-151.
47. Blackwell, C.M. and J.M. Turner, *Microbial metabolism of amino alcohols. Formation of coenzyme B12-dependent ethanolamine ammonia-lyase and its concerted induction in Escherichia coli.* Biochemical Journal, 1978. **176**(3): p. 751-757.
48. Shibata, N., et al., *Crystal Structures of Ethanolamine Ammonia-lyase Complexed with Coenzyme B-12 Analogs and Substrates.* J. Biol. Chem., 2010. **285**(34): p. 26484-26493.
49. Banerjee, R. and S.W. Ragsdale, *The many faces of cobalamin: Catalysis by B12-dependent enzymes.* Ann. Rev. Biochem., 2003. **72**: p. 209-247.
50. Shibata, N., et al., *Direct participation of a peripheral side chain of a corrin ring in coenzyme B12 catalysis.* Angewandte Chemie, 2018. **130**(26): p. 7956-7961.
51. Sun, L. and K. Warncke, *Comparative model of EutB from coenzyme B12-dependent ethanolamine ammonia-lyase reveals a b8a8, TIM-barrel fold and radical catalytic site structural features.* Proteins: Structure, Function, and Bioinformatics, 2006. **64**(2): p. 308-319.
52. Jones, P.W. and J.M. Turner, *Interrelationships between the enzymes of ethanolamine metabolism in Escherichia coli.* Microbiology, 1984. **130**(2): p. 299-308.
53. Carty, T.J., B.M. Babior, and R.H. Abeles, *The Mechanism of Action of Ethanolamine Ammonia-Lyase, a B12-dependent Enzyme EVIDENCE FOR TWO INTERMEDIATES IN THE CATALYTIC PROCESS.* Journal of Biological Chemistry, 1974. **249**(6): p. 1683-1688.
54. Sun, L., et al., *Critical role of arginine 160 of the EutB protein subunit for active site structure and radical catalysis in coenzyme B12-dependent ethanolamine ammonia-lyase.* Biochemistry, 2008. **47**(20): p. 5523-5535.
55. Poyner, R.R., et al., *Probing nitrogen-sensitive steps in the free-radical-mediated deamination of amino alcohols by ethanolamine ammonia-lyase.* J. Am. Chem. Soc., 2006. **128**(22): p. 7120-7121.
56. Shibata, N., Y. Higuchi, and T. Toraya, *How coenzyme B12-dependent ethanolamine ammonia-lyase deals with both enantiomers of 2-amino-1-propanol as substrates: structure-based rationalization.* Biochemistry, 2010. **50**(4): p. 591-598.
57. Graves, S.W., J.A. Fox, and B.M. Babior, *Deamination of 2-aminopropanol by ethanolamine ammonia-lyase, an AdoCbl-requiring enzyme. Kinetics and isotope effects for the R and S enantiomers of the substrate.* Biochemistry, 1980. **19**(15): p. 3630-3633.
58. Bandarian, V. and G.H. Reed, *Analysis of the electron paramagnetic resonance spectrum of a radical intermediate in the coenzyme B12-dependent ethanolamine ammonia-lyase catalyzed reaction of S-2-aminopropanol.* Biochemistry, 2002. **41**(27): p. 8580-8588.
59. Canfield, J.M. and K. Warncke, *Geometry of Reactant Centers in the CoII-Substrate Radical Pair State of Coenzyme B12-Dependent Ethanolamine Deaminase Determined by using Orientation-Selection-ESEEM Spectroscopy.* J. Phys. Chem. B, 2002. **106**: p. 8831-8841.

60. Canfield, J.M. and K. Warncke, *Active Site Reactant Center Geometry in the CoII-Product Radical Pair State of Coenzyme B12-Dependent Ethanolamine Deaminase Determined by Using Orientation-Selection-ESEEM Spectroscopy.* J. Phys. Chem. B, 2005. **109**: p. 3053-3064.
61. Wang, M., et al., *Resolution and characterization of chemical steps in enzyme catalytic sequences by using low-temperature and time-resolved, full-spectrum EPR spectroscopy in fluid cryosolvent and frozen solution systems.* Meth. Enzymol., 2015. **563, Part A**: p. 59-94.
62. Bovell, A.M. and K. Warncke, *The Structural Model of Salmonella typhimurium Ethanolamine Ammonia-Lyase Directs a Rational Approach to the Assembly of the Functional [(EutB–EutC)2]3 Oligomer from Isolated Subunits.* Biochemistry, 2013. **52**(8): p. 1419-1428.
63. Mori, K., et al., *Catalytic roles of substrate-binding residues in coenzyme B12-dependent ethanolamine ammonia-lyase.* Biochemistry, 2014. **53**(16): p. 2661-2671.
64. Zhu, C. and K. Warncke, *Kinetic Isolation and Characterization of the Radical Rearrangement Step in Coenzyme B12-Dependent Ethanolamine Ammonia-Lyase.* J. Am. Chem. Soc., 2010. **132**(28): p. 9610-9615.
65. Hay, B.P. and R.G. Finke, *Thermolysis of the cobalt-carbon bond in adenosylcorrins. 3. Quantification of the axial base effect in adenosylcobalamin by the synthesis and thermolysis of axial base-free adenosylcobinamide. Insights into the energetics of enzyme-assisted cobalt-carbon bond homolysis.* Journal of the American Chemical Society, 1987. **109**(26): p. 8012-8018.
66. Finke, R.G. and B.P. Hay, *Thermolysis of adenosylcobalamin: a product, kinetic, and cobalt-carbon (C5') bond dissociation energy study.* Inorganic chemistry, 1984. **23**(20): p. 3041-3043.
67. Marsh, E.N.G. and D.P. Ballou, *Coupling of cobalt− carbon bond homolysis and hydrogen atom abstraction in adenosylcobalamin-dependent glutamate mutase.* Biochemistry, 1998. **37**(34): p. 11864-11872.
68. Kohne, M., C. Zhu, and K. Warncke, *Two dynamical regimes of the substrate radical rearrangement reaction in B12-dependent ethanolamine ammonia-lyse resolve contributions of native protein configurations and collective configurational fluctuations to catalysis.* Biochemistry, 2017. **56**: p. 3257-3264.
69. Lewandowski, J.R., et al., *Direct observation of hierarchical protein dynamics.* Science, 2015. **348**(6234): p. 578-581.
70. Laage, D., T. Elsaesser, and J.T. Hynes, *Water dynamics in the hydration shells of biomolecules.* Chemical reviews, 2017. **117**(16): p. 10694-10725.
71. Wohlfromm, T. and M. Vogel, *On the coupling of protein and water dynamics in confinement: Spatially resolved molecular dynamics simulation studies.* The Journal of chemical physics, 2019. **150**(24): p. 245101.
72. Qin, Y., L. Wang, and D. Zhong, *Dynamics and mechanism of ultrafast water–protein interactions.* Proceedings of the National Academy of Sciences, 2016. **113**(30): p. 8424-8429.
73. Fenimore, P.W., et al., *Bulk-solvent and hydration-shell fluctuations, similar to alpha- and beta-fluctuations in glasses, control protein motions and functions.* Proc. Natl. Acad. Sci., 2004. **101**(40): p. 14408-14413.
74. Frauenfelder, H., et al., *A unified model of protein dynamics.* Proc. Natl. Acad. Sci., 2009. **106**: p. 5129-5134.
75. Vitkup, D., et al., *Solvent mobility and the protein'glass' transition.* Nature structural biology, 2000. **7**(1): p. 34-38.
76. Kohne, M., et al., *Deuterium Kinetic Isotope Effects Resolve Low-Temperature Substrate Radical Reaction Pathways and Steps in B12-Dependent Ethanolamine Ammonia-Lyase.* Biochemistry, 2019. **58**(35): p. 3683-3690.
77. Ucuncuoglu, N. and K. Warncke, *Protein configurational states guide radical rearrangement catalysis in ethanolamine ammonia-lyase.* Biophys. J., 2018. **114**: p. 2775-2786.

78. Nforneh, B. and K. Warncke, *Mesodomain and protein-associated solvent phases with temperature-tunable (200-265 K) dynamics surround ethanolamine ammonia-lyase in globally polycrystalline aqueous solution containing dimethyl sulfoxide.* J. Phys. Chem. B, 2017. **121**: p. 11109-11118.
79. Nforneh, B. and K. Warncke, *Control of solvent dynamics around the B12-dependent ethanolamine ammonia-lyase enzyme in frozen aqueous solution by using dimethyl sulfoxide modulation of mesodomain volume.* J. Phys. Chem. B, 2019. **(accepted)** p. DOI: 10.1021/acs.jpcb.9b02239.
80. Kerfeld, C.A. and M.R. Melnicki, *Assembly, function and evolution of cyanobacterial carboxysomes.* Curr. Opin. Plant Biol., 2016. **31**: p. 66-75.
81. Bobik, T.A., et al., *Propanediol utilization genes (pdu) of Salmonella typhimurium: three genes for the propanediol dehydratase.* Journal of Bacteriology, 1997. **179**(21): p. 6633-6639.
82. Yeates, T.O., J. Jorda, and T.A. Bobik, *The shells of BMC-type microcompartment organelles in bacteria.* Journal of molecular microbiology and biotechnology, 2013. **23**(4-5): p. 290-299.
83. Takenoya, M., K. Nikolakakis, and M. Sagermann, *Crystallographic insights into the pore structures and mechanisms of the EutL and EutM shell proteins of the ethanolamine-utilizing microcompartment of Escherichia coli.* J. Bacteriol., 2010. **192**(22): p. 6056-6063.
84. Joseph, B., et al., *Identification of Listeria monocytogenes genes contributing to intracellular replication by expression profiling and mutant screening.* Journal of bacteriology, 2006. **188**(2): p. 556-568.
85. Tanaka, S., M.R. Sawaya, and T.O. Yeates, *Structure and mechanisms of a protein-based organelle in Escherichia coli.* Science, 2010. **327**(5961): p. 81-84.
86. Yeates, T.O., M.C. Thompson, and T.A. Bobik, *The protein shells of bacterial microcompartment organelles.* Curr. Op. Struct. Biol., 2011. **21**: p. 223-231.
87. Chowdhury, C., et al., *Selective molecular transport through the protein shell of a bacterial microcompartment organelle.* Proc. Natl. Acad. Sci., 2015. **112**: p. 2990-2995.
88. Choudhary, S., et al., *Engineered protein nano-compartments for targeted enzyme localization.* PLoS One, 2012. **7**(3): p. e33342.
89. Sagermann, M., A. Ohtaki, and K. Nikolakakis, *Crystal structure of the EutL shell protein of the ethanolamine ammonia lyase microcompartment.* Proceedings of the National Academy of Sciences, 2009. **106**(22): p. 8883-8887.
90. Liu, J., J. Dai, and M. Lu, *Zinc-mediated helix capping in a triple-helical protein.* Biochemistry, 2003. **42**(19): p. 5657-5664.
91. Thompson, M.C., et al., *An allosteric model for control of pore opening by substrate binding in the EutL microcompartment shell protein.* Protein Sci., 2015. **24**(6): p. 956-975.
92. Axen, S.D., O. Erbilgin, and C.A. Kerfeld, *A taxonomy of bacterial microcompartment loci constructed by a novel scoring method.* PLoS computational biology, 2014. **10**(10).
93. Wang, M. and K. Warncke, *Kinetic and Thermodynamic Characterization of CoII-Substrate Radical Pair Formation in Coenzyme B12-Dependent Ethanolamine Ammonia-Lyase in a Cryosolvent System by using Time-Resolved, Full-Spectrum Continuous-Wave Electron Paramagnetic Resonance Spectroscopy.* J. Am. Chem. Soc., 2008. **130**: p. 4846-4858.
94. Klug, C.S. and J.B. Feix, *Methods and applications of site-directed spin labeling EPR spectroscopy.* Methods Cell Biol., 2008. **84**: p. 617-658.
95. Altenbach, C., et al., *Exploring structure, dynamics and topology of nitroxide spin-labeled proteins using continuous-wave electron paramagnetic resonance spectroscopy.* Meth. Enzymol., 2015. **564** p. 59-100.
96. Nforneh, B. and K. Warncke, *Electron spin labeling of the EutC subunit in B12-dependent ethanolamine ammonia-lyase reveals dynamics and a two-state conformational equilibrium in the N-terminal, signal-sequence-associated domain.* Free Radical Res., 2017. **52**: p. 307-318.

97. Weil, J.A. and J.R. Bolton, *Electron paramagnetic resonance: elementary theory and practical applications*. 2007: John Wiley & Sons.
98. Wertz, J.E. and J.R. Bolton, *Basic Principles of Electron Spin Resonance*, in *Electron Spin Resonance*. 1986, Springer. p. 1-20.
99. Schweiger, A. and G. Jeschke, *Principles of pulse electron paramagnetic resonance*. 2001, Oxford, UK: Oxford University Press.
100. Bhat, S.N., A. Sharma, and S.V. Bhat, *Vitrification and glass transition of water: Insights from spin probe ESR.* Phys. Rev. Lett., 2005. **95**: p. 2357021-2357024.
101. Banerjee, D. and S.V. Bhat, *Vitrification, relaxation and free volume in glycerol-water binary liquid mixture: Spin probe ESR studies.* J. Non-Cryst. Solids, 2009. **355**: p. 2433-2438.
102. Banerjee, D., et al., *ESR evidence for 2 coexisting liquid phases in deeply supercooled bulk water.* Proceedings of the National Academy of Sciences, 2009. **106**(28): p. 11448-11453.
103. Bartoš, J. and H. Švajdlenková, *On the mutual relationships between spin probe mobility, free volume and relaxation dynamics in organic glass-formers: Glycerol.* Chemical Physics Letters, 2017. **670**: p. 58-63.
104. Evans, E.G., et al., *Interaction between prion protein's copper-bound octarepeat domain and a charged C-terminal pocket suggests a mechanism for N-terminal regulation.* Structure, 2016. **24**(7): p. 1057-1067.
105. Ling, S., et al., *Combined approaches of EPR and NMR illustrate only one transmembrane helix in the human IFITM3.* Scientific reports, 2016. **6**(1): p. 1-8.
106. Warncke, K., J.C. Schmidt, and S.-C. Ke, *Identification of a Rearranged-Substrate, Product Radical Intermediate and the Contribution of a Product Radical Trap in Vitamin B12 Coenzyme-Dependent Ethanolamine Deaminase Catalysis.* J. Am. Chem. Soc., 1999. **121**(45): p. 10522-10528 [Correction: J. Am. Chem. Soc. 130, 6055 (2008)].
107. Zhu, C. and K. Warncke, *Reaction of the CoII-Substrate Radical Pair Catalytic Intermediate in Coenzyme B12-Dependent Ethanolamine Ammonia-Lyase in Frozen Aqueous Solution from 190 to 217 Kelvin.* Biophys. J., 2008. **95**: p. 5890-5900.
108. Babior, B.M., et al., *Mechanism of Action of Ethanolamine Ammonia-Lyase, a B12-Dependent Enzyme - Participation of Paramagnetic Species in Catalytic Deamination of 2-Aminopropanol.* J. Biol. Chem., 1974. **249**(14): p. 4537-4544.
109. Pilbrow, J. and M. Winfield, *Computer simulation of low symmetry ESR spectra due to vitamin B12r and model systems.* Molecular Physics, 1973. **25**(5): p. 1073-1092.
110. Hamilton, J., et al., *Formation of a cobamide containing divalent cobalt by the ribonucleotide reductase of Lactobacillus leichmannii.* Biochimica et Biophysica Acta (BBA)-General Subjects, 1969. **177**(2): p. 374-376.
111. Eaton, S., G. Eaton, and L. Berliner, *Biological Magnetic Resonance, Vol. 19.* Kluwer; New York, 2000.
112. Likhtenshtein, G.I., *Spin Labeling Methods in Molecular Biology*. 1976, New Your: John Wiley and Sons.
113. Persson, F., P. Söderhjelm, and B. Halle, *How proteins modify water dynamics.* The Journal of chemical physics, 2018. **148**(21): p. 215103.
114. Lind, P.A., et al., *Esterase catalysis of substrate vapour: enzyme activity occurs at very low hydration.* Biochimica et Biophysica Acta (BBA)-Proteins and Proteomics, 2004. **1702**(1): p. 103-110.
115. Klibanov, A.M., *Improving enzymes by using them in organic solvents.* nature, 2001. **409**(6817): p. 241-246.
116. Staib, L. and T.M. Fuchs, *From food to cell: nutrient exploitation strategies of enteropathogens.* Microbiology, 2014. **160**(6): p. 1020-1039.

117. Anderson, C.J. and M.M. Kendall, *Salmonella enterica Serovar Typhimurium strategies for host adaptation.* Front. Microbiol., 2017. **8**: p. 1983.
118. Franks, F., *Scientific and technological aspects of aqueous glasses.* Biophys. Chem., 2003. **106**: p. 251-261.
119. Goff, H.D., E. Verespej, and D. Jermann, *Glass transitions in frozen sucrose solutions are influenced by solute inclusions within ice crystals.* Thermochim. Acta, 2003. **399**: p. 43-55.
120. Franks, F., *Freeze-drying of bioproducts: putting principles into practice.* Eur. J. Pharm. Biopharm., 1998. **45**: p. 221-229.
121. Chen, H., L. Sun, and K. Warncke, *Heterogeneous ordered-disordered structure of the mesodomain in frozen sucrose-water solutions revealed by multiple electron paramagnetic resonance spectroscopies.* Langmuir, 2013. **29**: p. 4357-4365.
122. Roos, Y.H. and N. Potes, *Quantification of protein hydration, glass transitions, and structural relaxations of aqueous protein and carbohydrate–protein systems.* The Journal of Physical Chemistry B, 2015. **119**(23): p. 7077-7086.
123. Faust, L.P. and B.M. Babior, *Overexpression, Purification, and Some Properties of the Adocbl-Dependent Ethanolamine Ammonia-Lyase from Salmonella-Typhimurium.* Arch. Biochem. Biophys., 1992. **294**(1): p. 50-54.
124. Kaplan, B.H. and E. Stadtman, *Ethanolamine Deaminase, a Cobamide Coenzyme-dependent Enzyme II. Physical and chemical properties and interaction with cobamides and ethanolamine.* Journal of Biological Chemistry, 1968. **243**(8): p. 1794-1803.
125. Stoll, S. and A. Schweiger, *EasySpin, a comprehensive software package for spectral simulation and analysis in EPR.* J. Magn. Reson., 2006. **178**: p. 42-55.
126. Rasmussen, D. and A. MacKenzie, *Phase diagram for the system water–dimethylsulphoxide.* Nature, 1968. **220**(5174): p. 1315-1317.
127. Baudot, A., et al., *Thermal study of simple amino-alcohol solutions.* Cryobiology, 2002. **44**(2): p. 150-160.
128. Mehl, P.M., *The effect of the functional groups of organic solutes on the suppression of crystallization in aqueous solutions.* Thermochimica acta, 1993. **226**: p. 325-332.
129. Toraya, T., *Radical Catalysis in Coenzyme B12-Dependent Isomerization (Eliminating) Reactions.* Chem. Rev., 2003. **103**: p. 2095-2127.
130. Frey, P.A., *Cobalamin coenzymes in enzymology*, in *Comprehensive Natural Products II Chemistry and Biology*, L. Mander and H.-W. Lui, Editors. 2010, Elsevier: Oxford UK. p. 501-546.
131. Banerjee, R., *Introduction to the Thematic Minireview Series: Host-microbiome metabolic interplay.* J. Biol. Chem., 2017. **293**: p. 8544-8545.
132. Rupp, H., et al., *Electron spin relaxation of iron-sulphur proteins studied by microwave power saturation.* Biochimica et Biophysica Acta (BBA)-Protein Structure, 1978. **537**(2): p. 255-269.
133. Castner Jr, T., *Saturation of the paramagnetic resonance of a V center.* Physical Review, 1959. **115**(6): p. 1506.
134. Pascutti, P.G. and A.S. Ito, *EPR study of melanin-protein interaction: photoinduced free radicals and progressive microwave power saturation.* Journal of Photochemistry and Photobiology B: Biology, 1992. **16**(3-4): p. 257-266.
135. Brudvig, G.W., *[22] Electron paramagnetic resonance spectroscopy*, in *Methods in enzymology*. 1995, Elsevier. p. 536-554.
136. Berliner, L.J., S.S. Eaton, and G.R. Eaton, *Distance measurements in biological systems by EPR*. Vol. 19. 2006: Springer Science & Business Media.
137. Poole, C., *Electron Spin.* Resonance, 1983.
138. Dalal, D.P., S.S. Eaton, and G.R. Eaton, *The effects of lossy solvents on quantitative EPR studies.* Journal of Magnetic Resonance (1969), 1981. **44**(3): p. 415-428.

139. Held, M., et al., *Engineering formation of multiple recombinant Eut protein nanocompartments in E. coli.* Sci. Rep., 2016. **6**: p. 24359.
140. Crowley, C.S., et al., *Structural insight into the mechanisms of transport across the Salmonella enterica Pdu microcompartment shell.* Journal of Biological Chemistry, 2010. **285**(48): p. 37838-37846.
141. Aussignargues, C., et al., *Bacterial microcompartment assembly: The key role of encapsulation peptides.* Commun. Integr. Biol., 2015. **8**(3): p. e1039755.
142. Roser, P., et al., *Site-directed spin labeling of proteins for distance measurements in vitro and in cells.* Organic & biomolecular chemistry, 2016. **14**(24): p. 5468-5476.
143. Kunjir, N.C., et al., *Measurements of short distances between trityl spin labels with CW EPR, DQC and PELDOR.* Physical Chemistry Chemical Physics, 2013. **15**(45): p. 19673-19685.
144. Rabenstein, M.D. and Y.K. Shin, *Determination of the distance between two spin labels attached to a macromolecule.* Proc. Natl. Acad. Sci., 1995. **92**: p. 8239-8243.
145. Lawrence, A.D., et al., *Solution structure of a bacterial microcompartment targeting peptide and its application in the construction of an ethanol bioreactor.* ACS Synth. Biol., 2014. **3**(7): p. 454-465.
146. Cai, F., et al., *Engineering bacterial microcompartment shells: chimeric shell proteins and chimeric carboxysome shells.* ACS synthetic biology, 2015. **4**(4): p. 444-453.
147. Plegaria, J.S. and C.A. Kerfeld, *Engineering nanoreactors using bacterial microcompartment architectures.* Curr. Opin. Biotechnol., 2018. **51**: p. 1-7.
148. Nikolakakis, K., et al., *Preliminary structural investigations of the Eut-L shell protein of the ethanolamine ammonia-lyase metabolosome of Escherichia coli.* Acta Crystallographica Section F: Structural Biology and Crystallization Communications, 2009. **65**(2): p. 128-132.
149. Moore, T.C. and J.C. Escalante-Semerena, *The EutQ and EutP proteins are novel acetate kinases involved in ethanolamine catabolism: physiological implications for the function of the ethanolamine metabolosome in Salmonella enterica.* Mol. Microbiol., 2016. **99**: p. 497-511.
150. Chowdhury, C., et al., *The function of the PduJ microcompartment shell protein is determined by the genomic position of its encoding gene.* Molecular microbiology, 2016. **101**(5): p. 770-783.
151. Langen, R., et al., *Crystal structures of spin labeled T4 lysozyme mutants: implications for the interpretation of EPR spectra in terms of structure.* Biochemistry, 2000. **39**(29): p. 8396-8405.
152. Hubbell, W.L., et al., *Technological advances in site-directed spin labeling of proteins.* Current opinion in structural biology, 2013. **23**(5): p. 725-733.
153. Schrödinger, L., *PyMOL Molecular Graphics System.* Version 2.0.
154. Madden, T., *The BLAST sequence analysis tool*, in *The NCBI Handbook [Internet]. 2nd edition*. 2013, National Center for Biotechnology Information (US).
155. Combet, C., et al., *Geno3D: automatic comparative molecular modelling of protein.* Bioinformatics, 2002. **18**(1): p. 213-214.
156. Lodish H, B.A., Zipursky SL, et al., *Molecular cell biology. 4th edition.* New York: W. H. Freeman, 2013.
157. Michael C. Thompson, D.C., David J. Leibly, Todd O. Yeates, *An allosteric model for control of pore opening by substrate binding in the EutL microcompartment shell protein.* PROTEIN SCIENCE, 2015. **24**: p. 956—975.
158. Krissinel, E. and K. Henrick, *Inference of macromolecular assemblies from crystalline state.* Journal of molecular biology, 2007. **372**(3): p. 774-797.
159. Riener, C.K., G. Kada, and H.J. Gruber, *Quick measurement of protein sulfhydryls with Ellman's reagent and with 4, 4′-dithiodipyridine.* Analytical and bioanalytical chemistry, 2002. **373**(4-5): p. 266-276.

Appendix

A. Chapter I

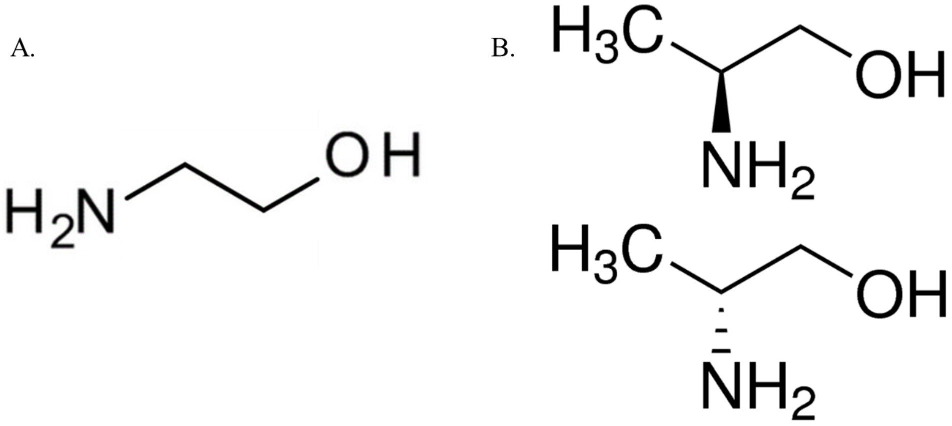

Figure A. 1. The chemical structures of the three AdoCbl-dependent EAL substrates. Panel A. shows EA and B. the enantiomers of the 2-aminopropanol: (S)-2-aminopropanol (top), and (R)-2-aminopropanol (bottom).

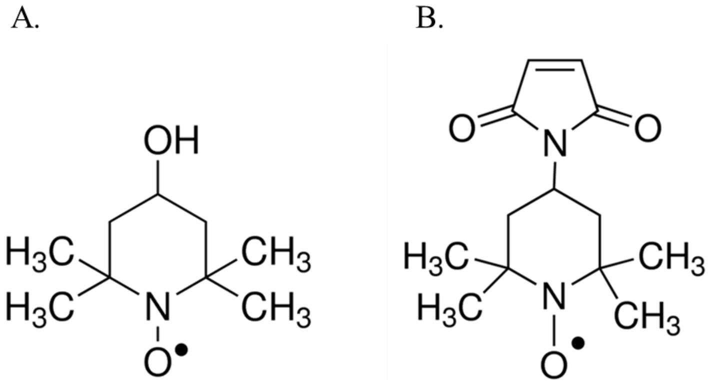

Figure A.2. Structure of 4-hydroxyl TEMPO (TEMPOL) spin probe (A) and 4-maleimido TEMPO (4MT) spin label (B).

B. Appendix for Chapter II

Table B.1. The logτ_c and W values at different T values for TEMPOL in solution of EAL and 10 mM 2-aminopropanol.

T (K)	Log$\tau_{c,f}$ (s)	W_f	Log$\tau_{c,s}$ (s)	W_s
220	-5.88 ± 0.14	0.89 ± 0.01	-4.07 ± 0.01	0.11 ± 0.01
225	-6.79 ± 0.09	0.90 ± 0.02	-4.32 ± 0.01	0.10 ± 0.02
230	-7.17 ± 0.02	0.89 ± 0.02	-6.40 ± 0.04	0.11 ± 0.02
235	-7.97 ± 0.05	0.38 ± 0.02	-7.04 ± 0.07	0.62 ± 0.02
240	-8.30 ± 0.02	0.35 ± 0.04	-7.15 ± 0.07	0.65 ± 0.04
245	-8.53 ± 0.07	0.37 ± 0.06	-7.76 ± 0.11	0.63 ± 0.06
250	-8.82 ± 0.10	0.45 ± 0.05	-8.02 ± 0.16	0.55 ± 0.05
255	-9.14 ± 0.08	0.55 ± 0.08	-8.35 ± 0.15	0.45 ± 0.08
260	-9.47 ± 0.04	0.62 ± 0.06	-8.76 ± 0.08	0.38 ± 0.06
265	-9.76 ± 0.02	0.70 ± 0.05	-9.05 ± 0.06	0.30 ± 0.05

Table B.2. The logτ_c and W values at different T values for TEMPOL in solution of EAL with 10 mM 2-aminopropanol and 2 % v/v DMSO.

T (K)	Log$\tau_{c,f}$ (s)	W_f	Log$\tau_{c,s}$ (s)	W_s
200	-6.93 ± 0.21	0.94 ± 0.02	-5.18 ± 0.01	0.06 ± 0.02
205	-7.46 ± 0.03	0.92 ± 0.03	-6.60 ± 0.05	0.08 ± 0.03
210	-7.71 ± 0.14	0.76 ± 0.03	-7.13 ± 0.02	0.24 ± 0.03
215	-8.04 ± 0.11	0.73 ± 0.03	-7.41 ± 0.09	0.27 ± 0.03
220	-8.29 ± 0.08	0.72 ± 0.00	-7.63 ± 0.08	0.28 ± 0.00
225	-8.51 ± 0.08	0.68 ± 0.04	-7.90 ± 0.11	0.32 ± 0.04
230	-8.69 ± 0.08	0.72 ± 0.01	-8.08 ± 0.09	0.28 ± 0.01
235	-8.90 ± 0.05	0.73 ± 0.02	-8.36 ± 0.06	0.27 ± 0.02
240	-9.10 ± 0.06	0.71 ± 0.03	-8.62 ± 0.04	0.29 ± 0.03
245	-9.29 ± 0.04	0.72 ± 0.01	-8.85 ± 0.02	0.28 ± 0.01
250	-9.48 ± 0.03	0.75 ± 0.01	-9.04 ± 0.02	0.25 ± 0.01
255	-9.65 ± 0.02	0.77 ± 0.01	-9.14 ± 0.04	0.23 ± 0.01
260	-9.84 ± 0.02	0.80 ± 0.01	-9.47 ± 0.03	0.20 ± 0.01
265	-9.98 ± 0.01	0.82 ± 0.01	-9.59 ± 0.05	0.18 ± 0.01

C. Appendix for Chapter III

The functions that describe the kinetic time evolution of the measured states

The form of the equations that describe the minimal model of three steps, four states used to numerically simulate the experimental data was calculated from the set of differential equations that describe the system (eq 3.4, 3.5, 3.6, 3.7). Under the initial conditions mentioned in the Chapter 3 these equations are:

$$S(t) = \frac{k_1 a_1 + k_2 a_2 - \kappa_-}{\kappa_+ - \kappa_-} e^{-\kappa_+ t} + \frac{-k_1 a_1 - k_2 a_2 + \kappa_+}{\kappa_+ - \kappa_-} e^{-\kappa_- t} \tag{C. 1}$$

$$X(t) = \frac{(k_1 + k_3 - \kappa_-) a_1 - k_4 a_2}{\kappa_+ - \kappa_-} \times \frac{k_1 (1 - e^{-\kappa_+ t})}{\kappa_+} + \frac{-(k_1 + k_3 - \kappa_+) a_1 + k_4 a_2}{\kappa_+ - \kappa_-} \times \frac{k_1 (1 - e^{-\kappa_- t})}{\kappa_-} \tag{C. 2}$$

$$P(t) = \frac{-k_3 a_1 + (k_2 + k_4 - \kappa_-) a_2}{\kappa_+ - \kappa_-} \times \frac{k_2 (1 - e^{-\kappa_+ t})}{\kappa_+} + \frac{k_3 a_1 - (k_2 + k_4 - \kappa_+) a_2}{\kappa_+ - \kappa_-} \times \frac{k_2 (1 - e^{-\kappa_- t})}{\kappa_-} \tag{C. 3}$$

$$S_1(t) = \frac{(k_1 + k_3 - \kappa_-) a_1 - k_4 a_2}{\kappa_+ - \kappa_-} e^{-\kappa_+ t} + \frac{-(k_1 + k_3 - \kappa_+) a_1 + k_4 a_2}{\kappa_+ - \kappa_-} e^{-\kappa_- t} \tag{C. 4}$$

$$S_2(t) = \frac{-k_3 a_1 + (k_2 + k_4 - \kappa_-) a_2}{\kappa_+ - \kappa_-} e^{-\kappa_+ t} + \frac{k_3 a_1 - (k_2 + k_4 - \kappa_+) a_2}{\kappa_+ - \kappa_-} e^{-\kappa_- t} \tag{C. 5}$$

The composite/ observed rate constants that are obtained from empirical fits of the data have the following dependence on the microscopic rate constants:

$$\kappa_{\pm} = \frac{(k_1 + k_2 + k_3 + k_4) \pm \sqrt{(k_1 - k_2 + k_3 + k_4)^2 - 4k_4(k_1 - k_2)}}{2} \tag{C. 6}$$

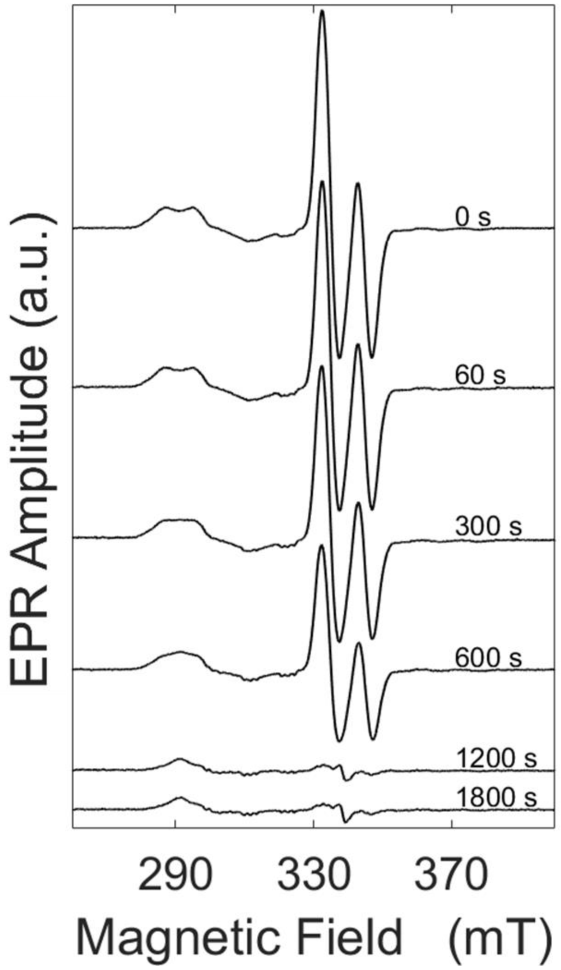

Figure C.1. Time-dependence of the Cbl(II)- 2-aminopropanol substrate radical pair state in EAL. The signal was measured at 120 K and each scan corresponds to a sample incubated at 288 K for the time interval indicated.

Table C.1. Normalized weights of the substrate radical ($\mathbf{S}^{\bullet}$) and uncoupled Cbl(II) ($\mathbf{X}^{\bullet}$) components at the end of the decay at each temperature, relative to the initial cryotrapped Cbl(II)-substrate radical pair concentration. The diamagnetic product is calculated according to equation 3.1. The normalized values are calculated from the AUC values for initial and final EPR absorption spectra. Parameters represent the mean values ± standard deviation, for three separate decay measurements at each temperature.

% v/v DMSO	**T (K)**	**Normalized Weights**		
		$S^{\bullet}$	**$X^{\bullet}$**	**P**
0	210	0.03 ± 0.005	0.43 ± 0.076	0.54 ± 0.078
	220	0.10 ± 0.017	0.53 ± 0.076	0.37 ± 0.093
	230	0.08 ± 0.019	0.58 ± 0.098	0.33 ± 0.105
	240	0.10 ± 0.006	0.62 ± 0.055	0.26 ± 0.049
	288*	0.04	0.26	0.70
2	230	0.12 ± 0.028	0.43 ± 0.094	0.44 ± 0.110
	240	0.09 ± 0.017	0.30 ± 0.086	0.61 ± 0.074
4	230	0.12 ± 0.031	0.60 ± 0.041	0.27 ± 0.057
	240	0.10 ± 0.083	0.72 ± 0.195	0.19 ± 0.201

* one sample measured.

Table C.2. Estimates for the total uncoupled Cbl(II) and diamagnetic product formed after the decay of the total radical pair. The values are calculated from the normalized weights of the components determined from the AUC values for initial and final EPR absorption spectra. Parameters represent the mean values ± standard deviation, for three separate decay measurements at each temperature.

% v/v DMSO	**T (K)**	**$X^{\bullet}$**	**P**
0	210	0.44 ± 0.079	0.55 ± 0.080
	220	0.58 ± 0.092	0.41 ± 0.096
	230	0.63 ± 0.106	0.36 ± 0.111
	240	0.68 ± 0.060	0.29 ± 0.054
2	230	0.48 ± 0.115	0.49 ± 0.115
	240	0.32 ± 0.090	0.66 ± 0.083
4	230	0.68 ± 0.054	0.30 ± 0.059
	240	0.78 ± 0.208	0.21 ± 0.211

Table C.3. First-order rate constants of the microscopic kinetic model that simulates the Cbl(II)-substrate radical pair decay kinetics at the respective *T* values. The values represent the mean ± standard deviation, for three separate decay experiments fits at each temperature.

% v/v DMSO	***T* (K)**	**$k_1 \times 10^{-4}$ (s^{-1})**	**$k_2 \times 10^{-4}$ (s^{-1})**	**$k_3 \times 10^{-4}$ (s^{-1})**	**$k_4 \times 10^{-4}$ (s^{-1})**	**R^2**
0	210	0.18 ± 0.01	0.13 ± 0.04	6 ± 5 (× 10^{-4})	4 ± 5 (× 10^{-4})	0.9317 ± 0.0766
	220	1.85 ± 0.65	0.16 ± 0.01	0.07 ± 0.03	0.07 ± 0.01	0.9280 ± 0.0386
	230	3.31 ± 2.17	0.30 ± 0.05	0.29 ± 0.22	0.23 ± 0.04	0.9566 ± 0.0060
	240	3.43 ± 0.60	0.69 ± 0.14	0.29 ± 0.25	0.28 ± 0.14	0.9762 ± 0.0090
2	230	0.66 ± 0.09	0.21 ± 0.02	1.62 ± 1.08	0.37 ± 0.11	0.9842 ± 0.0037
	240	0.39 ± 0.11	3.04 ± 0.69	0.17 ± 0.06	0.38 ± 0.06	0.9439 ± 0.0119
4	230	0.53 ± 0.07	0.14 ± 0.04	0.59 ± 0.41	0.32 ± 0.20	0.9514 ± 0.0122
	240	1.15 ± 1.28	3.73 ± 3.38	0.66 ± 0.99	1.98 ± 1.36	0.7135 ± 0.1085

Table C.4. The initial concentration of the substrate radical present in the **$S_1^{\bullet}$** and **$S_2^{\bullet}$** states as calculated by the simulations of the four states, three steps kinetic model. The values represent the mean ± standard deviation, for three separate decay measurements at each temperature.

% v/v DMSO	**T (K)**	**[$S_1^{\bullet}$]**	**[$S_2^{\bullet}$]**
0	210	0.40 ± 0.05	0.60 ± 0.05
	220	0.36 ± 0.14	0.64 ± 0.14
	230	0.39 ± 0.21	0.61 ± 0.21
	240	0.53 ± 0.06	0.47 ± 0.06
2	230	0.59 ± 0.15	0.41 ± 0.15
	240	0.43 ± 0.10	0.57 ± 0.10
4	230	0.62 ± 0.08	0.38 ± 0.08
	240	0.64 ± 0.20	0.36 ± 0.20

Alternative model tested for Cbl(II)-2-aminopropanol substrate radical pair decay in EAL in reaction solution of different % v/v DMSO.

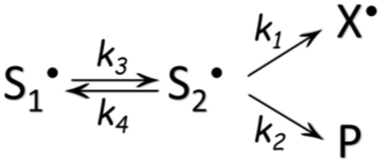

Figure C.2. Alternative microscopic kinetic model tested for the mechanism of the Cbl(II)-2-aminopropanol substrate radical pair decay in EAL

The mechanism considers two sequential microstates with different protein configurations, $\mathbf{S_1^\bullet}$ and $\mathbf{S_2^\bullet}$, where $\mathbf{S_1^\bullet}$ is the substrate radical capture state, and $\mathbf{S_2^\bullet}$ is the radical rearrangement state. The nascent radical state, $\mathbf{S_1^\bullet}$ populates $\mathbf{S_2^\bullet}$ with a first-order rate constant k_3, and $\mathbf{S_2^\bullet}$ enables the diamagnetic product **P** or uncoupled radical species $\mathbf{X^\bullet}$ formation with the rate constants k_2 and k_1. Under the non-native substrate, the $\mathbf{S_2^\bullet}$ state captures two hybrid indistinguishable conformations of the substrate radical ($\mathbf{S_2^{\bullet\prime}}$ and $\mathbf{S_2^{\bullet\prime\prime}}$) which determine the fate of the pathway, into $\mathbf{X^\bullet}$ or **P** formation. The reverse reaction $\mathbf{S_2^\bullet}$ to $\mathbf{S_1^\bullet}$ (k_4) is also possible. The set of solutions of the differential equations that describe the model in Figure C.2 defined by $\mathbf{S^\bullet}$(t), **P**(t) and $\mathbf{X^\bullet}$(t) are simulated, presenting good fits to the experimental data (Figure C.3).

$$S(t) = \frac{(k_1 + k_2)a_2 - \kappa_-}{\kappa_+ - \kappa_-} e^{-\kappa_+ t} + \frac{-(k_1 + k_2)a_2 + \kappa_+}{\kappa_+ - \kappa_-} e^{-\kappa_- t} \qquad \text{(C. 7)}$$

$$X(t) = \frac{-k_3 a_1 + (k_1 + k_2 + k_4 - \kappa_-)a_2}{\kappa_+ - \kappa_-} \times \frac{k_1(1 - e^{-\kappa_+ t})}{\kappa_+} + \frac{k_3 a_1 - (k_1 + k_2 + k_4 - \kappa_+)a_2}{\kappa_+ - \kappa_-} \times \frac{k_1(1 - e^{-\kappa_- t})}{\kappa_-} \qquad \text{(C. 8)}$$

$$P(t) = \frac{-k_3 a_1 + (k_1 + k_2 + k_4 - \kappa_-)a_2}{\kappa_+ - \kappa_-} \times \frac{k_2(1 - e^{-\kappa_+ t})}{\kappa_+} + \frac{k_3 a_1 - (k_1 + k_2 + k_4 - \kappa_+)a_2}{\kappa_+ - \kappa_-} \times \frac{k_2(1 - e^{-\kappa_- t})}{\kappa_-} \qquad \text{(C. 9)}$$

Based on this model, the composite/ observed rate constants that are obtained from empirical fits of the data have the following dependence on the microscopic rate constants (k_1, k_2, k_3, k_4):

$$\kappa_{\pm} = \frac{(k_1 + k_2 + k_3 + k_4) \pm \sqrt{(k_1 + k_2 + k_3 + k_4)^2 - 4k_3(k_1 + k_2)}}{2} \qquad \text{(C. 10)}$$

The 210 K data is explained by this model by the following arguments: 1) The monoexponential kinetics characterizes only one pathway, namely the formation of $\mathbf{X^{\bullet}}$, thus the fast component of the ($\mathbf{S_1^{\bullet}}$ + $\mathbf{S_2^{\bullet}}$) decay represents the $\mathbf{S_2^{\bullet\prime}}\rightarrow\mathbf{X^{\bullet}}$ reaction, k_1; 2) The amplitude of the fast component (A_f=0.84 ± 0.05, table 3.1) of the decay is considerably larger than the slow component (A_s=0.16 ± 0.05, table 3.1), and $\mathbf{X^{\bullet}}$ amplitude ($[\mathbf{X^{\bullet}}]_{AUC}$=0.43 ± 0.08, Table C.1) is approximately half of the decaying fast component amplitude. Thus, half of the fast decay component amplitude together with the slow component makes up the total **P** amplitude ($[\mathbf{P}]_{AUC}$=0.55 ± 0.08, Table C.1). 3) This indicates that the formation of $\mathbf{X^{\bullet}}$ follows a single process, which is identified as $\mathbf{S_2^{\bullet\prime}}$ to $\mathbf{X^{\bullet}}$, while **P** formation follows two processes: a direct process from $\mathbf{S_2^{\bullet\prime\prime}}$ which has the same microscopic rate constant as $\mathbf{S_2^{\bullet\prime}}$ to $\mathbf{X^{\bullet}}$, equal to the observed fast rate constant; and a decay that follows reactions from $\mathbf{S_1^{\bullet}}$ to $\mathbf{S_2^{\bullet\prime\prime}}$ to **P** which is a much slower process that describes the observed slow rate constant. 4) Additionally, the initial amplitudes of the substrate radical pair in the $\mathbf{S_1^{\bullet}}$ and $\mathbf{S_2^{\bullet}}$ states are identical to the normalized amplitudes of the two components that empirically fit the data (0.16 and 0.84, Table C.6 and 3.1). Under these considerations, the kinetic model results suggest that transition $\mathbf{S_2^{\bullet}}$ to $\mathbf{S_1^{\bullet}}$ was considerably slowed down at 210 K, essentially quenched on the time scale of the reaction and that the initial population of $\mathbf{S}_1^{\bullet}$ which matches the amplitude of the observed slow component contributes towards the final **P** concentration.

For 2 and 4 % v/v DMSO reaction condition, the empirical fits of the kinetics experimental data identify three rate constants from which two are composites of all four microscopic rate constants that describe the kinetics, while one is a direct measurement of a microscopic rate constant. The presence of DMSO increases the dynamics in the PAD and favors a rapid exchange condition compared to the direct reactions from $\mathbf{S}_2^{\bullet}$ states to **P** or $\mathbf{X}^{\bullet}$, $k_3,k_4 \approx k_1,k_2$. Therefore, the rate of growth of $\mathbf{X}^{\bullet}$ describes a unique pathway for the destructive reaction that occurs in the 2-aminopropanol substrate radical. At 4 % v/v DMSO the misfire is enabled entirely by the dominant population trapped upon freeze trapping in the $\mathbf{S}_2^{\bullet\prime}$ state, and it is characterized by the slower rate k_2 as indicated by the simulated results of the kinetic model. This behavior was observed for the reaction kinetics in the absence of DMSO at 210 K, but with the fast rate k_1 at the expense of the k_4 reaction, which is quenched on the time scale of the formation of **P** and $\mathbf{X}^{\bullet}$. The larger concentration of uncoupled species generated at 4 % DMSO for both *T* conditions is supported by the high initial concentration of the total substrate radical in the $\mathbf{S}_2^{\bullet}$ state ($[\mathbf{S}_2^{\bullet}]>[\ \mathbf{X}^{\bullet}]$). (Tables C.1 and C.6) In 2 % v/v DMSO situation the concentration of $\mathbf{X}^{\bullet}$ that is formed reaches roughly 50 % from the initial trapped radical pair at the measured *T* of 230 K and 30 % at 240 K. In these solution conditions, the monophasic uncoupled radicals are initiated from the concentration of Cbl(II)-substrate radical pair which accumulates during turnover in the $\mathbf{S}_2^{\bullet\prime}$ state, a situation that requires the exchange rate to satisfy the condition $k_3=k_1/2$. (Table C.5)

The two proposed hybrid conformations of the substrate radical in the $\mathbf{S}_2^{\bullet}$ state ($\mathbf{S}_2^{\bullet\prime}$ and $\mathbf{S}_2^{\bullet\prime\prime}$) may arise from a steric mismatch of the substrate radical in the active site due to the presence of the methyl group of the 2-aminopropanol. This kinetic model can be validated by structural studies on the EAL- bound radicals that can distinguish possible conformations of the substrate radical at the active site. These can be done by employing X-ray diffraction or NMR techniques.

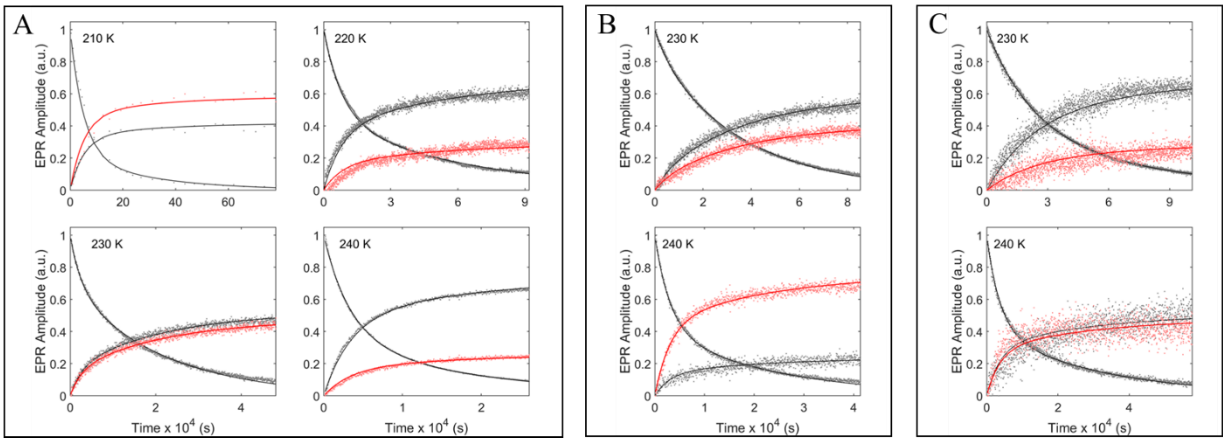

Figure C.3. Time-dependence of the deconvoluted Cbl(II)-2-aminopropanol substrate radical pair decay components in EAL and % DMSO at the corresponding measured *T* values overlaid with simulated components of the kinetic model: A. 0 % v/v DMSO, B. 2 % v/v DMSO and C. 4 % v/v DMSO. The representative single data set shown for each *T* corresponds to the same samples reported in Chapter 3 for the previously proposed kinetic model. The components obtained from measurement (decay of substrate radical and growth of uncoupled Cbl(II)) are indicated in grey dots with the corresponding overlapped black lines for **S**$^{\bullet}$(t) and **X**$^{\bullet}$(t) simulations. The diamagnetic product is shown in light red dots with the simulated **P**(t) in red line.

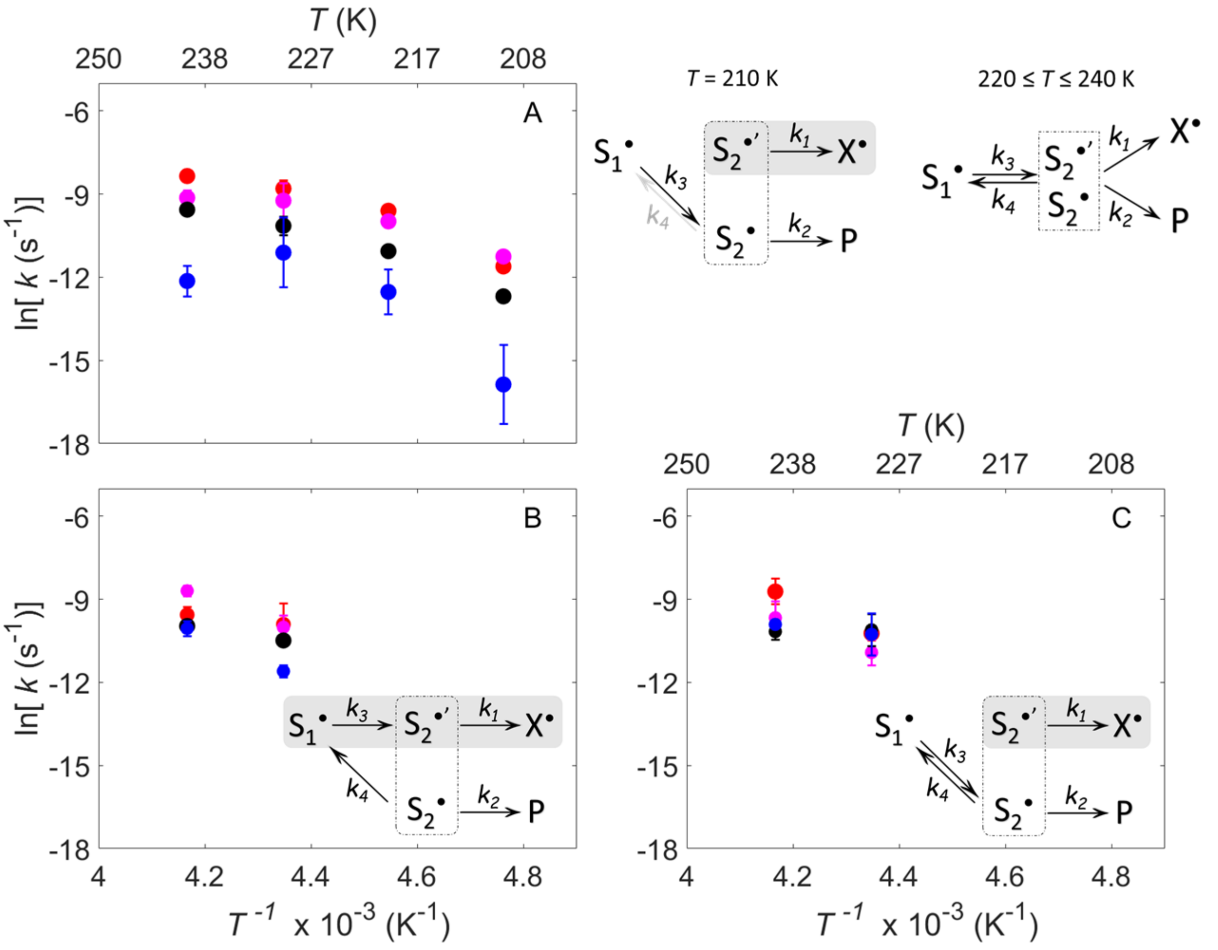

Figure C.4. Arrhenius plots for the microscopic rate constants determined from the kinetic model and proposed mechanism for Cbl(II)-substrate radical decay in EAL in reaction solution with different % v/v DMSO: 0 % (A), 2 % (B) and 4 % (C). The microscopic rate constants (k_1 (red), k_2 (purple), k_3 (black) and k_4 (blue)) are determined for three data sets at each T value. The kinetic mechanism for the decay at the indicated T range is shown next to the Arrhenius plots (A) or as inserts to the Arrhenius plots (B, C). The models indicate reactions that contribute to the kinetics measured by the decay of $\mathbf{S_1^{\bullet}}$ + $\mathbf{S_2^{\bullet}}$ (black arrows) and states that contribute to kinetics measured by the rise of $\mathbf{X^{\bullet}}$ (grey pathway). The grey arrow indicates slow/quenched reaction.

Table C.5. First-order rate constants of the simulate Cbl(II)-substrate radical pair decay kinetics at the respective *T* values by using the microscopic kinetic model reported in previous work[77]. The values represent the mean ± standard deviation, for three separate decay experiments fits at each temperature.

% v/v DMSO	***T* (K)**	**$k_1 \times 10^{-4}$ (s^{-1})**	**$k_2 \times 10^{-4}$ (s^{-1})**	**$k_3 \times 10^{-4}$ (s^{-1})**	**$k_4 \times 10^{-4}$ (s^{-1})**	**R^2**
0	210	0.09 ± 0.01	0.13 ± 0.02	0.03 ± 0.006	0.001 ± 0.002	0.9542 ± 0.0556
	220	0.68 ± 0.13	0.46 ± 0.10	0.16 ± 0.02	0.04 ± 0.03	0.9896 ± 0.0094
	230	1.51 ± 0.45	0.98 ± 0.61	0.39 ± 0.13	0.15 ± 0.19	0.9926 ± 0.0015
	240	2.37 ± 0.33	1.08 ± 0.29	0.70 ± 0.14	0.05 ± 0.03	0.9938 ± 0.0040
2	230	0.50 ± 0.38	0.45 ± 0.19	0.28 ± 0.01	0.09 ± 0.02	0.9832 ± 0.0071
	240	0.71 ± 0.20	1.68 ± 0.33	0.47 ± 0.05	0.43 ± 0.11	0.9597 ± 0.0227
4	230	0.36 ± 0.09	0.18 ± 0.09	0.41 ± 0.24	0.35 ± 0.27	0.9550 ± 0.0015
	240	1.64 ± 0.76	0.63 ± 0.37	0.39 ± 0.12	0.50 ± 0.001	0.6859 ± 0.1448

Table C.6. The initial concentration of the substrate radical present in the **$S_1^\bullet$** and **$S_2^\bullet$** states as calculated by the numerical simulations of the kinetic model. The values represent the mean ± standard deviation, for three separate decay measurements at each temperature.

% v/v DMSO	**T (K)**	**[$S_1^\bullet$]**	**[$S_2^\bullet$]**
0	210	0.16 ± 0.03	0.84 ± 0.03
	220	0.38 ± 0.01	0.62 ± 0.01
	230	0.45 ± 0.10	0.55 ± 0.10
	240	0.33 ± 0.04	0.67 ± 0.04
2	230	0.45 ± 0.25	0.55 ± 0.25
	240	0.19 ± 0.05	0.81 ± 0.05
4	230	0.23 ± 0.15	0.77 ± 0.15
	240	0.24 ± 0.07	0.76 ± 0.07

D. Appendix for Chapter IV

Table D.1. Normalized weights of the substrate radical (**$S^\bullet$**) and uncoupled Cbl(II) (**$X^\bullet$**) components at the end of the decay relative to the initial cryotrapped Cbl(II)-substrate radical pair concentration for each sample. The normalized values are calculated from the AUC values for initial and final EPR absorption spectra.

% v/v DMSO	**Normalized weights**	
	$S^\bullet$	**$X^\bullet$**
0	0.11	0.52
2	0.07	0.39
4	0.15	0.64

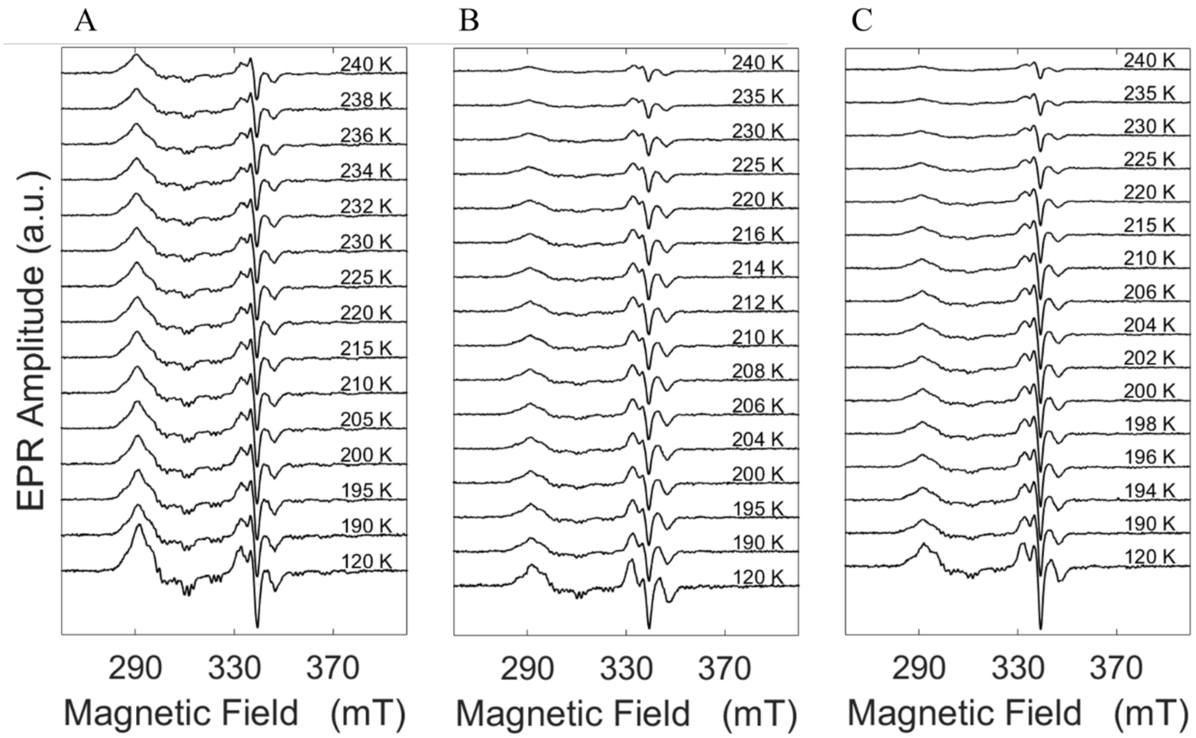

Figure D.1. Temperature dependence of the Cbl(II)-substrate radical and uncoupled Cbl(II) + radical species spectra for the decayed cryotrapped Cbl(II)-2-aminopropanol substrate radical pair in EAL solution in the presence of different added % v/v DMSO: (A) 0 %; (B) 2 %; (C) 4 %.

Figure D. 2. Fitting results for the progressive power saturation measurements at 200 K and 235 K for uncoupled Cbl(II) and substrate radical, **S**$^\bullet$, in EAL and different % DMSO.

Radical species		**S$^\bullet$**		**Cbl(II)**	
% v/v DMSO	***T* (K)**	***$P_{1/2}$***	***R^2***	***$P_{1/2}$***	***R^2***
0	200	107	0.9694	21.6	0.8458
	235	221	0.9004	45.6	0.8996
2	200	116	0.9802	52.5	0.8293
	235	279	0.4918	336	0.6636
4	200	109	0.9378	26.6	0.9795
	235	336	0.2469	138	0.9662

E. Appendix for Chapter V

The homology model using a protein molecular modeling server Geno3D (http://geno3d-pbil.ibcp.fr) was done for both EutS and EutL proteins from *S. typhimurium*. The model generated 10 possible structures with overall RMSD values from the template structure. The best model was chosen, and a cartoon structure can be seen in Figure E.1 overlaid with the respective templates. The templates used are the *E. coli* PDB structures 3i96 for EutS, 3i82 for EutL closed conformation (EutLc) and 3i87 for EutL open conformation (EutLo). The alignment function used in PyMOL was performed for sequence alignment with structural superposition and for C_α atoms alignment. (Table E.1.)

Table E.1. Results for alignment methods performed in PyMOL for modelled *S. typhimurium* EutS and EutL structures on template *E. coli* PDB structures 3i96 (EutSc), 3i82 and 3i87 (EutLo).

Protein	**sequence alignment**		**C_α atoms alignment**	
	RMSD	% atoms aligned	RMSD	% atoms aligned
EutS	0.78	89.5	0.67	96.4
EutLc	0.66	84.9	0.55	89.7
EutLo	0.69	89.1	0.57	92.8

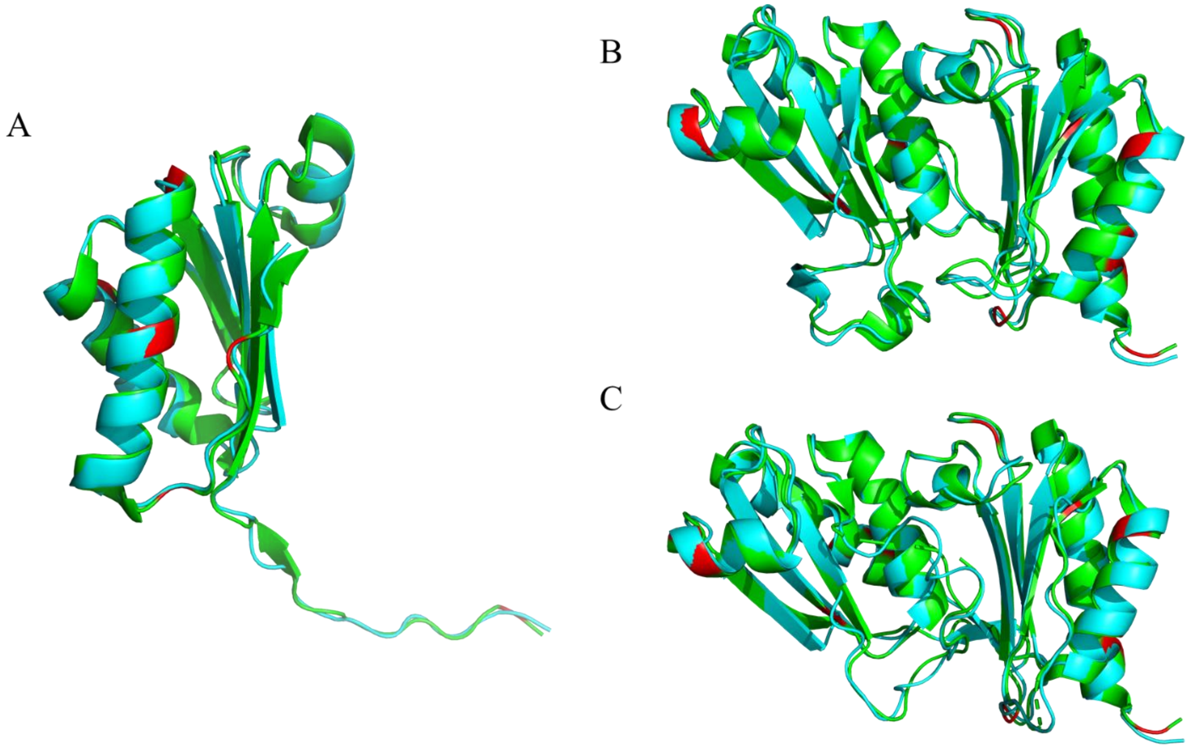

Figure E.1. PyMOL cartoon representation of EutS (A) and, EutL closed (B) and open (C) conformations from *E. coli* template structures (green; 3i96, 3i82 and 3i87) overlaid with the *S. typhimurium* modelled structures (blue). The overlay was achieved by structure alignment in PyMOL.

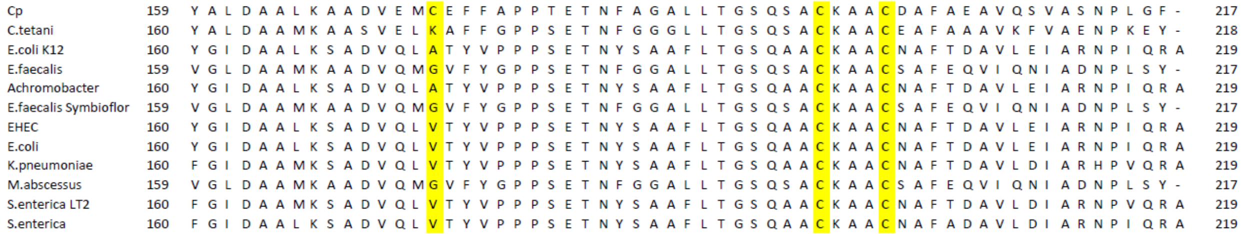

Cp	159	Y A L D A A L K A A D V E M C E F F A P P T E T N F A G A L L T G S Q S A C K A A C D A F A E A V Q S V A S N P L G F -	217
C.tetani	160	Y A L D A A M K A A S V E L K A F F G P P S E T N F G G G L L T G S Q S A C K A A C E A F A A A V K F V A E N P K E Y -	218
E.coli K12	160	Y G I D A A L K S A D V Q L A T Y V P P P S E T N Y S A A F L T G S Q A A C K A A C N A F T D A V L E I A R N P I Q R A	219
E.faecalis	159	V G L D A A M K A A D V Q M G V F Y G P P S E T N F G G A L L T G S Q S A C K A A C S A F E Q V I Q N I A D N P L S Y -	217
Achromobacter	160	Y G I D A A L K S A D V Q L A T Y V P P P S E T N Y S A A F L T G S Q A A C K A A C N A F T D A V L E I A R N P I Q R A	219
E.faecalis Symbioflor	159	V G L D A A M K A A D V Q M G V F Y G P P S E T N F G G A L L T G S Q S A C K A A C S A F E Q V I Q N I A D N P L S Y -	217
EHEC	160	Y G I D A A L K S A D V Q L V T Y V P P P S E T N Y S A A F L T G S Q A A C K A A C N A F T D A V L E I A R N P I Q R A	219
E.coli	160	Y G I D A A L K S A D V Q L V T Y V P P P S E T N Y S A A F L T G S Q A A C K A A C N A F T D A V L E I A R N P I Q R A	219
K.pneumoniae	160	F G I D A A M K S A D V Q L V T Y V P P P S E T N Y S A A F L T G S Q A A C K A A C N A F T D A V L D I A R H P V Q R A	219
M.abscessus	159	V G L D A A M K A A D V Q M G V F Y G P P S E T N F G G A L L T G S Q S A C K A A C S A F E Q V I Q N I A D N P L S Y -	217
S.enterica LT2	160	F G I D A A M K S A D V Q L V T Y V P P P S E T N Y S A A F L T G S Q A A C K A A C N A F T D A V L D I A R N P V Q R A	219
S.enterica	160	F G I D A A L K S A D V Q L V T Y V P P P S E T N Y S A A F L T G S Q A A C K A A C N A F A D A V L D I A R N P I Q R A	219

Figure E.2. Sequence alignment for pathogens reported to cause food poisoning. C127 is absent in all strains but *C. perfringens* ortholog.

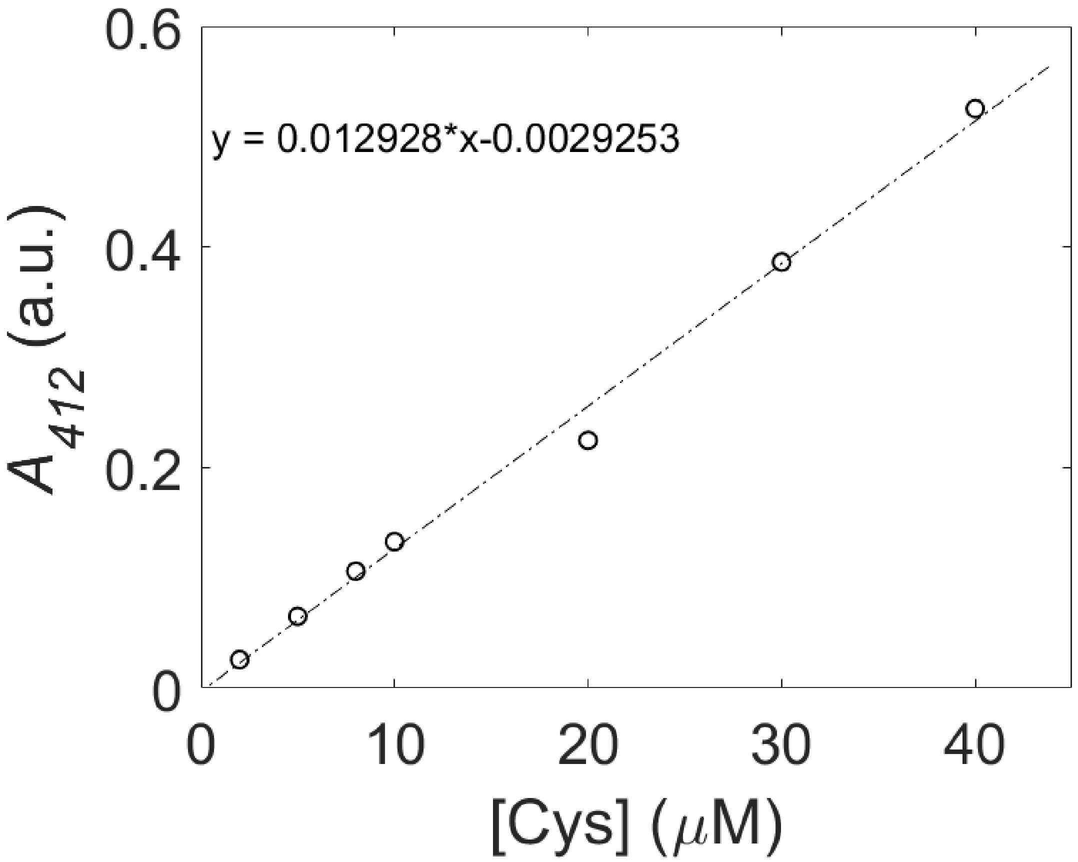

Figure E.3. Calibration curve for Ellman's test performed by using DLCys. The resulted absorption values at 412 nm are used to determine the concentration of Cys residues from this curve.

Table E.2. Possible H-bonds indicated by PyMol. The distances suggest moderate H bonding characteristic for proteins. Amino acids that do not present major bonding formation within the loops structure could be identified. In addition, based on these distances and H-bonding, the possible amino acids involved in each state stabilization were determined. All the residues found are conserved between EutL orthologs from *E. coli* and *S. typhimurium*.

H bonds	Closed		Dist. A	Open		Dist. A
Stabil form	Glu182	Arg67	3.1	Tyr49	Ala74	2.7
		Ser68	2.9	Ala123	Tyr185	3.2
		Ala71	2.8	Gly76	Asp45	3.2
	Thr80	Ser41	2.7		Asp46	3
		Thr12	2.9			
	Glu83	Asp45	2.9	Thr80	Asp43	3.1
		Ala42	2.9	Val84	Asp42	3.1
α3	Gly76	Ala73	2.9			
	His75	Gly72	3.1			
α3-β3	Leu69	Gly72	3.2	Thr80	Gly82	2.7
	Glu83	Ala73	2.9			
	Ser78	Ala81	3.4;3	His75	Ala71	3
		Thr80	3;3.5			
β’4-β’3	Val177	Ala187	3	Asn184	Thr183	3
		Ser186	2.9		Tyr185	3
	Ser181	Tyr185	3;3.1	Ala123	Tyr185	3.2
		Thr183	3;3.5			
		Asn184	3			
α’1	Thr139	Leu136		Thr139	Leu136	
	Ser138	Tyr135		Ser138	Tyr135	
		Ser134			Ser134	
	Ser137	Ser134	3	Ser137	X Ser134	3.6
		Gly133			Gly133	

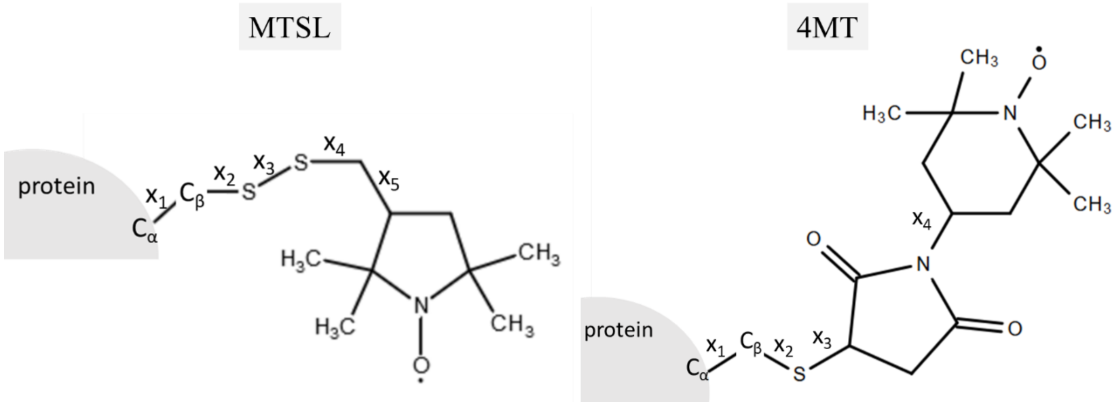
MTSL

4MT

Figure E.4. The nitroxide labels MTSL and 4MT. MTSL is the available label given by the MMM library for simulating the rotamer states at the desired residue in the protein. The nitroxide used for the experiments is 4MT. MTSL bind to the protein through a link longer than 4MT induced by the disulfide bond.

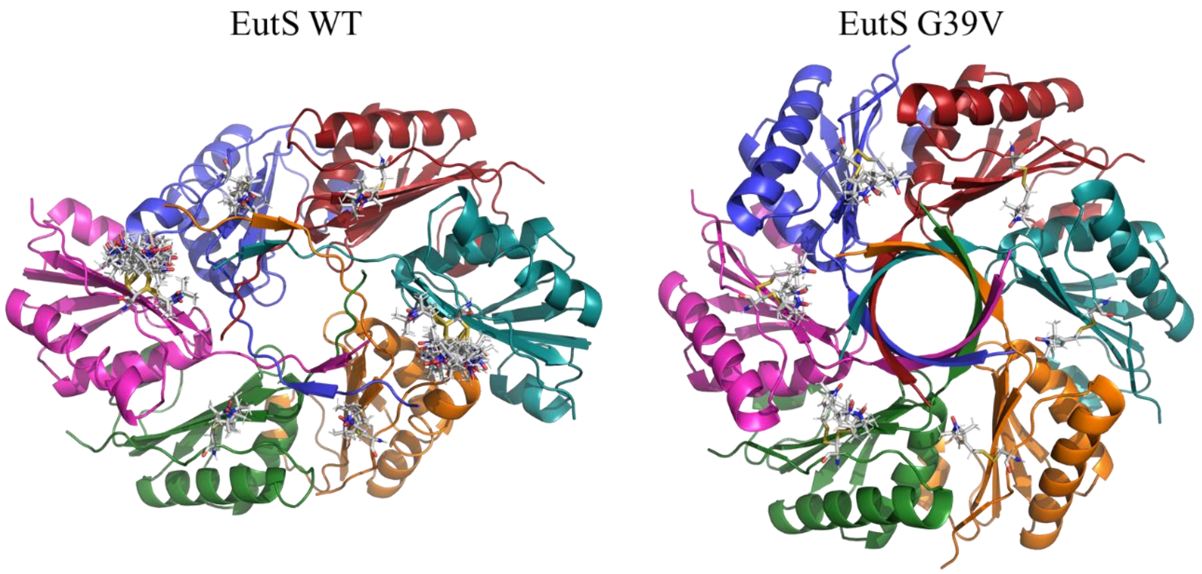
EutS WT

EutS G39V

Figure E.5. Rotamer simulations of the MTSL at C106 within the EutS protein. The probable rotameric states given by MMM software are shown in grey sticks for both bend (left) and flat (right, G39V) conformations.

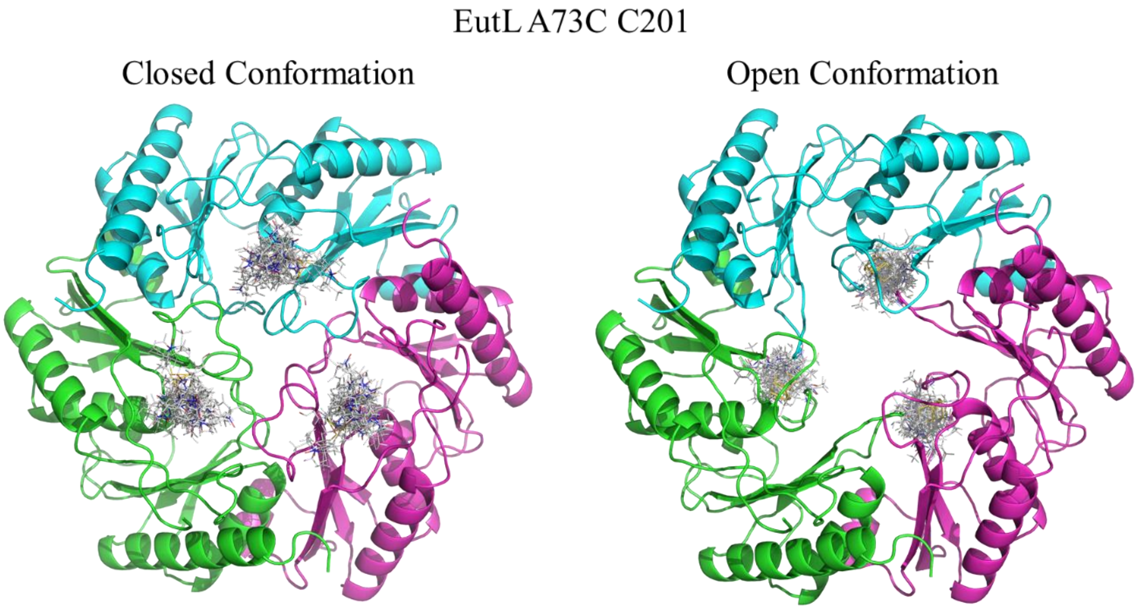

Figure E.6. Rotamer simulations of the MTSL at A73C within the EutL protein. The probable rotameric states given by MMM software are shown in grey sticks for both closed (left) and open (right) conformations. The images show opposite sides for the EutL: open structure is visualized from the back of the closed structure.

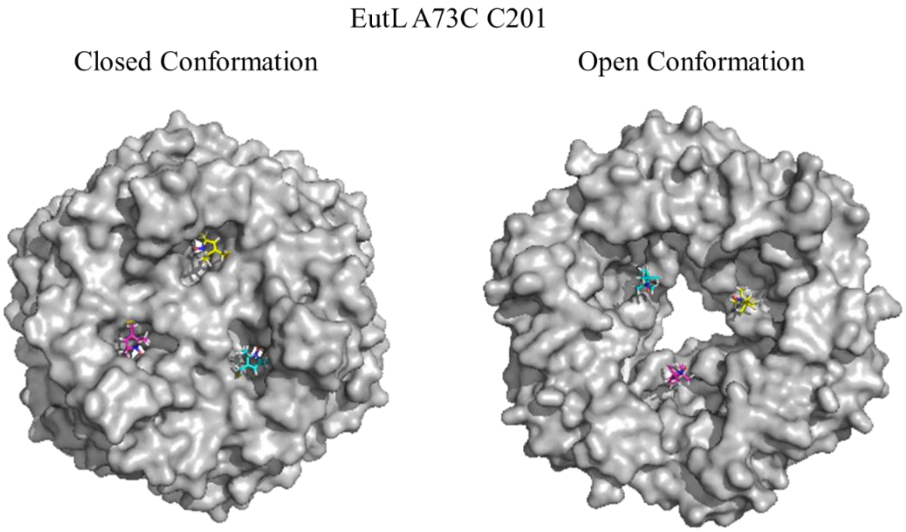

Figure E.7. Spin label configurations for EutL A73C. Surface map of the protein shows accessibility region for the MTSL modelled at the residue position. The three molecules shown as sticks are the MTSL most probable rotamer state covalently linked to the protein.

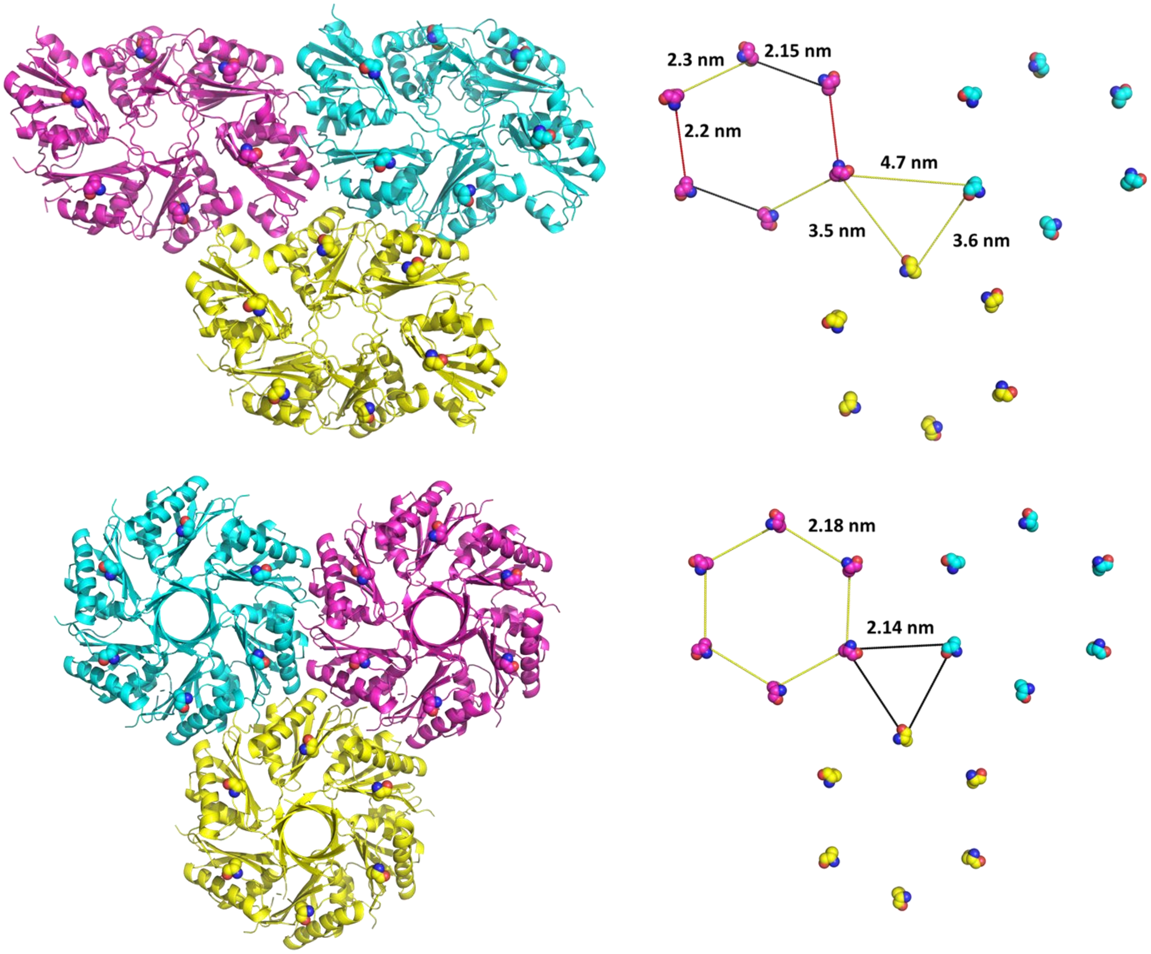

Figure E.8. Structural models of the tile formation by the two conformations of EutS BMC protein generated by using PYMOL (PDB files 3i96 and 3ia0). The right diagram shows the positions of the cysteines in the modeled tile packing, and the distances between them.

```
Closed   1    MPALDLIRPS VTAMRVIASV NADFARELKL PPHIRSLGLI SADSDDVTYI   50
Open     1    MPALDLIRPS VTAMRVIASV NADFARELKL PPHIRSLGLI SADSDDVTYI   50

Closed  51    AADEATKQAM VEVVYGRSLY AGAAHGPSPT AGEVLIMLGG PNPAEVRAGL  100
Open    51    AADEATKQAM VEVV------ AGAAHGPSPT AGEVLIMLGG PNPAEVRAGL  100

Closed 101    DAMIAHIENG AAFQWANDAQ DTAFLAHVVS RTGSYLSSTA GITLGDPMAY  150
Open   101    DAMIAHIENG AAFQWANDAQ DTAFLAHVVS RTGSYLSSTA GITLGDPMAY  150

Closed 151    LVAPPLEATY GIDAALKSAD VQLATYVPPP SETNYSAAFL TGSQAACKAA  200
Open   151    LVAPPLEATY GIDAALKSAD VQLATYVPPP -ETNYSAAFL TGSQAACKAA  200

Closed 201    CNAFTDAVLE IARNPIQRAL EHHHHHH     227
Open   201    CNAFTDAVLE IARNPIQRAL EHHHHHH     227
```

Figure E.9. Alignment sequence for EutL from *E. coli* in closed and open conformations. The highlighted regions are missing in the structure of the open conformation.

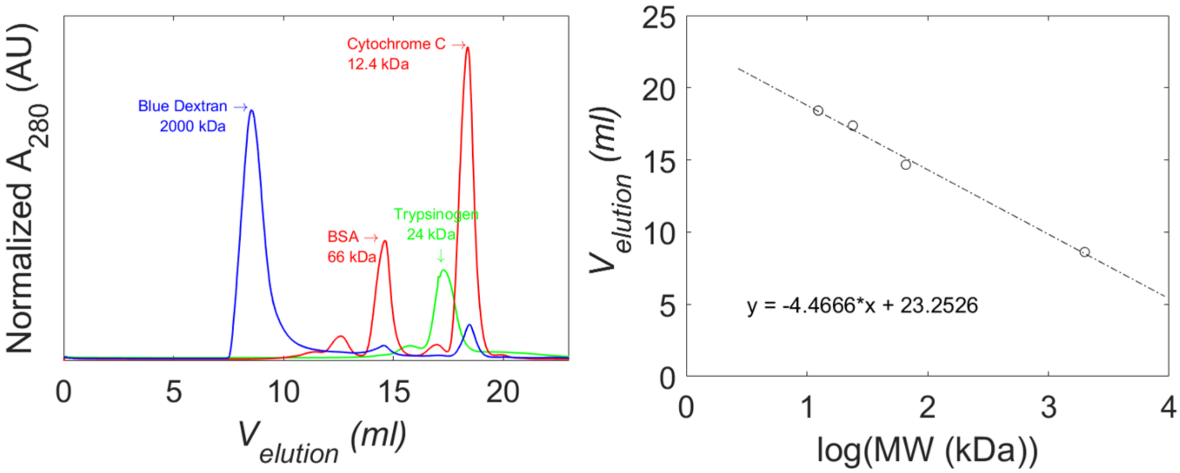

Figure E.10. Gel filtration retention profiles and calibration curve for Superdex 200. Left image is the retention profiles for known protein masses blue dextran, BSA, trypsinogen and cytochrome C. The absorbance was normalized to the highest peak. BSA and trypsinogen were ran together on the column. Each characteristic peak is indicated. Right image shows the calibration curve for the Superdex 200 in 20 mM Tris, 100 mM NaCl pH8 buffer as the retention volume as a function of the log MW. All EutS and EutL protein masses were determined using this information.

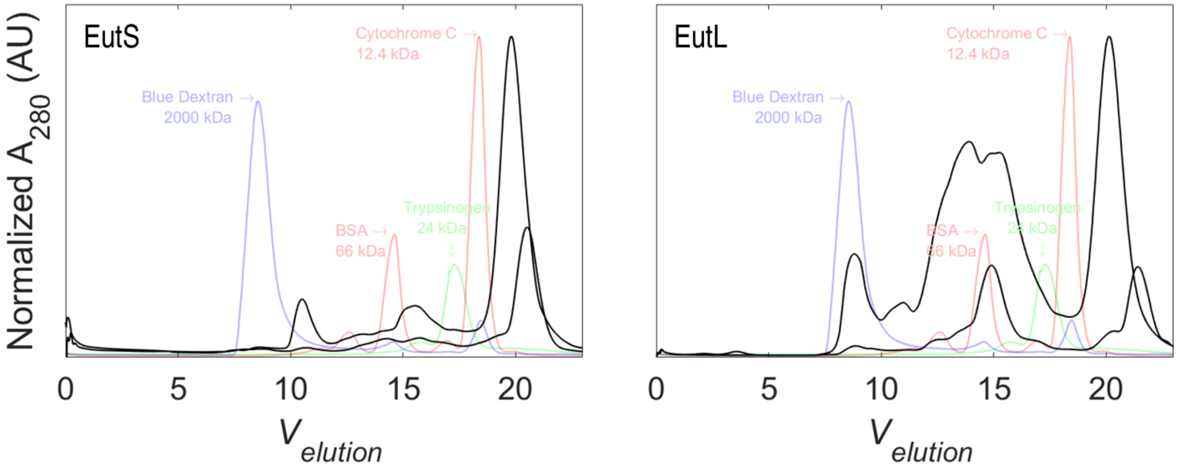

Figure E.11. Gel filtration on Superdex 200 of purified proteins. The retention profiles of the oligomeric structures of EutS (left, black lines) and EutL (right, black lines) purified protein are shown overlaid with the known molecular mass proteins. The two black lines show two different purified samples.